Use of Ultrasonic Pulses to Detect State of Charge and State of Health in Lithium-Ion Batteries

Royce John Copley

A thesis submitted in partial fulfilment of the requirements for the degree of Doctor of Philosophy

The University of Sheffield
Faculty of Engineering
Department of Mechanical Engineering

January 2022

Abstract

The rapid growth in the adoption of lithium-ion batteries since their introduction in the 1990's is expected to continue in the coming years. Electric vehicles in particular will account for a large market share, being considered clean transportation technology compared to the internal combustion engine. Lithium-ion batteries change their internal state during cycles of charge and discharge. Estimation of the state of charge is commonly performed by battery management systems that rely on charge counting and cell voltage measurements. Determining the physical state of the battery components is challenging.

Recently, the response of an ultrasonic pulse through a battery has been successfully correlated with both change in state of charge and state of health, the approach is now well established. This study assesses the qualities contained within an ultrasound signal response by investigating the behaviour of ultrasonic waves as they pass through the components in a layered battery structure, as those components change with battery charge. This is possible based on acoustic sensitivity to material property changes such as electrode density during charge cycling. Captured reflections from pulsed signals will accumulate in the signal response, with observed differences providing the potential for real-time, non-invasive, non-destructive measurements of internal changes in the battery cell.

A model has been developed to understand the nature of the ultrasound response and the features that provide a particular characteristic. Modelling was based on the one-dimensional wave equation, scripted in MATLAB. Layered properties simulating a battery cell are required to run the model, the outputs of which include simulated wave responses, wave development plots and animations.

Experiments were conducted to establish methodologies in detecting a relationship between battery state of charge and ultrasound response. Data analysis and visualisation methods were developed during this study to determine the optimal methods of gaining battery charge measurements. The accuracy of charge monitoring is affected by temperature, either from the cell or ambient conditions. Evaluation of temperature effect is possible using analysis contained in this work, with a method of calibrating signal for temperature suggested.

It was concluded from experimental testing combined with modelling that small changes in battery parameters could cause significant changes to an expected signal response. The variety in cell construction and manufacturing discrepancies presents a serious problem for the application of ultrasound monitoring in practice. A smart peak selection method was developed to ensure that regardless of the nature of the ultrasound response, state of charge measurements are optimised by

ensuring the regions of signal with best battery charge correlation are identified. This can greatly help with the automation of the process in a sensor-based battery management system.

Finally, ultrasonic monitoring was explored as a method of early warning of the onset of thermal runaway during thermal abuse testing. The signal responses show deviations from expected signals at temperatures consistent with expected cell reactions to temperature increases, such as the onset of self-heating and electrode delamination. Instrumentation calibration and limitation tests were conducted to provide confidence that changes in ultrasound responses are battery and not sensor related.

Contents

iv

List of Figures

x

xiii

List of Tables

Supplementary Materials

Figure S.1 Standard separator Top panel - 2MHz pulses travelling through layers of a simulated cell. Red wave represents wave through discharged cell, green through charged cell. Middle panel - pulse/echo, A scan generated in real time. Bottom panel - pitch/-catch, through pulse A-scan generated in real time.

Figure S.2 Low speed separator Same plots as in Figure S.1, arbitrary separator speed reduction causes collapse of clear signal response.

Figure S.3 5MHz pulse Top panel - 5MHz pulses travelling through layers of a simulated cell. Red wave represents wave through discharged cell, green through charged cell. Middle panel - pulse/echo, A scan generated in real time. Bottom panel - Moderate signal differences occur early between charge/discharged signals, likely to contain poor charge measurement correlations.

Figure S.4 0.5MHz pulse Same plots as S.3 with 0.5MHz pulse. Bottom panel shows little signal difference between charged/discharged signals, likely to contain no charge measurement correlations.

Figure S.5 2MHz pulse Same plots as S.3 with 2MHz pulse. Bottom panel shows significant differences between charged/discharged signals around 6-8µs, likely to contain strong charge measurement correlations.

Figure S.6 1.5 standing wave in layer 2.25MHz pulses transmitted through a 2mm body having a wavespeed of 3000m/s creating a resonant 3/2 standing wave.

Figure S.7 XWT charge cycling Left panel - the cross wavelet transform (XWT) changing during cycling, changing phase arrows are visible across the 2MHz frequency band. Middle panel - contains the signal important factor, when normalised it is shown to provide a stable region from which to take charge measurements. Right hand panel - the charged A-scans move during charge cycling, using the discharged as a static reference. A state of charge bar is added to the left panel that applies to all three plots.

Abbreviations

λ Wavelength (distance)

Ah   Amp hour

ARC   Accelerated rate calorimetry

AU   Arbitrary units

BMS   Battery management systems

C   C-rate

CCCV   Constant current, constant voltage

COI   Cone of influence

CWT   Continuous wavelet transform

FFT   Fast Fourier transform

Hz   Hertz

Li   lithium

Li^+ Lithium-ion

mA   milliampere

SAM   scanning Acoustic Microscopy

SEI   Solid electrolyte interphase

SoC   State of charge

SoH   State of health

STFT   Short-time Fourier transform

ToF   Time of flight

TR   Thermal runaway

UHFUS   Ultra high frequency ultrasound

V   Voltage

XWT   Cross wavelet transform

Acknowledgments

I would like to give deepest thanks and gratitude to my main supervisor Rob Dwyer-Joyce. Thank you for showing faith in me right from the very start, for providing me with the opportunity to do a PhD and also for the support, guidance and encouragement throughout. I would also like to give thanks to my additional supervisors Denis Cumming and Yajue Wu who have given me much advice and guidance that was invaluable during the course of this project.

A sincere thank you to Ricardo for their show of faith in supporting me and and funding this PhD, in particular many thanks go to Jonathan Wheals for his enthusiasm and support for which I am very grateful. Also thanks go to Michael Wheeldon and Ben Reid who I have worked with during the course of this project.

Many thanks to all those people who have helped me, Jake Entwistle for his help in setting up my initial tests and training me on the relevant equipment. Peter Bugryniec for his patience, help and advice working on the thermal abuse tests. Thanks also to Gary Nicholas for his support in the lab and assistance whenever I have needed it and to Xiangwei Li for being someone I could speak with whenever I have needed advice or help. Thanks to Andy Hunter, for the kindness and patience to help, in the early days in sorting my data acquisition software and later on building a complete ultrasound test kit. Everyone I have crossed paths with during this work has been friendly, helpful and knowledgeable, it has been an amazing experience.

I would like to thank my family for their continued support over the years of this exciting academic journey, my wife Lindsey for the daily support and encouragement she provides, to my daughter Connie and my son Wilfrid who have showed so much enthusiasm and interest in my work. Finally, thanks to my Mum and Dad who believed in me all my life. I hope I have made you all proud.

1 Introduction

In this chapter, lithium-ion batteries are introduced and the increase in adoption and continuing expected rapid growth is evidenced. Challenges around effective and safe usage of lithium-ion cells are presented, with battery management systems (BMS) being utilised to monitor cell performance developed to control these issues. The scope of this thesis is introduced, focusing on the ultrasonic monitoring of battery cells.

1.1 The Continuing Rise of Lithium-Ion Batteries

Since their introduction in the 1990's, lithium-ion batteries have become increasingly popular in mobile power applications, from handheld devices such as smart phones and tablets to electric vehicles. The success of the lithium-ion battery is due to its high energy density and operating voltage, the best energy-to-weight ratio, no memory effect and undergo only small amounts of discharge when not in use when compared to alternative battery technologies[1–3]. There are limitations with this technology; stress induced material damage, capacity fade and the potential for thermal runaway. Even with optimal usage a battery can support only a finite number of charge/discharge cycles, improper use can lead to deterioration in battery performance and a shortening of lifespan[4].
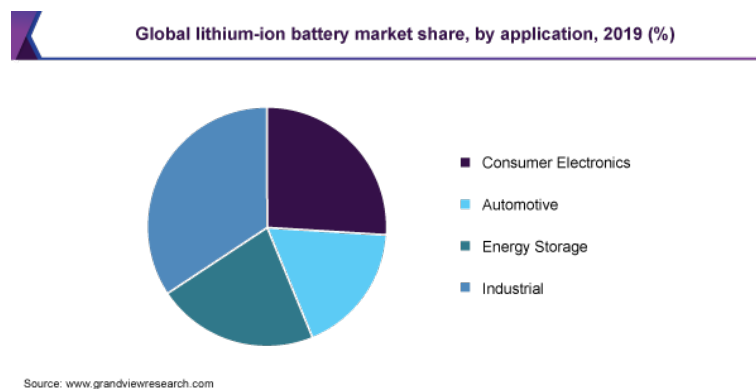
Figure 1.1: Lithium-ion battery market share[5].

Currently, consumer electronics account for approximately a quarter of the global market share of lithium-ion batteries whilst energy storage and industrial applications account for over 50%. As of 2019, it is estimated that transportation already accounted for almost a quarter of global lithium-ion batteries (Figure 1.1)[5]. The significant market share is despite electric vehicles currently being a niche market. The 1.18 million

electric vehicles on the road in the U.S. account for a small percentage in 2019, just 1.8% of cars sold were electric vehicles[6].

There has been a growing rise in demand for electric vehicles in recent times and this trend is expected to continue over the next 10 years. Figure 1.2 shows that by 2030 it is predicted there will be an annual demand of over 1500GWh for electric vehicles, a ten fold increase on current levels of demand[7].
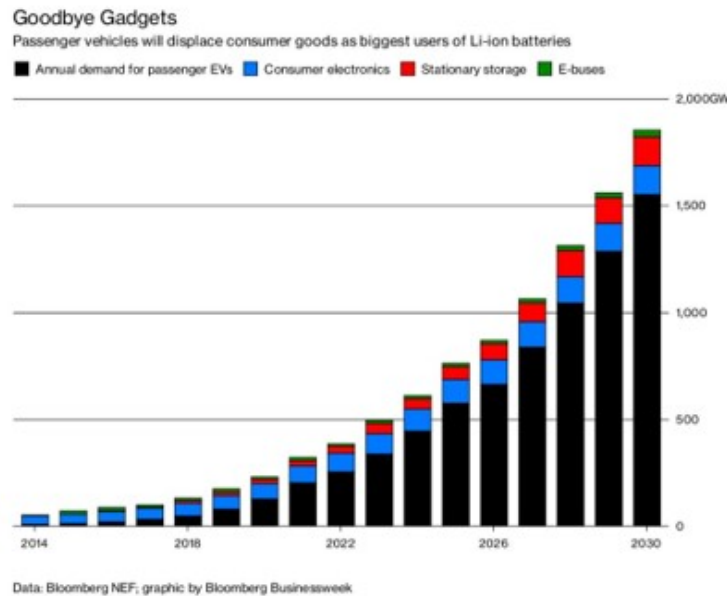
Figure 1.2: Predicted increase in demand for lithium-ion batteries over the next 10 years[7].

Electric vehicles are widely accepted as clean transportation technology compared with the internal combustion engine, reducing reliance on fossil fuels. This exploitation of sustainable energy will play a significant role in slowing down the rate of global warming[8].

Electric vehicles are energy efficient, converting over 77% of the electrical energy from the grid to power at the wheels. This is compared to conventional gasoline vehicles which convert about 12%–30% of the energy stored in gasoline to power at the wheels. Whilst the power plant producing the electricity to power electric vehicle may emit pollutants, electricity from clean and renewable sources such as nuclear, wind and solar powered plants cause no air pollutants. Adoption of electric vehicles would reduce greenhouse gases emissions using renewable energy sources. Additionally, electric vehicles emit no tailpipe pollutants, making them an environmentally friendly solution to transportation demands[9].

As the demand for lithium-ion batteries grow, so does the requirement to facilitate safe and efficient battery operation. Battery management systems are used to control battery usage, the development of which is a popular topic of research. There are significant challenges monitoring a battery cell, being a closed electrochemical system and challenging to estimate. Developing accurate and reliable technologies in battery management systems remains a demanding task. This is noted in current research literature[8,10] and will also be recognisable to most users of electronics powered by lithium-ion batteries first hand, through daily usage.
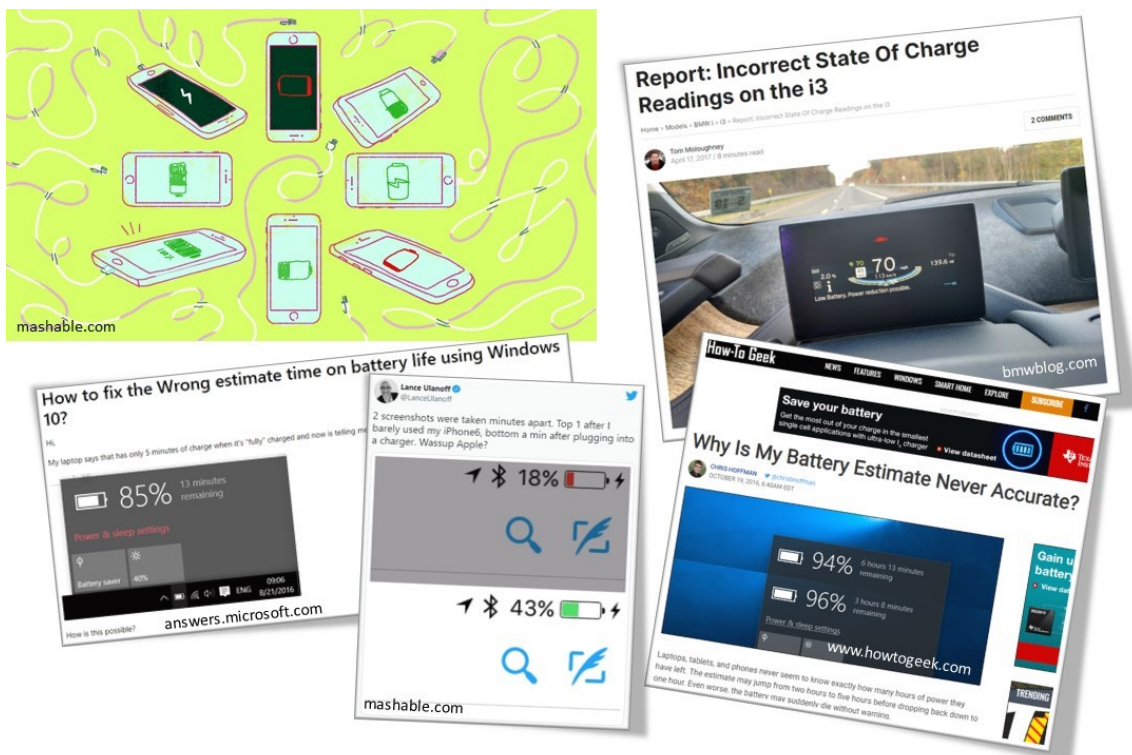
Figure 1.3: Problems experienced during daily usage of lithium-ion batteries[11–14].

Figure 1.3 shows a sample of readily obtainable comments of frustration and inconvenience experience by consumers using lithium-ion batteries. This is usually not born of frustration with the battery itself, but with inaccurate reporting, of available charge for example. Whilst this frustration and inconvenience is unappealing when using smaller devices such as laptops or smart phones, accurate battery reporting is absolutely critical in electric vehicles and aerospace[15] applications for example.

A recently explored method of battery monitoring is the application of ultrasonic inspection. The development and current status of this technique is discussed in some detail in Section 3.2. To introduce one of the main ideas behind the use of ultrasound

in this battery monitoring application. A commercial 2Ah cell is is shown in Figure 1.4 next to a pile of 15 staples. The staples represent the approximate equivalent mass of material that moves between layers in the cell during charge/discharge cycling. It is this movement of material, lithium-ions in this case, that causes shifts in the cross sectional distribution of material density that ultrasonic wave responses detect.
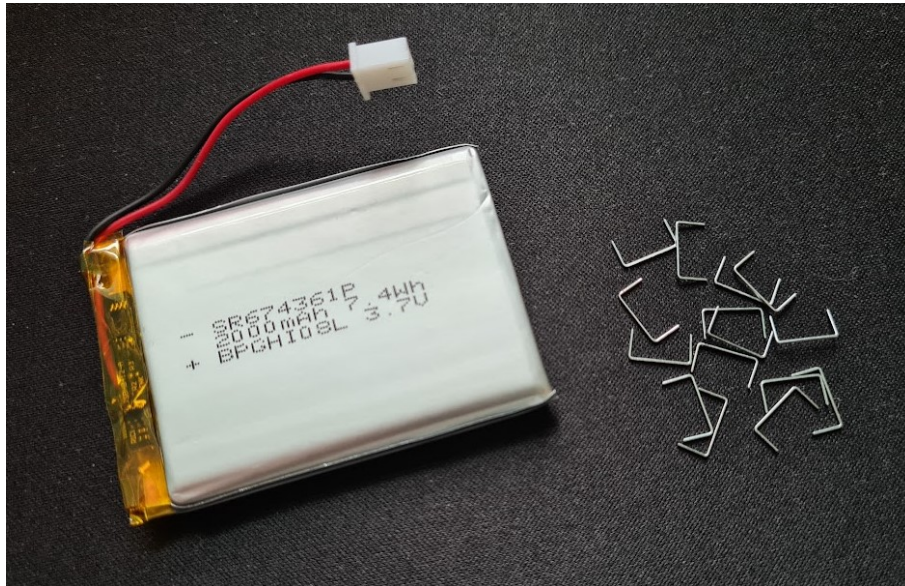
Figure 1.4: 2Ah pouch cell with approximately 0.5g of staples.

Capturing changes in wave response provide the potential for real-time, non-invasive, non-destructive measurements of internal changes in the battery cell. The scope of this thesis is focused on the development of ultrasonic inspection of lithium-ion battery cells.

1.2   About the Thesis

The work contained in this thesis is sponsored by Ricardo Innovations UK. The key aims were to establish the ultrasonic method with respect to battery monitoring, designing a test system where the ultrasonic responses alter with respect to internal changes in a lithium-ion battery cell, either during normal operation or fault conditions. Once the method is established, robust data processing methods are developed to assess the quality and accuracy of the signal responses. Modelling is developed to simulate waves passing through a multi-layered body such as a battery cell.

1.2.1   Objectives

The aim of this project was to develop a methodology for recording and interpreting ultrasonic measurements of a lithium-ion cell during various states. This was to gain an understanding into the potential for this battery monitoring technique to make further developments that may be utilised in future battery management systems. The objective for this project can be summarised into four main categories as follows:

1. **Establish methodology**. Acquire or locate test equipment to control battery aspects (charge cycling, battery abuse methods for example) and ultrasound signal generation/data capture hardware. Suitable sensor equipment, commercial probes and sensors cut from piezoceramic plates/discs. Correct application/development of relevant software solutions to all equipment.

2. **Standard testing (state of charge)**. Design charge cycling test program and monitor using ultrasound responses for measurable changes. Optimise signal measurement methodology to account for signal variability. Assess the effect during charge cycling by establishing a measuring method to compare temperature/charge effect on the signal.

3. **Non-standard testing (thermal abuse)**. Adapt and apply developed ultrasonic inspection methodology to lithium-ion cells undergoing thermal abuse to monitor battery degradation. Assessment of hardware, specifically sensor limitations and measurement reliability at extreme temperatures.

4. **Multi-layered (battery cell) body ultrasound modelling**. Developed new 1D layered modelling system to monitor wave transmission/reflection effects in real time. Use model to better understand wave response in pulse/echo, pitch/catch through pulse configurations. Understand the behavior of waves in such applications.

1.2.2   Thesis Layout

The layout of the thesis is as follows. Background to the main concepts, ultrasound and batteries, are covered in **chapter 2**. The ultrasound discussion pays particular attention to concepts and phrases occurring throughout this work. Sensor options are briefly introduced along with bonding methods. Finally, basic battery operation is described

covering the transportation of material during charge cycling, the process that enables ultrasonic monitoring.

Chapter 3 presents a literature review in two parts. Firstly, current measuring methods utilised in battery management systems and the challenges in ensuring safe and efficient usage of lithium-ion batteries. Secondly, a comprehensive review of ultrasonic monitoring of batteries, covering the history, scope and opportunities to develop this growing area of research.

The development of a 1D wave model is covered in **chapter 4**, detailing the construction of the model and various outputs. Insights gained from the modelling are presented in this chapter. Equipment used during experimental testing, test methodologies and data processing techniques are presented in **chapter 5**. Ultrasound and battery charge cycling hardware and software is described, with an introduction to the MATLAB script designed to process results included.

Experimental results from standard condition, charge cycling tests are presented in **chapter 6**. Data synchronisation and visualisation methods are discussed, with correlations for various ultrasound and battery parameters compared. Cell surface temperature is recorded to asses the impact of temperature fluctuations, both from internal, cell driven changes during charge cycling and external ambient effects. A smart peak selection method is suggested for optimised charge readings regardless of signal quality.

In **chapter 7**, non-standard, thermal abuse tests are conducted. Equipment, instrumentation, experimental methodologies and data analysis techniques adapted for these specialised tests are described. Challenges around ultrasonic monitoring of an object undergoing thermal changes are addressed, as acoustic signal responses are sensitive to changes in temperature. References are obtained from metal blocks during heating to provide hardware performance data. This includes temperature limitations of the method and signal behaviour benchmarks from which deviations are assumed to be battery cell related.

Finally, **chapter 8** draws overall conclusions on this work and suggestions for further work are outlined.

2   Background

This chapter describes the two most important aspects of this work. Firstly, ultrasound waves and how they travel through a medium, with specific focus on moving through layer boundaries. Key concepts such as frequency and how this relates to wavelength are discussed. Wavelengths being a critical aspect of this work, the concept of full and partial reflections through various layer thicknesses are defined. Instrumentation arrangement options are presented with decisions available regarding desired wave paths for signal transmission, with the benefits of each method explained. Sensor options used during this work are outlined including bonding/attachment methods. Secondly, there is an introduction of how batteries work, with special attention given to the processes that take place during charge cycling. Battery construction types are introduced along with details of charge cycling methods, key information to understanding results and discussions in later chapters.

2.1   Ultrasound and Waves

Ultrasound defines sound waves that are above the normal range of human hearing, generally referred to as frequencies greater than 20kHz[16]. Ultrasound waves are non-invasive and there is no requirement to introduce instrumentation into any body under exploration and importantly, ultrasound is non-destructive, so that the propagating sound waves creating only minor and non-permanent changes to the body at particle level. Typically, waves are pulsed using either/or a combination of, longitudinal waves (where the material vibration occurs parallel to the direction of travel) and shear waves (where the vibration occurs perpendicular to the direction of wave travel)[17].

2.1.1   Frequency and Wavelength

The frequency of a wave is the number of oscillations per second, measured in Hertz (Hz). Wavelength is the distance between two points that are in the same state of motion, for example, the peaks of adjacent waves, measured in metres (m). The plots in Figure 2.1a illustrate this relationship. The blue plot represents 3 cycles (identified at the peaks) of 2MHz sine wave. The wavelength in the time domain (T), also known as period, is measured to be 0.5μs. The frequency relates the wavelength using equation 2.1 such that the frequency of a wave is the reciprocal of its period and vice versa. The

orange plot shows 6 cycles (identified at the peaks) of 4MHz sine waves, this time with a period of 0.25μs.

The 2MHz waves have larger peaks, twice the size of the 4MHz waves. This is signal amplitude and normally measured in Volts. In practice the higher voltage applied to a signal, the higher the signal strength (amplitude). Higher voltage signals are used when standard pulsing methods are unable to penetrate a body with enough power to reach the signal capturing sensor. High voltage signals will also help improve signal to noise ratio, improving accuracy. Note the y-axis is measuring the amplitude in arbitrary units (AU). This measure of amplitude is applied throughout this work, as measurements are taken from change in signal rather than the values themselves.
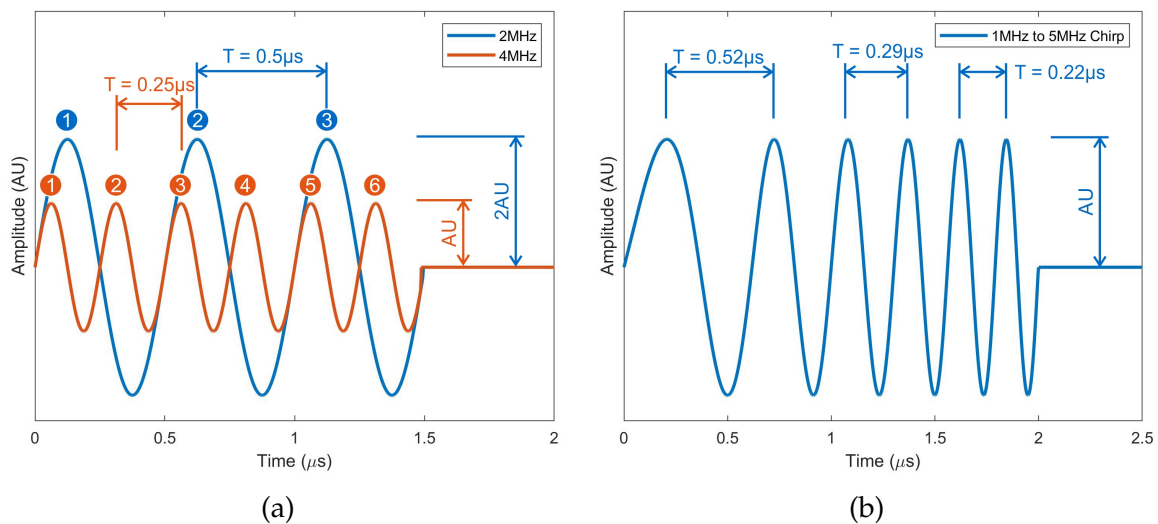
Figure 2.1: a) relationship between frequency and wavelength in pulses using cycles of sine waves and b) a chirp signal that contains a range of frequencies.

$$f = \frac{1}{T} \tag{2.1}$$

Another pulsing method is that of a *chirp*, the signal here has a range of frequencies determined by a start and finish parameter. A sample chirp signal is shown in Figure 2.1b, in this case a chirp is set to range from 1MHz to 5MHz, note the variable period of each wave. Using the measurements of the peaks, the signal here contains $1/0.52$μs ≈ 1.9MHz, $1/0.29$μs ≈ 3.4MHz and $1/0.22$μs ≈ 4.5MHz. These are discrete values taken from the peaks, the waves themselves contain all frequencies from 1-5MHz. This a useful option if the ideal pulse frequency is unknown, a possible application of this method is discussed in Section 4.5.

These waves exist in the time domain and would be specified when setting pulsing parameters and in signal response monitoring. Waves also exist in the space domain, once the pulses are specified and transmitted from the sensor. The waves will travel through the body under inspection, changing their characteristics according to the material they pass through. Figure 2.2 shows two 10MHz sine waves passing through 2mm of water into 2mm of steel. The incident waves through the water, after 0.6μs in blue and reflected waves after 1.7μs in orange, both have wavelength (λ) distance of 0.15μm having a wave speed of 1500m/s. These values are related using equation 2.2. The 10MHz waves travelling through the steel on the right hand side of the body have a wavelength (λ) of 0.32μm as the wave speed through this material is 3200m/s. Notice the amplitude of the wave also changes according to the material, this relates the sound pressure of the waves through the material. This pressure will fluctuate across the body according to the material properties[16]. This will remain consistent in the time domain and would not affect ultrasound measurements.

$$f = \frac{c}{\lambda} \tag{2.2}$$
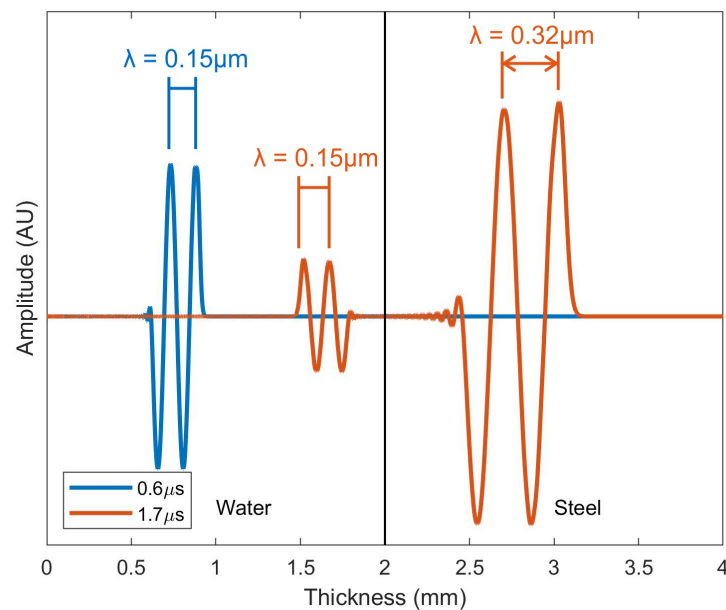
Figure 2.2: 10MHz waves in the space domain.

2.1.2 Reflections and Partial Reflections

Reflections occur when a wave encounters a material interface (Figure 2.3). The difference in material properties can be due to material density or elasticity which will affect the sound speed for these materials. Where there is a difference, the wave can partially or completely reflect, it is these reflections that provide insights into an otherwise inaccessible body. For this study longitudinal waves are used as they provide the strongest reflection response from liquid and solid material interfaces.
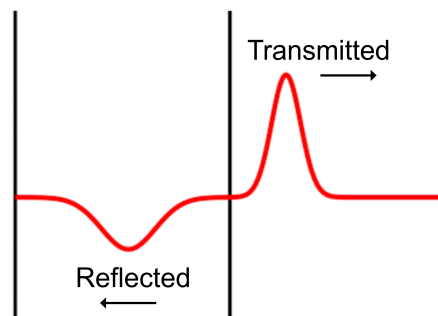
Figure 2.3: Example of a two layered body, when a wave encounters an interface (a change in material property) some part of the wave is transmitted and some is reflected.

Partial reflections occur as a travelling wave passes through layers with widths shorter than the wavelength. Similar to the waves passing through water and steel in Figure 2.2 and the simple wave encountering an interface in Figure 2.3, the waves in Figure 2.4a travel along the body intact. This is true of both the sine wave passing through the solid body in the bottom half shown in magenta, and the sine wave travelling through the single interface on the top half, shown in blue.

The difference between the wave passing through the interface is a change of phase and amplitude and the creation of a full reflection, forming a complete 'reflected' sine wave. The wave through the solid layer is unaltered. The thick white line shows the differences between the waves passing through a single layer and two layered body. This shows the change in phase and amplitude with the two transmissions being identical otherwise.

Waves have a more complex relationship with material interfaces where the waves span multiple layers such as that seen in the top half of Figure 2.4b. Partial reflections are defined in this work as 'altering' of waves as they pass through layers, an example of the wave deformation is shown in the zoomed box, notice the subtle distortion of the travelling wave as it passes through a layer boundary. There will be a reflection back
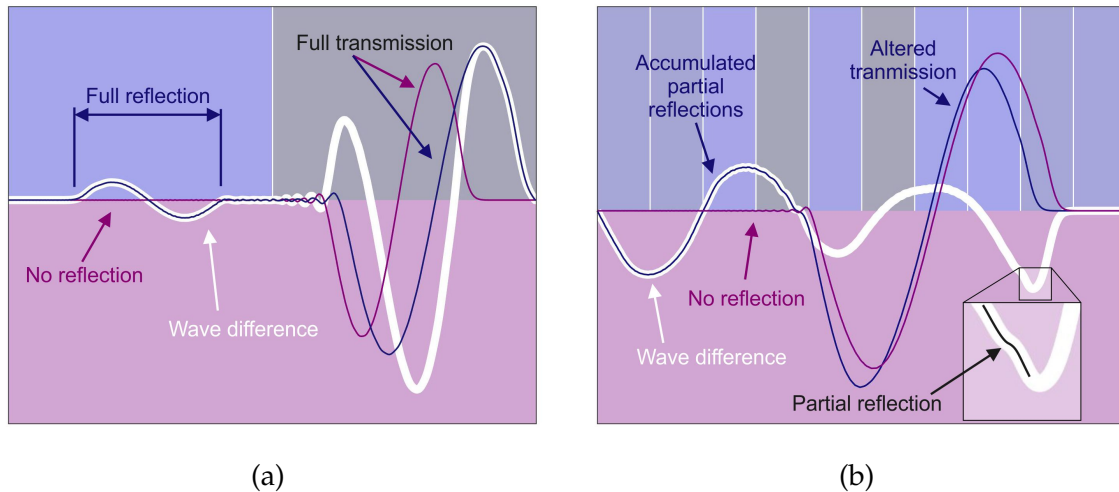
Figure 2.4: a) relationship between frequency and wavelength in pulses using cycles of sine waves and b) a chirp signal that contains a range of frequencies.

at this interface, however, as with the transmission wave the reflection is accumulated with multiple partial reflections. This creates large accumulated reflections that are difficult to interpret. The transmission wave will also alter shape through the layers, the magenta and blue waves are no longer identical apart from phase and amplitude.

2.1.3 Pulsing Methods and Wave Paths

There are various methods of transmitting and receiving waves through an object, Figure 2.5 illustrates commonly used configurations. Pulse/echo shown on the left is the simplest set up, requiring a single sensor. This halves instrumentation time and costs and also has a requirement of just one side been accessible. A draw back with this method is the excitation pulse can interfere with response signal depending on layer thickness/arrangements. Introducing a second sensor can help eliminate this problem by having separate sensors to send and receive the signal as shown in the pitch/catch arrangement in the centre of Figure 2.5. A pitch/catch configuration is also possible with sensors on opposing sides, giving a through pulse, as the right of Figure 2.5 shows. In this instance, the wave travels half the distance, so that attenuation effects are lower. It can be desirable to allow longer wave paths in some instances however, accumulating the effects of many (partial) reflections along the way. It is required that opposing sides of the object under inspection are accessible using this method.
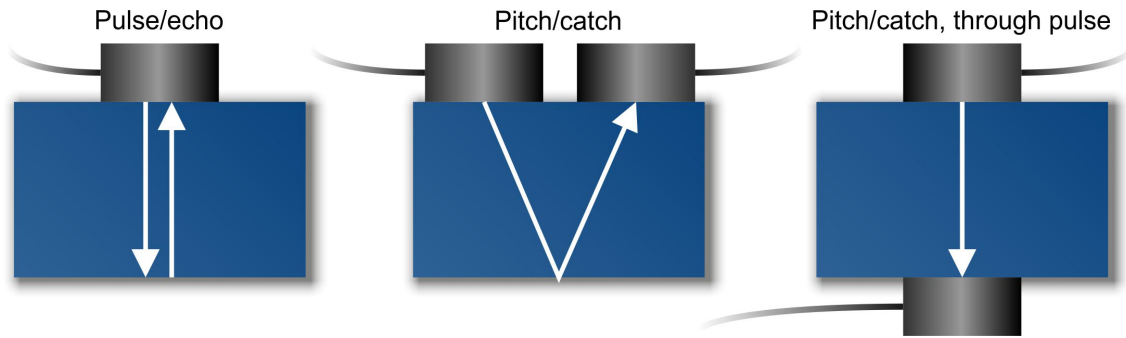
Figure 2.5: Wave paths through an object.

2.1.4 Ultrasonic Sensors

Two main types of hardware were utilised during this work to both generate the ultrasound pulse and record the returning signals. The most commonly used set up is that of commercially obtained ultrasonic transducers or 'probes', a schematic of a transducer is shown in Figure 2.6a. This shows the active element close to the sensing edge of the probe, note the large backing material behind the sensor, helping damp the signal reducing ring-down. A reduction in ring-down is highly desirable as this helps keep reflected signals clear of effects from the elements for clearer object measurements. These probes are secure in housing with connectors available for ease of wiring attachments to signal acquisition oscilloscopes.

(a)   (b)
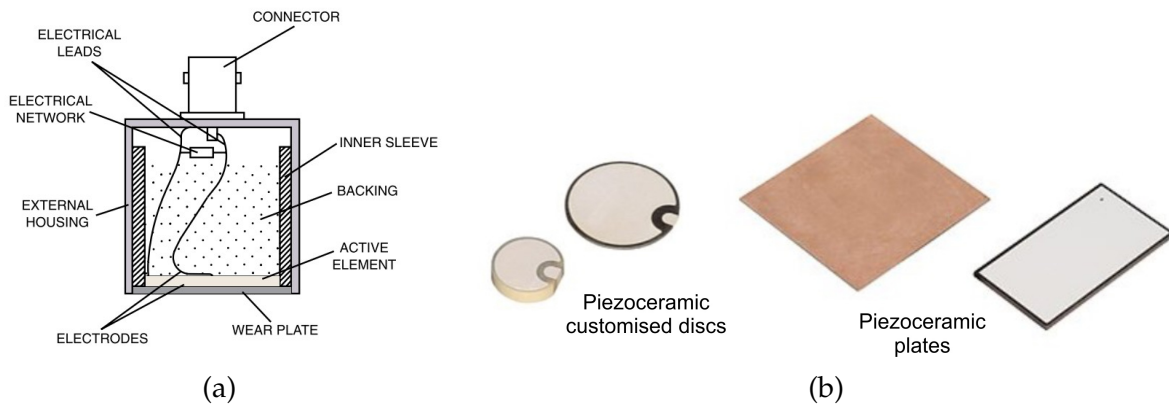
Figure 2.6: Ultrasound sensors a) ultrasonic transducer and b) piezoceramic elements.

Alternatively to commercial probes, piezoelectric elements are used to both pulse and obtain signals, shown in Figure 2.6b. Pre-cut discs are available, where the size is determined according to the parts ordered. Note these are described as customised discs due to the notched portion of the surface where there is a region separated from the

12

main surface to ground the wiring of the sensor. This wraparound design feature is required when bonding sensors to a non-metallic surface to which the sensor can not be earthed, a convenient solution when attaching sensors to the polyamide/polyethylene outer layers generally used on pouch cells.[18] Piezoceramic plates are available that can be cut to size depending on the instrumentation requirements. These plates are also available with wraparound options, making them good options for battery sensors.

These sensors are small and can be just a few millimeters length and width. The thickness of the piezo elements is inversely proportional to the frequency of the sensor, for example a 0.5MHz element would be approximately 4mm thick, whilst a 10MHz sensor would be just 0.2mm thick. The small size of these elements is an advantage of this sensor method, along with the low cost and small diameter wiring requirements.

Couplant is required to form an effective interface between whichever sensing method is used. The main function of the couplant is to flood the micro-air space that would otherwise exist between two surfaces, even if pressure is applied to the sensor. This allows the incident waves to travel from sensor into object, through the object and back into the sensor. With piezoceramic elements, the couplant is also generally used as a bonding method, securing the element to the surface, a good solution for permanent sensor attachments. Whilst ultrasound gel can be used with commercial probes, ideal for quick tests where the sensor can be moved to various positions on cells. In this case, the probes would be held in place with clamps or other specially designed holding devices. Glued attachments can be used with transducers, this is not considered ideal however as the probes are difficult to remove without damaging the sensor or cell.

2.2 Batteries

2.2.1 Principles of the Charge Cycling Process

To understand the reasons behind successful application of ultrasonic monitoring of lithium-ion batteries, understanding the process of charge/discharge at an atomic level and working this through to some approximations of the changes occurring in a cell during cycling will be useful.

In lithium-ion battery cells, lithium exists in the cathode layer. There are various lithium-ion cathode chemistries available such as lithium cobalt oxide ($LiCoO_2$) - LCO,
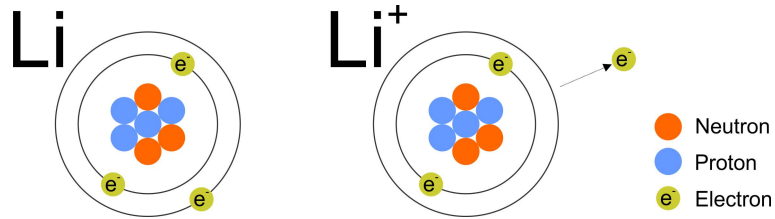
Figure 2.7: Lithium atom gives up an electron to become a lithium-ion.

lithium nickel manganese cobalt oxide ($LiNiMnCo0_2$) - NMC and lithium iron phosphate ($LiFeP0_2$) - LFP. All these types contain lithium in the cathode material. As shown in Figure 2.7 lithium (Li) atoms have 3 electrons, with one being in the outer shell, lithium will readily release this outermost electron providing a flow of charge. Once the electron is released, having a net charge, the lithium atom becomes a lithium-ion (Li^+).
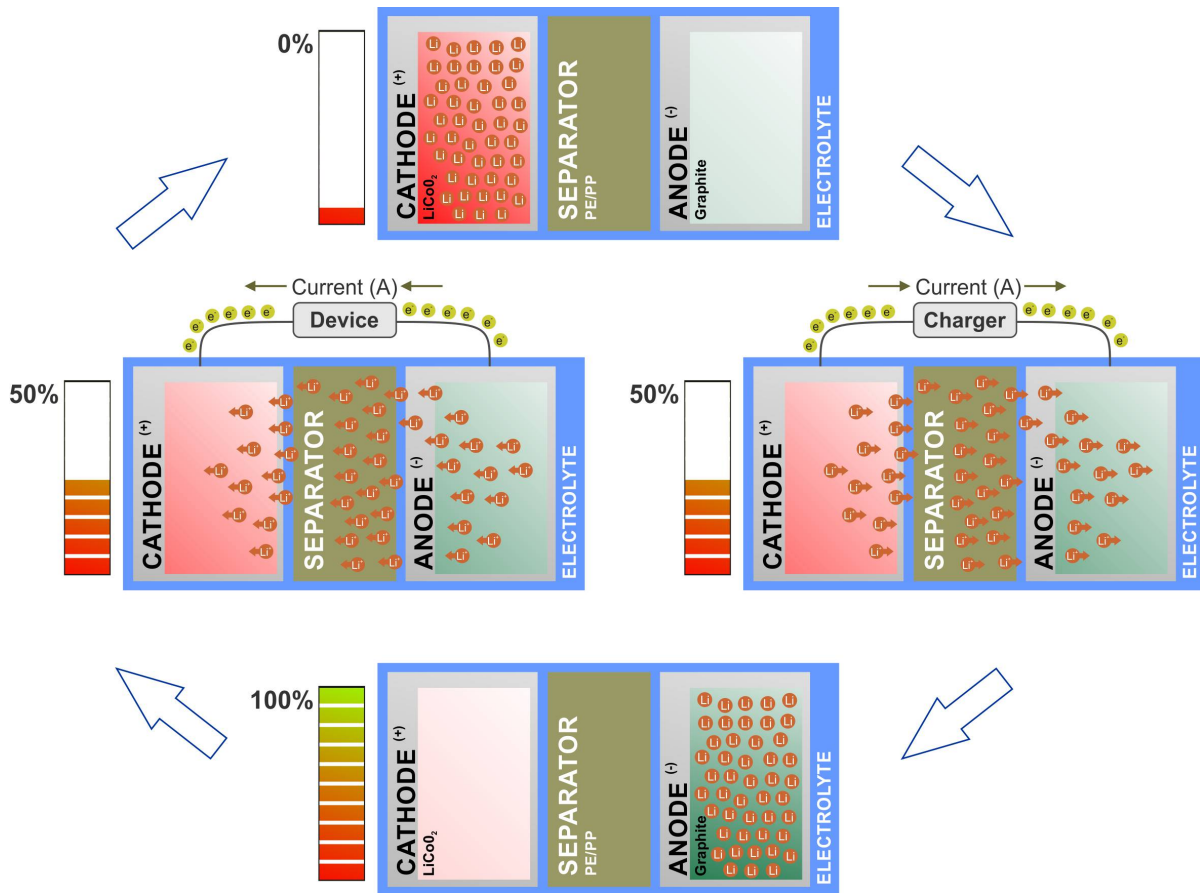
Figure 2.8: Travel of lithium-ions and electrons during charge cycling in a lithium-ion battery.

When discharged the lithium is stored in the cathode layer of the cell (Figure 2.8 -

top), during charging, current is applied and electrons will leave the cathode through the external circuit arriving in the anode layer. The lithium-ions will travel from the cathode, through the permeable separator membrane (Figure 2.8 - right), arriving in the graphite where the ions will connect again with electrons storing lithium in the anode. Once all lithium is stored in the anode, the cell is fully charged (Figure 2.8 - bottom). The battery can then be connected to a device that will cause electrons to flow in the opposite direction back into the cathode powering the device, the lithium-ions will also return back through the separator to the cathode to connect with electrons (Figure 2.8 - left). Once all lithium is back in the cathode, there can be no flow of electrons through the device and the battery is once again fully discharged.

2.2.2 Application of Ultrasonic Inspection to Charge Cycling

Using material density values given in literature[19], material weight contribution in similar cell design[18] and known dimensional values of commercial cells used during experimental tests. Estimations can be made of the changes in density distribution throughout the cell during charge cycling.

The atomic mass of a lithium atom is 6.941u which converts to approximately 1.16×10^{-26}kg. The number of electrons flowing past a point at a rate of 1 amp is 6.28×10^{18}, also known as 1 coulomb. A 2Ah cell such as those tested on during this work would see 7200 coulombs flow through a device (4.52×10^{22} electrons). As each of these electrons will connect with a lithium-ion in the electrodes, 5.24×10^{-4}kg (0.52g) of lithium is transferred from cathode to anode and back during a full charge cycle.

Further calculations can be done to verify this against some assumed parameters. Hsieh et al. state that the $LiCoO_2$ cathode has a material density of 5150kg/m^3 (discharged) to 4800kg/m^3 (charged)[19], whilst the graphite anode is 2260kg/m^3 (discharged) to 2500kg/m^3 (charged). The 2Ah commercial cells used during testing have dimensions of 62 x 42 x 7mm and a weight of 40g. Figure 2.9 has sketches of the electrodes with approximate dimensions for this commercial cell, an unknown parameter being the number of layers contained within. Herrmann state that in a lithium-ion cell, 32.9% of the total cell mass is in the positive cathode and 22.3% is in the negative anode[18]. Using these weightings a default material weight can be calculated for each electrode, the transfer of 0.52g of lithium providing a charge and discharge weight for each. These values are shown in Table 1 in columns 1-5.
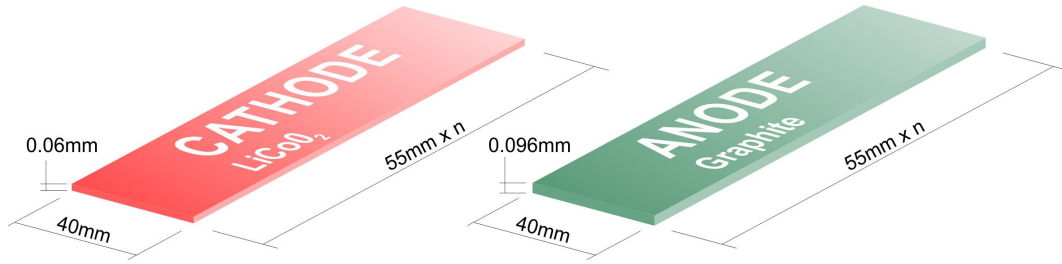
Figure 2.9: Electrode volume dimensions and number of layers in cell (n).

With the weight and density of each electrode available, the volume of each can be obtained, the cathode is calculated to have a volume of $2.68 \times 10^{-6} m^3$. Following from the volume of the cathode, the number of layers (n) can now be calculated to show approximately 20 layers. All these steps were reversed for the anode layers, starting with the volume, having thickness of 0.096mm rather than the 0.06mm of the cathode.

Table 1: Change in electrode density estimations due to lithium transportation, with respect to state of charge.

	Material weight (%)	Material mass (g)	Lithium transfer (g)	Weight (g)		Density (kg/m^3) Hsieh et al. [19]		Density (kg/m^3) Theory		Volume/ layer (m^3)	Layers (n)
				0% SoC	100% SoC	0% Soc	100% SoC	0% SoC	100% SoC		
Total	100	40									
Cathode	32.9	13.16	0.52	13.42	12.90	5150	4800	4993	4800	2.68×10^{-6}	20
Anode	22.3	8.92	0.52	8.66	9.18	2260	2500	2050	2173	4.22×10^{-6}	20

Completing Table 1 in this way shows the density range for the cathode of $4800 kg/m^3$ (the reference value for calculations) when charged to $4993 kg/m^3$ discharged. The density range for the anode is $2173 kg/m^3$ when charged and $2050 kg/m^3$ when discharged. The values are close to those quoted by Hsieh et al. [19] shown in Table 1. It was not expected the values would directly match as these calculations take values from multiple sources to make these comparisons. It is considered close enough to support the idea that the not insubstantial amount of 0.52g of lithium is moved across the battery cell during charge cycling and this is what makes ultrasonic readings of this change possible.

There are various layer construction methods inside battery cells. Figure 2.10 shows four different types, three of which are typically used in pouch cells, single stacking sheets (a), z-stacking (b) and prismatic winding or jelly roll (d). The prismatic winding or so called 'jelly roll' construction is favoured by Asian manufacturers, while European manufacturers favour the single sheet stacking. The cylindrical winding (c) is

16
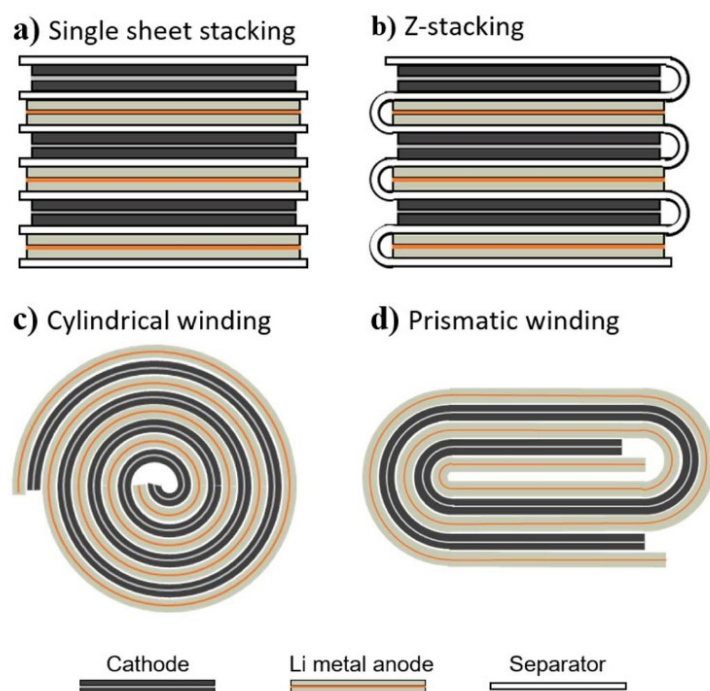
Figure 2.10: Schematic showing four typical types of Li metal batteries manufacturing processes. a) single sheet stacking; b) Z-stacking; c) cylindrical winding and d) prismatic winding[20].

utilised in cylindrical cells such as the popular 18650 lithium-ion battery.

This study has noted that the type of construction used has a direct effect on the ultrasound signal response such that the response can give clues as to which construction method has been utilised. It is possible that a certain construction type is preferable for ultrasonic inspection, this is discussed in Section 6.4.

The rate at which a battery is charged/discharged is described using C-rates. C-rates are all normalised to time, such that 1C is 1 hour, regardless of the battery capacity. Charging a 2Ah cell at 1C would take 1 hour, applying a current of 2A. When discharging a 2Ah cell at 1C, the battery will produced 2A for 1 hour. Faster charging/discharging requires higher C-rates. To charge a 2Ah cell in 30 minutes would require an applied current of 4A, a C-rate of 2C. Conversely, slow charge/discharge uses small C-rates. A 2Ah battery discharging at a C-rate of 0.1C would provide 10 hours of 200mA. A selection of sample values are shown in Table 2.

Battery capacity can be >5% lower at higher C-rates, with energy lost through heating[21]. This is problematic for ultrasound monitoring, as temperature has an effect on material wave speed. Observations and discussions around this important point take

Table 2: Sample battery capacity/C-rates.

Cell capacity	C-rate	Time	Current
	5C	12 minutes	1.05A
210mAh	1C	1 hour	210mA
	0.5C	2 hours	105mA
	5C	12 minutes	10A
2Ah	1C	1 hour	2A
	0.5C	2 hours	1A
	5C	12 minutes	60A
12Ah	1C	1 hour	12A
	0.5C	2 hours	6A

place in Sections 6.3 and 6.7.

Charge cycling is primarily performed in this work using a constant current, constant voltage (CCCV) procedure. In which a constant current is applied to a cell during charging until the cell reaches its maximum voltage. To continue charging to cell to its full capacity, reducing amounts of current are applied whilst holding the cell voltage constant. Once the applied current drops below a specified threshold the cell is considered fully charged. A schematic of the process is shown is Figure 2.11.
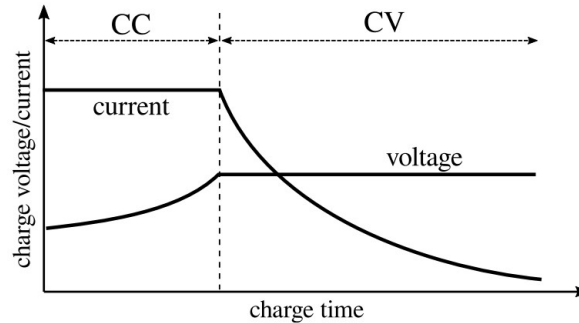
Figure 2.11: Constant current, constant voltage (CCCV) charging.[22].

2.3 Conclusions

- Higher frequency pulses provide shorter wavelengths. Pulsing higher voltage signals increases signal amplitude and can help improve signal to noise ratio. This work uses arbitrary units (AU) to record changes in signal amplitude responses.

- A boundary occurs in an object where there is a difference in material properties between two adjacent layers. When a wave encounters a boundary, some portion of the wave is transmitted and the remaining energy is reflected back. The relationship between pulse frequency/wavelengths and layer thickness is a factor, with partial reflections occurring where waves span multiple layers.

- It is calculated here that over 0.5g of lithium is transported through the layers of a 2Ah lithium-ion cell during charge cycling. This movement of material between layers alters the density profile of a cell such that acoustic waves passing through layers provide measurable responses with respect to state of charge.

3 Literature Review

This chapter contains a literature review that is presented in two parts, firstly, an overview of current battery estimation methods of which the use of ultrasound is a small sub-category. Secondly, a review of research where ultrasound measurements are used to provide battery cell insights.

3.1 Battery Estimation Methods

To assist in the care of battery usage, battery management systems have been developed to monitor battery status. Estimating the available capacity of a battery, referred to as state of charge (SoC) and the general condition of a battery, referred to as state of health (SoH) are important features of a BMS.
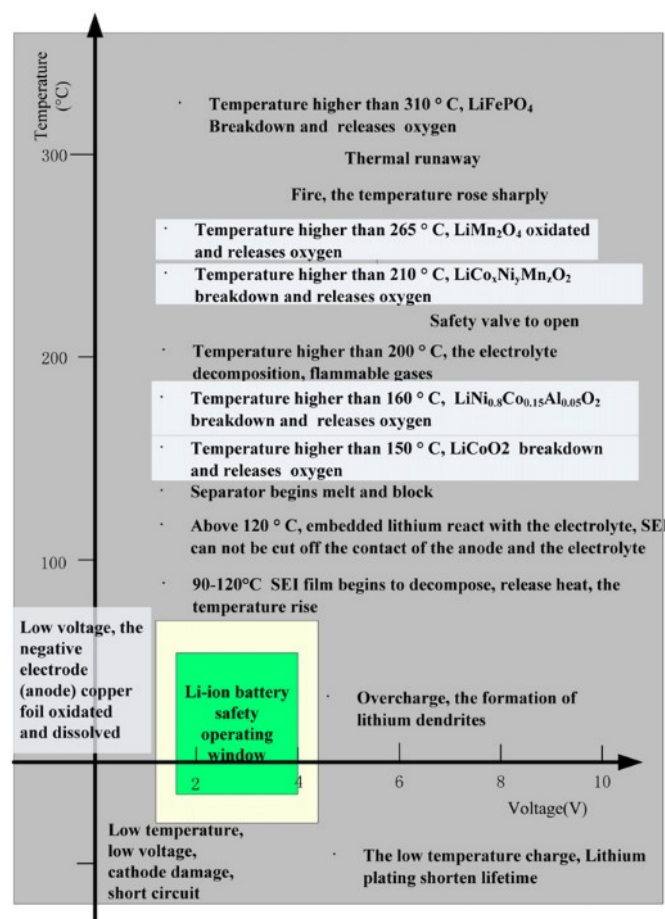
Figure 3.1: Narrow region for safe and reliable operation of a typical lithium-ion battery[2].

A key feature of usage of lithium-ion batteries is the narrow region of both reliable and safe operation. Figure 3.1 shows limits and possible effects of operation outside of this narrow region. Note that over-charging can lead to dendrite formation resulting in short circuits and safety issues and also gas build up, the definition of overcharge is when electricity is forced to flow through a battery cell beyond its designed capacity. Dendritic lithium formation is a common factor leading to short circuits in lithium-ion batteries as the dendrite growth on the anode can puncture through the separator creating a connection with the cathode. Over-discharging a battery can lead to cathode damage or short circuits as can operating at lower temperatures than those recommended. Using at higher than recommended temperatures can lead to various issues resulting in irreversible battery damage and potential thermal runaway[2,3,23].

3.1.1 State of Charge Estimation

State of charge (SoC) is generally accepted to mean the ratio of the remaining charge and the total charge at the same specified standard condition, where 100% is full and 0% is empty. Accurately estimating SoC is vital to ensure ongoing safe and reliable battery usage. The main problem being that a battery cell is a closed chemical storage source and the chemical energy cannot be access directly. Therefore, gaining any knowledge about the internal state of a battery is difficult.
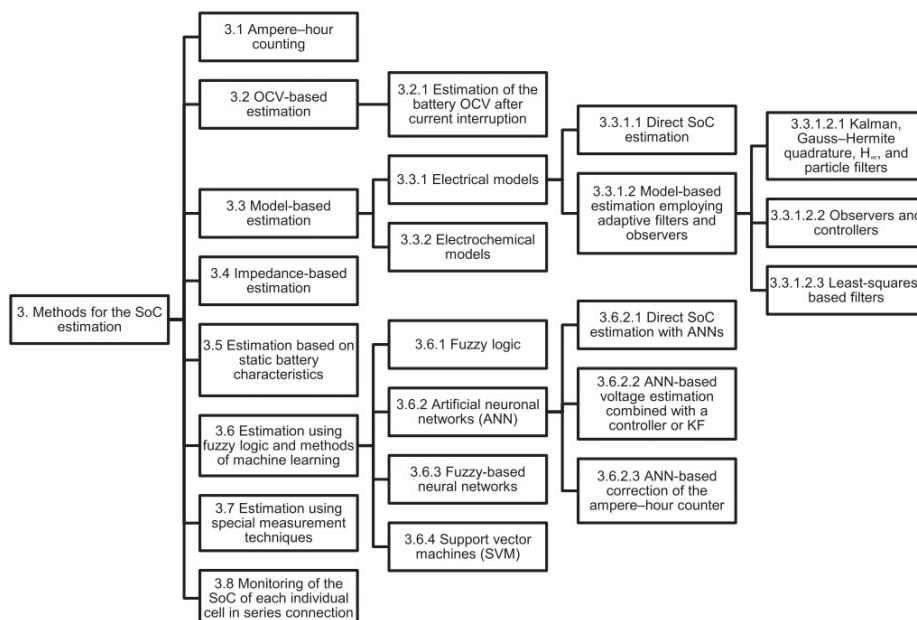
Figure 3.2: Classification of the methods for the SoC estimation[24].

There are various methods attempting to increase estimation accuracy whilst working within the limitations of accessible information from a battery cell. In a review of lithium-ion battery monitoring in electric vehicles Waag et al. (2014) state three main parameters to be monitored. Firstly, state of charge being the capacity of the battery at a given time. Figure 3.2 provides a summary of various SoC estimation methods. Secondly, impedance parameters are also estimated that provide the available power and finally state of health (SoH) estimations being the remaining useful life of the battery cell. Figure 3.3 provides a summary of available power and SoH estimation methods.

(a) Classification of the methods for the estimation of the battery impedance.

(b) Two concepts for the prediction of the battery remaining useful life; 1) concept based on the observation of battery conditions and a lifetime model, 2) concept based on SoH prediction model
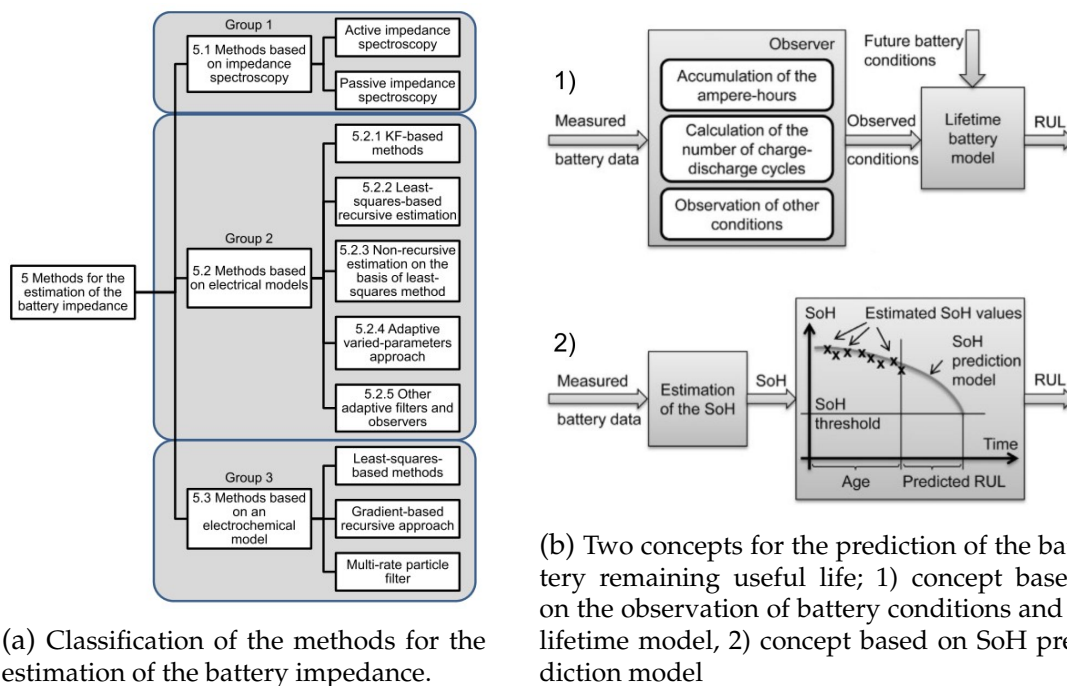
Figure 3.3: Overview of impedance and SoH estimation methods[24].

In a review paper focusing on SoC estimations, Zheng et al. (2018) explore in some detail commonly used methods such as; open circuit voltage, ampere-hour counting estimation, impedance and internal resistance based estimation, equivalent circuit model, machine learning based estimation and modern control theory estimation. Novel methods are briefly covered noting measured values in addition to terminal voltage and temperature, namely magnetic field intensity, mechanical stress and ultrasound velocity as potential methods of obtaining SoC estimations. There follows a discussion about various algorithms to reduce estimation errors in the more commonly used methods, observing a trade off between SoC estimation error and estimation method complexity, where the on board chip of a battery can prove a limiting

factor[25].

In a review by Chang (2013), SoC estimation methods are grouped into four categories; direct measurements that uses physical battery properties such as voltage and battery impedance, book-keeping estimation that uses the discharging current over time to calculate SoC, adaptive systems that are self-designing and can adjust for different discharging conditions and hybrid methods that combine and optimise various estimation methods available. Table 3 contains a summary of the four broad types of SoC estimation with some examples of each. The ultrasonic method would be included in the direct measurements category, with scope to develop measurements in a hybrid method.

Table 3: Overview of SoC estimation methods[26,27].

Categories	Mathematical method
Experimental Techniques (Direct Measurements)	Open circuit voltage method
	Terminal voltage method
	Impedance method
	EIS (Electrochemical Impedance Spectroscopy)
Experimental Techniques (Book-keeping estimation)	Coulomb counting method
	Probabilistic method
	Support vector algorithm
	Parity relation
	Sample entropy
	Big data
	Data Maps
Adaptive systems	Neural network
	Observer
	Fuzzy logic
	Least square
	Kalman filter
	EKF (Enhanced Kalman filter)
Hybrid methods	Coulomb counting and EMF combination
	Coulomb counting and Kalman filter combination
	Per-unit systems and EKF combination

In review there are many different SoC estimation methods from measured values such as ampere hour counting and open circuit voltage to modelling approaches such as machine learning algorithms and electrochemical models. Each method has benefits and disadvantages, the measured values are simple to obtain for example, but contain greater estimation errors than modelling methods which contain lower estimation errors but are complex, requiring processing time/power[25]. This makes it difficult to evaluate the overall performance of a method as in existing applications, there is a range of charge/discharge conditions and also battery type and size[26]. Section 6 fo-

cuses on the use of ultrasound measurements during charge cycling to further develop the method.

3.1.2 Battery Abuse and State of Health Estimation

Safety issues can arise during battery operation under abuse conditions of which there are three categories (Figure 3.4); mechanical abuse (crush, penetration, drop, vibration), electrochemical abuse (over-charge, over-discharge, gas build-ups) and thermal abuse (external heating, flame attack)[3,28]. Anti-abuse protection of lithium-ion batteries is inefficient according to Jiang and Zhang (2015), specifically in instances such as operating outside of recommended temperature ranges for extended periods or running the batteries with too high or low state of charge. This abuse can lead to battery failure, fire or explosion[29]. Ultrasonic monitoring of health degradation due to thermal abuse forms the basis of experimental testing in Section 7.
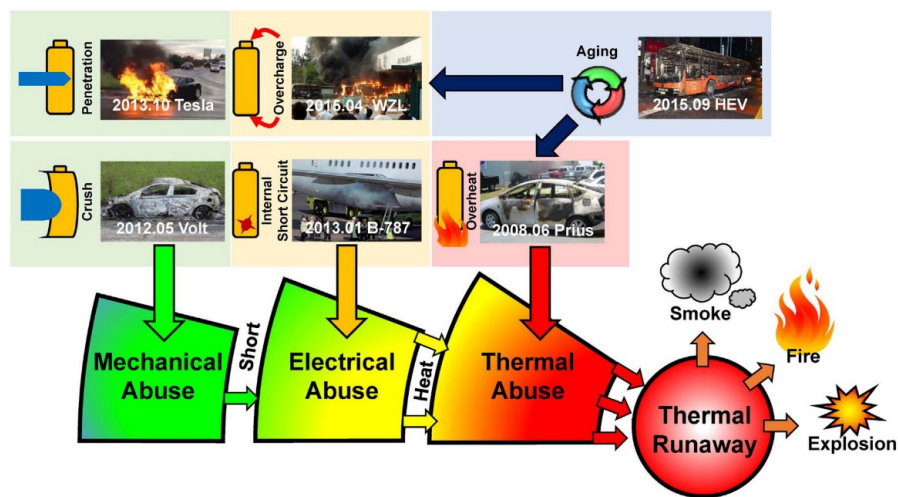
Figure 3.4: Three types of battery abuse, leading to thermal runaway[28].

The inefficiencies of anti-abuse methods where simple BMS have been applied to battery monitoring in electric vehicles has led to repeated safety incidents[29]. More attention has therefore been paid to BMS more recently, modern BMS now use algorithms to inform of battery states from external characteristics (such as voltage, current, temperature). A robust BMS can aid efficient battery utilisation to support battery usage and improve battery life, it can also offer over-charge and over-discharge prevention measures which will improve battery life and also make battery usage safer.

3.1.3 Ultrasonic Inspection in Battery Management Systems

In their 2015 book, Jiang and Zhang state that most BMS designers are electrical engineers and regard batteries as 'black boxes' and only utilise external characteristics to assess battery status. They found that these simple measuring techniques were insufficient, for example, battery packs still have shorter lifespans compared to single cells. In the case of the practical application of lead-acid batteries, it was shown that a battery pack in series had a significantly shorter lifespan than that of a single cell, it was found that the management pattern was based on the battery terminal voltage and neglected to account for the differences between cells[29].

In 2018, Zheng et al., stated that ultrasonic velocity measurements have poor feasibility for SoC estimation due to the requirement for additional sensors and accuracy doubts[25]. In a 2021 battery estimation review paper, Wang et al. give over a section to the ultrasonic monitoring method along with electrochemical impedance spectroscopy. The measured strong correlations between ultrasound signal with both SoC and SoH is acknowledged, such that these techniques are capable of providing insights into the internal structure of a battery using an external signal excitation. It is noted that results are susceptible to experimental conditions leading to poor repeatability[8].

3.2 Acoustic Battery Inspection

Since Hsieh et al. published a paper showing evidence of strong correlations between ultrasound signal and battery SoC and SoH in 2015, there has been a growing number of research papers exploring this method of battery inspection (Figure 3.5). In this section a review these papers is conducted, assessing the methodologies, findings and possibilities of the method. For quick reference a comprehensive summary of these papers is presented, in approximate chronological order, in Table 4 in section 3.2.5.

3.2.1 Equipment and Set Up Methods

Hardware choices are vital when pulsing ultrasonic waves through a body with the intention of gaining insights into the nature of the object. As seen in Section 2.1, the frequency of a wave is related to wavelength and material properties causing variations in wave speeds. As such, some care should be taken selecting sensors.
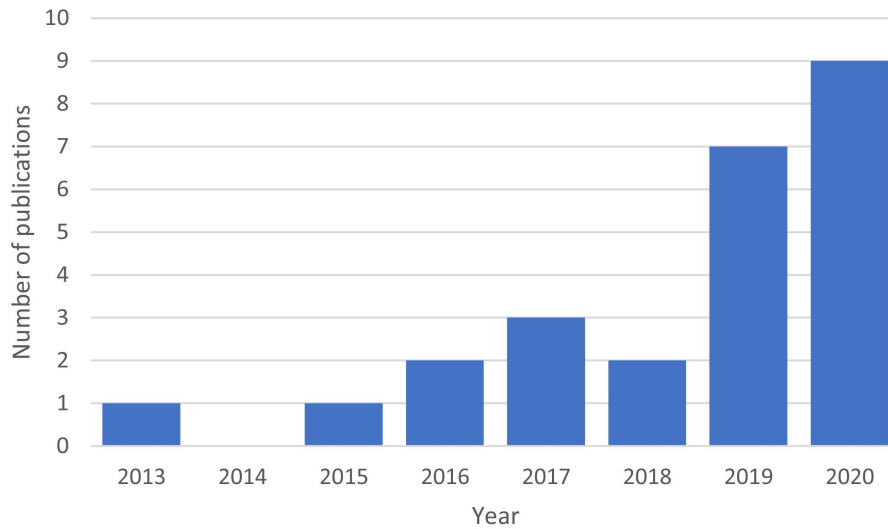
Figure 3.5: Increase in the rate of ultrasonic monitoring of batteries publications.

In the literature there are studies that have opted for 'lower' frequency pulsing from as low as 30kHz[30] up to 300kHz[31]. Some studies have decided on 'higher' frequency sensing, as high as 10MHz[32] and 15-100MHz[33]. The vast majority of studies however utilise sensors/pulse frequencies between 2MHz and 2.5MHz[34–38] with specifically 2.25MHz a common option[19,39–46]. There is little discussion around the choice of frequency across all papers, as such a discussion using modelling to simulate various frequencies pulsing through battery layers in included in Section 4.5. Here it is concluded that approximately 2MHz is confirmed as a optimum pulse frequency, balancing trade offs between cell penetration and layer accuracy.
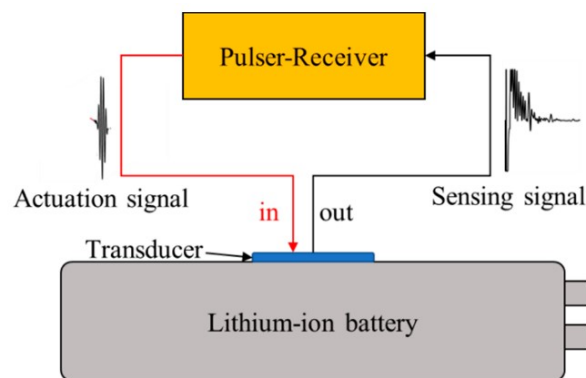
Figure 3.6: Example of a pulse/echo, single sensor test configuration (Wu et al.)[47].

The wave path presents important decision making choices in setting up experimental testing. As shown in Figure 2.5, pulse/echo requires a single sensor, both emitting

26

and receiving ultrasonic waves. A pitch/catch set up requires at least two sensors of which one will transmit the signal with a different sensor set to receive the waves. In battery monitoring literature, there is a small number of studies using a pulse/echo configuration[19,41,42,47,48]. An illustration of a pulse/echo test is shown in Figure 3.6.

More specialised wave paths such as guided waves[36,49] and waves transmitted across the cell surface[30] have been used. However, the most popular pulsing method was the use of a through pulse, utilising two sensors on opposing faces of the cell, one to transmit the signal with the receiving sensor receiving the wave[19,31,34,35,37–40,43–45,50–53]. This provides a logical guarantee, that the received wave has successfully passed through each layer at least once. This is not necessarily true of a pulse/echo configuration, where the received signal is open to interpretation. A schematic illustration of a pitch/catch, through pulse test set up is shown in Figure 3.7. Most experimental testing in this work was performed using a single sensor pulse/echo arrangement. However, some testing was conducted using a dual sensor, through pulse set up the comparative results of which are discussed in Section 6.6.2.
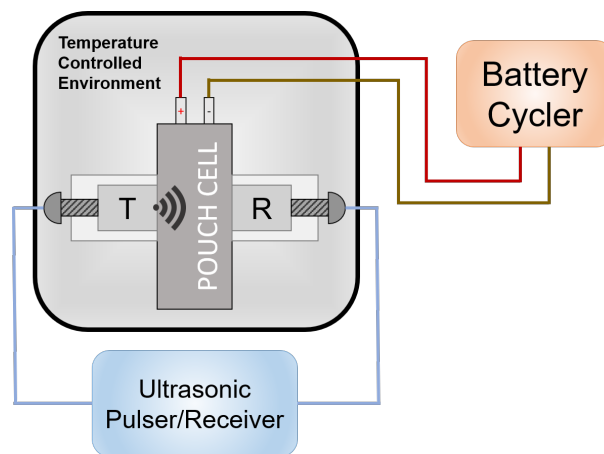
Figure 3.7: Example of a pitch/catch, two sensor through pulse test configuration (Hodson et al.)[38].

A final important consideration regarding instrumentation is that of the hardware itself. Commercial probes remains the most common sensor type used in ultrasonic battery monitoring literature with most studies opting for this sensor solution. Deviations from this include studies using ceramic/brass piezo elements[36,51,52], these tended to be in the lower frequency ranges of 120-500kHz. Another option is to use piezoelectric disc transducers or sensors cut from piezoelectric plates[30,47,49,54], sensors of this nature are small, cheap and easily bonded to the surface of a battery. Examples of com-

mercial probes and bonded piezoelectric elements are shown in Figure 3.8. Work in this thesis generally utilised commercial probes for the standard charge testing in Section 6, obtaining high quality results leading to strong ultrasound response/SoC correlations. Bonded sensors proved challenging to obtain comparable signal quality in this work, particularly during the thermal abuse experiments in Section 7. It is considered that the superior signal quality of commercial probes is the reason behind the popularity in battery/ultrasound research currently.

<div align="center">(a)   (b)</div>
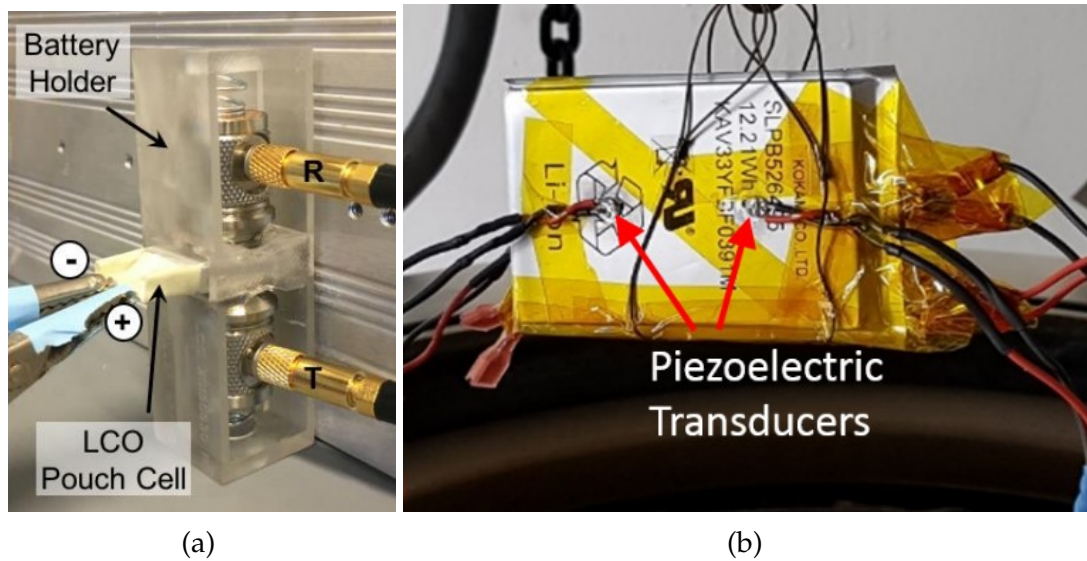
Figure 3.8: Sensor types a) Commercial probes in custom 3D printer holder[35], b) Bonded piezoelectric disk transducers[36].

Most studies use glue, gel or resins as couplant. There are examples of more specialised test arrangements, such as air coupled transducers[53,55], focusing transducers[34] and oil filled containers for optimal acoustic transmittance[46]. In this work, gel and glue are used for commercial probe attachment, comparisons of which are made in Section 6.6.1 . Epoxy resin is used when bonding piezoelectric sensors to a cell.

3.2.2 Battery Types and Test Parameters

Three main considerations were commonly stipulated in the literature; the battery type and capacity to be subjected to ultrasonic inspection, the charging cycle design and the temperature conditions of the experiments.

Pouch cells were used in the majority of studies using ultrasound, the capacities of which tended to be small, ranging from 0.21Ah[35,37,41–43,45] to 3.3Ah-3.6Ah[36,49,54]. A

small number of studies focused on larger capacity cells ranging from 6Ah to 36Ah capacity[30,53,55]. The experiments contained in this work are primarily focused on commercially obtained pouch cells having a capacity of 2Ah, although there is some methodology testing on large capacity, 52Ah cells in Section 6.7. The specific chemistry of test cells is not considered in this study. This decision is based on the assumption that the ultrasound detection method is applicable to all chemistry types, all sharing the fundamental principle of material transfer during charge cycling and physical features such as gassing and swelling during abuse conditions. Apart from standard pouch cells, further studies have used ultrasound to measure vanadium redox flow batteries[31], prismatic cells[48] and bespoke pouch cells with defects deliberately built in[32], to assess the capability of detection using ultrasound.

For charge cycling tests, most experimental designs for cell utilised CCCV charge procedures. This was either done in small number for SoC testing[31,51] or large number for SoH tests[34,47,50]. The C-rate used across the literature was generally within expected manufactures guidelines, ranging from 0.1C[30,49] to 1C[30,41], with 0.5C commonly used[31,37,40,50].

The temperature conditions of testing throughout the research is generally unspecified unless cell temperature is a specific part of experiments. For example, where a cell is transitioned between set temperatures to monitor ultrasound reactions[35], thermal abuse tests[36] and temperature monitored tests[30]. There are studies that state constant temperature values and ranges; 25°C[53], 30°C[49,54] and 25°C-30°C[41]. Other papers state the tests were run at room temperature[19,50,51], remaining literature make no reference to temperature. As it is known that temperature, along with density/elasticity effects the speed of sound of a material. Standard testing in this thesis records the surface temperature of the cell. This is assessed to determine the effect on ultrasound response and to what degree it occurs.

3.2.3 Standard Testing

This section covers studies using ultrasound to monitor cells during standard testing conditions such as charge cycling or battery ageing tests. There are several studies using ultrasound wave responses to monitor battery state of charge. The first of which was published in 2015 by Hsieh et al., showing that the state of charge of a battery cell could be monitored using ultrasound time of flight measurements. They state that the

density distribution within a battery cell must change according to state of charge, this would be correct regardless of chemistry and that the field had lacked a non-invasive, field deployable method for battery cell live monitoring.

Changes in density and elastic modulus of the electrodes occur as functions of the state of charge of the battery, where the rate of these changes can also provide information of battery state of health. A model to simulate battery charge cycling and the acoustic effects was created using Clawpack, the changes in SoC were managed using Dual-foil to estimate density changes in each electrode. In the model the modulus was held constant and only density changes were considered, however it is acknowledged to be likely that the modulus will have an effect on the signal in reality. The modelling contained in this thesis in Section 4 takes the same approach with wave speed of materials being a function only of density. The development of modelling would aim to support the inclusion of elasticity in future work.
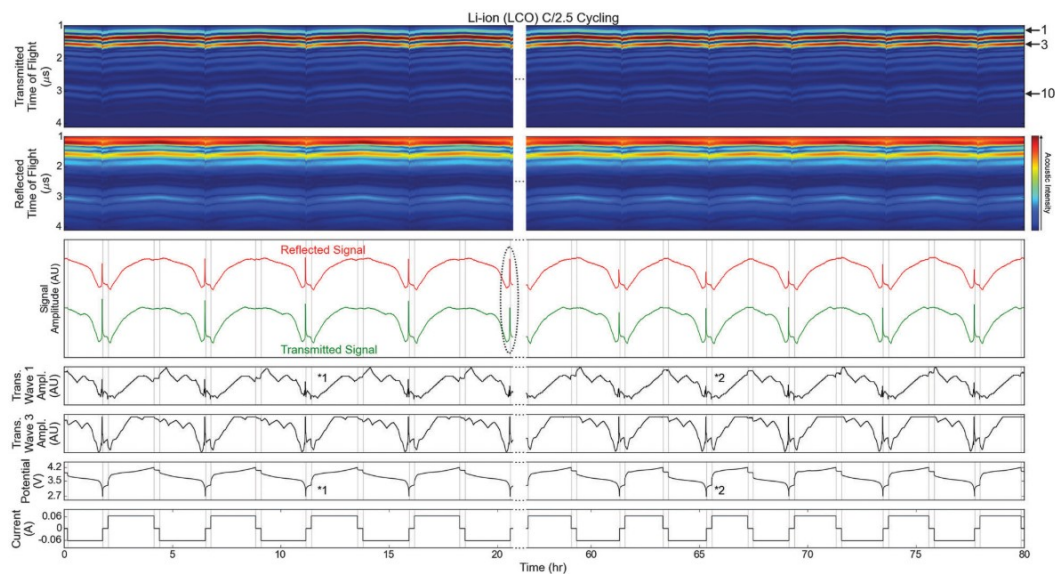
Figure 3.9: Charge cycling effects on ultrasound acoustic response in battery model simulation (Hsieh et al.)[19].

Figure 3.9 shows a measurable shift in time of flight and signal intensity (amplitude) in the simulation, both of which are functions of battery state of charge. During charging it was observed that ToF peaks shifted towards lower values whilst the intensity (amplitude) of the signal increased, the opposite being true during discharge. It was also noticed when comparing transmission peaks 1, 3 and 10 in the top panel of Figure 3.9 that the ToF shift is more pronounced in later signal regions and signal amplitude has reduced intensity[19]. This will become a recognisable feature in experimental testing

in Section 6 with later waves featuring a trade off between richer measurements caused by greater number of transmission/reflection events and decreasing amplitude due to signal attenuation.

The method of visual data synchronisation presented in Figure 3.9 is the template for data analysis performed in the work contained in this thesis. Particularly the time/time intensity plot that shows the evolution of a signal response over the course of a test. Hsieh et al. makes references to correlations in their paper which are noted from visual inspections, they do not extract any data to show precise coefficients measuring the relationship.

Correlations with SoC and ultrasound measurements are calculated by Gold et al. in their 2017 paper. They found that pulsed ultrasound signals are sensitive to changes in porosity of the graphite anode during charge/discharge and therefore to SoC. The 200kHz pulse produced two wave packets that are received when the cell is fully charged, shown in Figure 3.10a. It was found that the first wave remained unaltered during charge cycling whereas the second wave packet shows a dependence on SoC. Additionally, the second wave packet shows a delayed ToF that also correlates with SoC as shown in Figure 3.10b[51]. Chang et al. obtained similar results using 'Biot's fluid-saturated porous media model' and air-coupled sensors, although they found that both the fast and slow waves had an almost linear relationship with SoC[53]. Taking measurements from an envelope of the modulus of the signal, similar to the processing method used by Gold et al. was including in the analysis options developed during this study. The comparative results of which are discussed in Section 5.2.
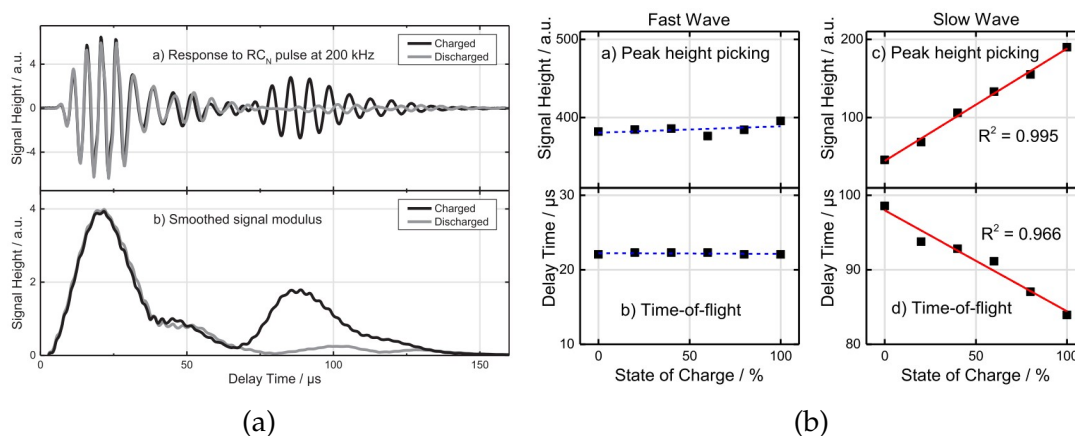
Figure 3.10: a) change of ToF and signal amplitude and the relationship with battery SoC and b) correlations of SoC with fast and slow waves (Gold et al.)[51].

In other ultrasound/SoC studies, it was found that ultrasound velocity exhibits variations in accordance with changes in composition of vanadium-ion in the positive electrolyte solution of vanadium redox flow batteries. The accuracy of this method was robust having just $\pm 2\%$ errors compared with predicted values[31]. Shifts in ToF and signal amplitude in relation to battery SoC and SoH were observed by Davies et al.. Developing battery reporting using the ultrasound data, a machine learning model was created to predict the SoH with approximately 1% error margin[40]. Ladpli et al. claim to measure SoC and SoH with greater accuracy using guided waves across the surface of the cell[49]. Spatial characterisation of cells during fast-charging was accomplished by Chang and Steingart. In this recent publication, amplitude attenuation of ultrasound signal is processed to visualise the varying extent of graphite lithiation at different locations on the pouch cell[46].

Acoustic ToF is measured against cell charge cycling by Robinson et al., analysis of the signals suggested that stresses are generated in electrodes during charge cycling with the Young's modulus of material being a function of the SoC and applied current[41]. During analysis, single peaks were isolated and studied as shown in Figure 3.11a. Popp et al. also used ultrasonic ToF measurements to detect changes in SoC, in their signal processing work, amplitude based Schmitt-triggers isolated potential regions of interest, shown in Figure 3.11b.

(a)   (b)
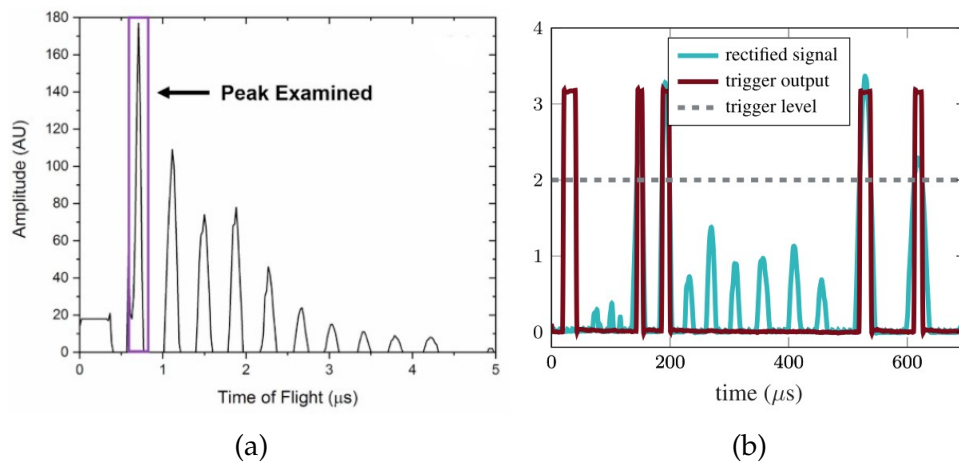
Figure 3.11: Signal processing methods a) example of a rectified acoustic signal, with the investigated peak highlighted (Robinson et al.)[41] and b) input pulse and rectified signal response with Schmitt-trigger output (Popp et al.)[30].

A common theme throughout the literature is a lack of discussion of from which part of the signal measurements should be taken. It often appears that the largest is assumed

to be optimal due to the obvious properties of best signal to noise ratio. It developed into a key part of the work in this thesis to understand the nature of wave responses with the aim of identifying if all parts of a wave response contain equal battery insights and if not, which peaks perform best and how can they be identified.

Along with a study by Ladpli et al., which used ultrasonic guided waves and a matching pursuit technique to estimate SoC and SoH of lithium-ion cells, some of the papers mentioned above also used their ultrasound experiments to monitor cell health along with charge cycling[19,40,49]. In the 4th panel of Figure 3.9, labelled *'Trans. Wave 1 Ampl. (AU)'*, a peak in the amplitude of the first wave evident in the 3rd cycle (*1) has disappeared by the 15th cycle (*2) which is believed to have been an indicator of the cell accepting less charge[19].

In an early study in 2013 by Sood et al., ultrasound pulses are used to non-destructively evaluate the internal condition of a lithium-ion cell. This was thought to be possible due to gassing evolution through continued cycling, causing the wave response to become slower (larger ToF) and more shallow, shown in Figure 3.12a[50]. A study by Wu et al. exclusively focused on the use of ultrasound to monitor the health of lithium-ion batteries. They found that the ToF was highly related to the underlying material degradation, shown in Figure 3.12b. Using data fusion methods to fuse ultrasound signal and temperature, they were able to successfully monitor the health of lithium-ion cells[47]. Measuring effective stiffness of active storage materials using accurate cell thickness measurements and recorded wave arrival times is possible using ultrasound pulses, improving SoC and SoH estimations[45].

| (a) | (b) |
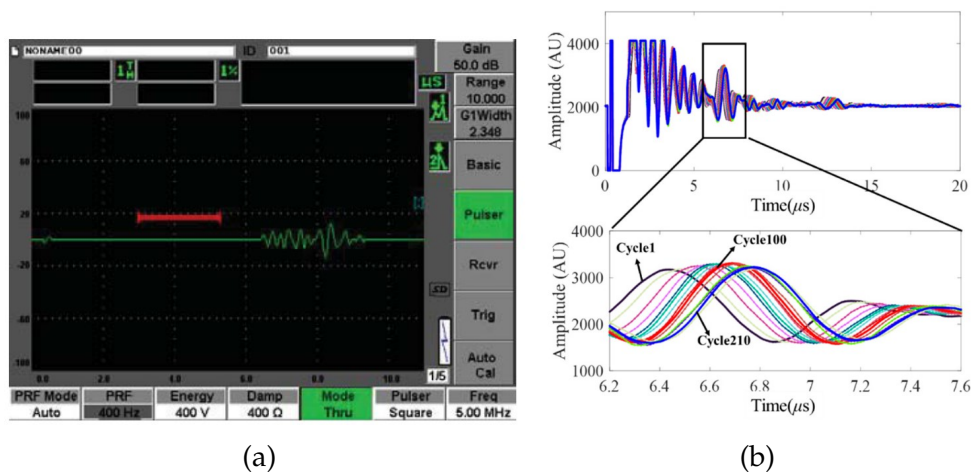
Figure 3.12: State of health monitoring a) increased ToF and reduction in amplitude Sood et al.[50] and b) increase in ToF Wu et al.[47].

3.2.4 Non-Standard Testing

A review of ultrasound monitoring during non-standard testing is conducted in this section. This will cover more specialist studies such as cell abuse[36,52] and feature/defect detection[32,43]. Utilisation of ultrasonic inspection being the common theme throughout.

A study by Bhadra et al. finds that changes in the ToF measurements taken in AA batteries during discharge, correlate with changes occurring in the anode layer. This important step means the author is able to take the correlations and start to make claims about the underlying physical changes[39]. Robinson et al. used spatially resolved ultrasound measurements to analyse the condition of lithium-ion electrodes. They state that acoustic peaks in the reflected signal are indicative of interfaces between different materials and note that in the received signal each peak is a doublet (two peaks close together), shown in Figure 3.13a. It is not clear how the study confirms that each wave response is locating an interface, the method for discounting the multiple reflections as the initial wave travels deeper into the body is not explained. They do state however, that the reduction of the first peak of the doublet and increase of the second peak suggests they can be ascribed to the cathode and anode respectively. They note that the presence of even a small amount of gas would impede the signal significantly and would therefore be an identifiable problem from the ultrasound response. The variations in ToF across the battery cell are shown in Figure 3.13b. There is a region of significant interest at the top where the red area is, this is around the anode current collecting tab suggesting that the tab inhibits the expansion of electrode layers causing a contraction of layers[48].

(a)

(b)
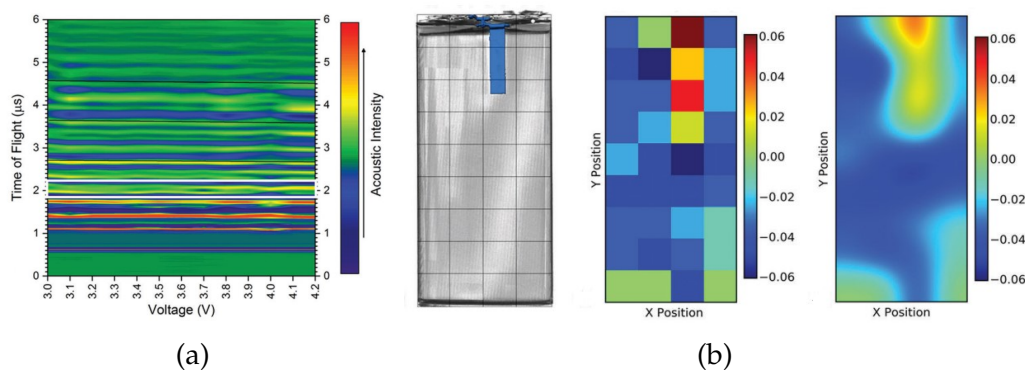
Figure 3.13: Typical ultrasound response and spatially resolved ultrasound measurements across battery surface; a) Ultrasound response at a specific point on the surface and b) variation in ToF across battery surface[48].

34

Gassing build up, referred to as stomata defects have been detected using ultrasonic inspection methods in lithium-ion batteries. The method can successfully detect the stomata defect and also determine the location of the defect with respect to the sensor, based on the change in signal amplitude[55] (Figure 3.14a). Gassing occurring in cells is also detected through loss of signal, along with solid-electrolyte-interphase (SEI) formation during cycling (Figure 3.14b). The location and scale of the defects deliberately introduced to the layers of a cell, such as the dissolving of active cathode material using solvent, was possible using ultrasound measurements[32]. Shifts in ToF has been shown to correlate with increase in silicone in the silicone/graphite mixture in the anode in NMC/SiGr composite pouch cells and lithium plating in conventional lithium-ion batteries[43,44]. The use of higher frequency pulses 15MHz and 100MHz were used in a paper published by Bauermann et al., to successfully detect various defects (Figure 3.14c)[33]. The defects visualised using scanning acoustic microscopy (SAM) included electrolyte leakage, faulty electrodes and gas accumulation in coin cells. The potential use of high frequency pulses similar to those used by Bauermann et al. are discussed in Section 4.7, where it is suggested that obtaining resonances from the various active layers may provide electrode insights during charge cycling.

(a)   (b)   (c)
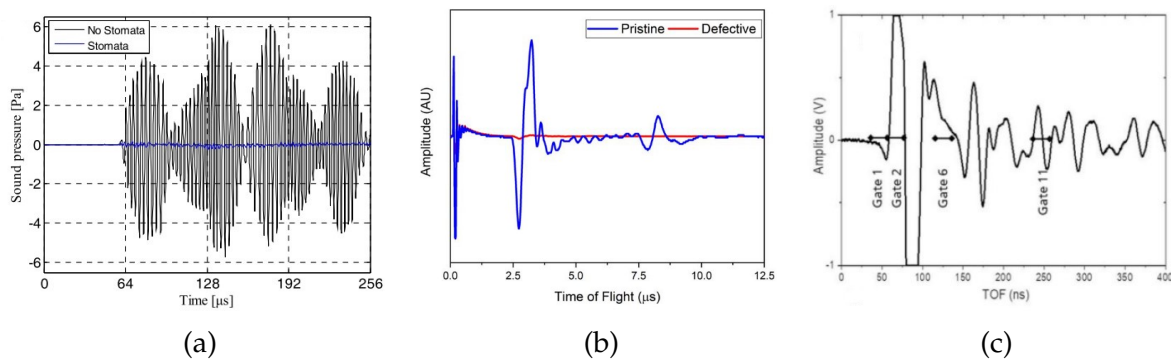
Figure 3.14: a) Transmission signals of intact and defective models with the stomata defect in the fifth electrolyte layer of the lithium-ion battery Li and Zhou[55], b) Ultrasonic ToF waveforms from pristine and defective cells (Robinson et al.)[32], c) Representative reflectogram using a 100MHz transducer at the center of a CR2032 coin cell (Bauermann et al.)[33].

Electrical abuse tests, specifically the over-charge/discharging of a prismatic cell were conducted by Oca et al.. Ultrasonic characterisations of the cells during testing confirmed irreversible damage to the cells under abuse conditions. Importantly, these changes could not be seen using the three parameters commonly used in BMS; cell voltage, current and temperature ratings[52].

The effects of significant shifts in temperature were explored by Chang et al.. In their

study, they demonstrate the adverse effects transitioning from low to high temperatures can have on commercial lithium-ion batteries (Figure 3.15a). Ultrasonic monitoring of cells during tests shows an exponential, Arrhenius relationship between acoustic attenuation and the magnitude of temperature shifts. It is concluded that the ability to monitor temperature shift effects this way could aid systems designed to reduce risk of cell failure[35]. Electrode delamination due to gas formation during thermal runaway has been detected using ultrasound attenuation monitoring and shifts in signal peaks (Figure 3.15b)[42].

(a)   (b)
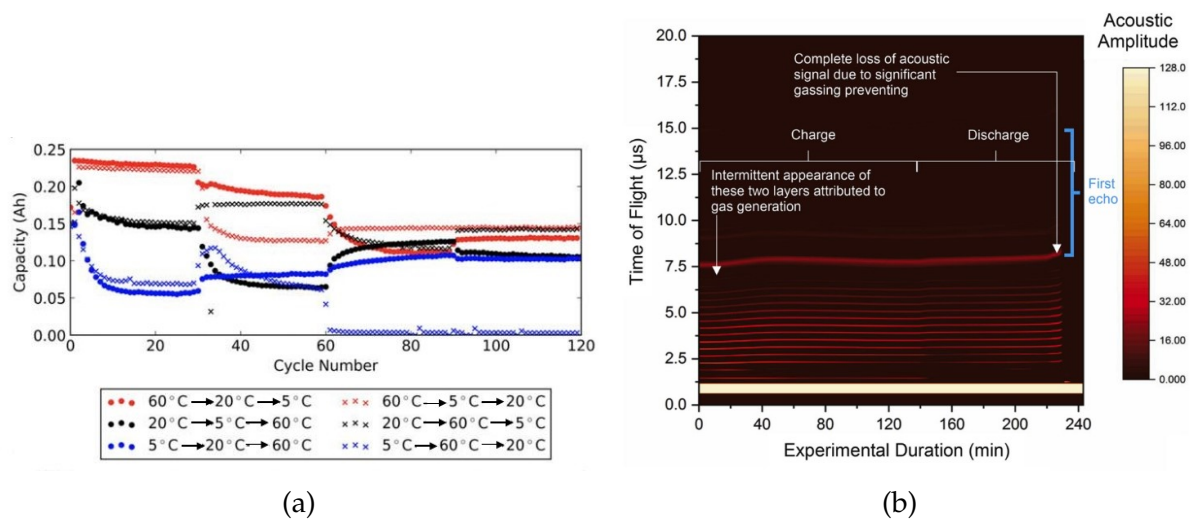
Figure 3.15: a) Cells cycling at six temperature permutation profiles; 5°C, 20°C and 60°C (Chang et al.)[35] and b) ultrasound response intensity plot (Pham et al.)[42].

Ultrasound measurements of lithium-ion batteries during high temperature, thermal abuse conditions conducted by Zappen et al. show that it is possible to observe degradation effects in real-time. Features are identified in the signal intensity and signal center of gravity (a method of tracking wave speeds through a body), with the center of gravity parameter in particular appearing highly sensitive to degradation and gassing processes such as SEI dissolution and evaporation of solvents. Having non-invasive, real-time access to this information is thought valuable for use in the application of battery management systems[36].

In other specialised experiments, ultrasonic monitoring has been used to provide insights into lithium-ion concentration, accumulation and depletion at the electrode/-electrolyte interface[38]. Ultrasonic imaging has been found to be sensitive to wetting and unwetting in lithium-ion pouch cells, an example 'unwetted' image is shown in Figure 3.16a. Unwetting occurs where the electrode active layers swell to the extent

(a)

(b)
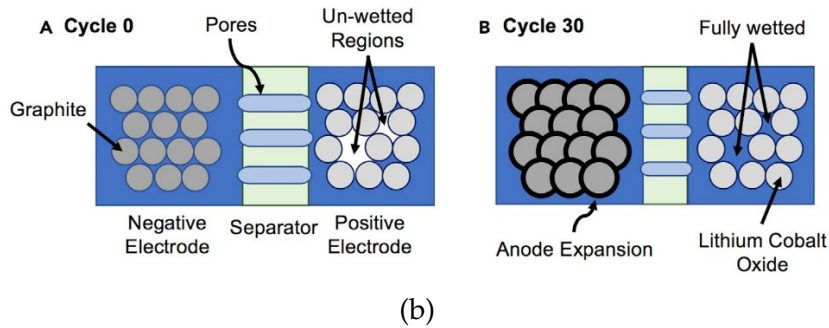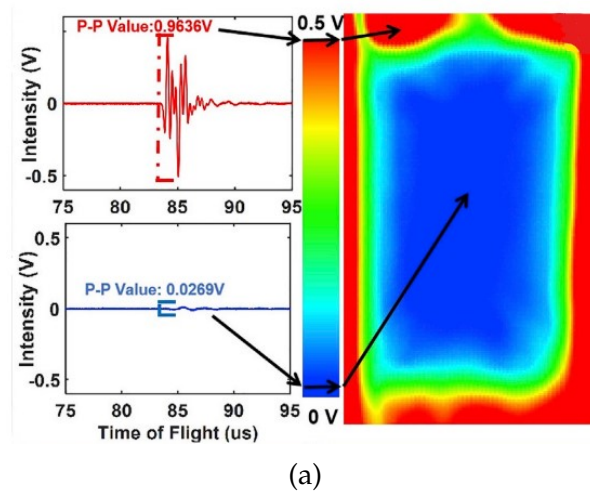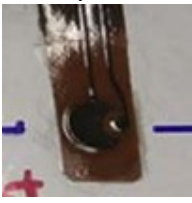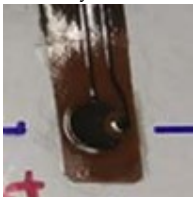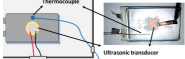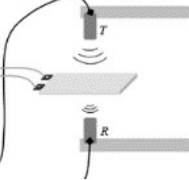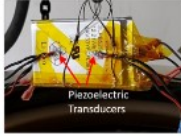
Figure 3.16: a) Ultrasonic transmission waves at the positions marked by arrows and ultrasonic transmission image of a dry single layer cell (Deng et al.)[34] b) Schematic of the proposed electrolyte wetting process (Knehr et al.)[37].

electrolyte no longer fills the expanded pore space (Figure 3.16b), a characteristic observed in aged cells[34,37]. There is a break-in period before a cell stabilises caused by swelling in the graphite anode. The increase in pressure causes wetting in the cathode. These physical changes in the anode affecting the electrochemical performance of the cathode is known as crosstalk. Ultrasonic ToF measurements measure this break-in period[37].

3.2.5 Compilation of Published Work

Authors, *title/aim of work*	Conclusions/analysis	Test parameters	Sensor type
2013			
Sood et al. (2013) [50] *Health monitoring of lithium-ion batteries*	Signal amplitude, delayed pulse due to degradation of interfaces after cycling	Pulse frequency: 5MHz Wave path: Pitch/catch - through Cell type: Li-ion Charge type/rate: CCCV / 0.5C Temperature: Room temperature	Transducer
2015			
Hsieh et al. (2015) [19] *Battery charge and health correlation with electrochemical-acoustic time of flight*	Strong correlation between SoC and density distribution. Time of flight shifts and amplitude changes	Pulse frequency: 2.25MHz Wave path: Pulse/echo, pitch/catch - through Cell type: Prismatic & 18650 cell Charge type/rate: CC-rest/ 0.4C Temperature: Room temperature	Transducer
2016			
Chou et al. (2016) [31] *State of charge monitoring of vanadium redox flow battery using ultrasound velocity sensing*	Ultrasound velocity in electrolyte solution is dependent on both temperature and concentration	Pulse frequency: 300kHz Wave path: Pitch/catch - through Cell type: Vanadium redox flow Charge type/rate: CCCV / 0.5C Temperature: Measured value	Ultrasonic velocity sensor
Bhadra et al. (2016) [39] *Anode characterization in AA Alkaline batteries using electrochemical acoustic time of flight*	Many correlations between ToF and scanning electron microscope (SEM) and energy-dispersive X-ray diffraction (EDXRD)	Pulse frequency: 2.25MHz Wave path: Pitch/catch - through Cell type: Zn/MnO_2 alkaline LR6 (AA) 2.85Ah Charge type/rate: 0.14, 0.1, 0.07 & 0.05C	Transducer
2017			
Gold et al. (2017) [51] *Li-ion batteries SoC using ultrasonic transmission*	Checked at different C-rates. 2 waves, 1 fast, 1 slow, slow wave correlates with SoC	Pulse frequency: 200kHz Wave path: Pitch/catch - through Cell type: 1.2Ah pouch cell Charge type/rate: CC / 2C and 4C Temperature: Room temperature	Ceramic / brass Piezo elements
Davies et al. (2017) [40] *SoC & SoH estimation using electrochemical acoustic ToF analysis*	Cross correlation measurements, time of flight and total signal amplitude values for SoC/SoH	Pulse frequency: 2.25MHz Wave path: Pitch/catch - through Cell type: LCO & LFP pouch cells Charge type/rate: CCCV / 0.5C	Olympus transducers
Ladpli et al. (2017) [49] *Li-ion battery cycling behavior using US ToF*	Changes in waves provide indication if physical processes. ToF and amplitude vary as a function of battery aging. SoC/SoH predicted on demand, without prior history	Pulse frequency: 100-200kHz Wave path: Pitch/catch- guided waves, four paths Cell type: 3.65Ah Li-ion pouch cell Charge type/rate: CC-rest / 0.1C Temperature: Constant 30°C	Piezoelectric disc transducers PZT-5A smart layer format
2018			

Authors, *title/aim of work*	Conclusions/analysis	Test parameters	Sensor type
Ladpli et al. (2018)[54] *SoC & SoH estimation with US using matching pursuit technique*	Framework for applying novel signal processing	Pulse frequency: 100-200kHz Wave path: Pitch/catch- guided waves, four paths Cell type: 3.65Ah Li-ion pouch cell Charge type/rate: CC-rest / 0.1C Temperature: Constant 30°C	Piezoelectric disc transducers PZT-5A smart layer format
Knehr et al. (2018)[37] *Understanding Full-Cell Evolution and Non-chemical Electrode Crosstalk of Li-Ion Batteries*	Swelling of the anode, caused by side reactions increases pressure. This increase forces electrolyte to wet previously inactive parts, lowering the cell impedance	Pulse frequency: 2.5MHz Wave path: Through pulse Cell type: 0.21Ah Li-ion pouch cell Charge type/rate: CCCV / 0.5C	Transducers
2019			
Robinson et al. (2019)[48] *Spatially resolved ultrasound Li-ion diagnostics*	Change in density of electrodes visualised. Current collecting tab inhibits movement of electrode layers	Pulse frequency: 5MHz Wave path: Pulse/echo - various positions Cell type: 2.8Ah prismatic cell Charge type/rate: CCCV-rest / 0.35C	MR110-RM transducers
Robinson et al. (2019)[41] *Li-ion battery cycling behavior using US ToF*	Variations in ToF indicate presence of stresses. ToF consistent at the temperature extremes during cycling	Pulse frequency: 2.25MHz Wave path: Pulse/echo Cell type: 0.21Ah LCO cell Charge type/rate: CCCV / 1, 2 & 4C Temperature: Measured using thermal imaging 25-30°C	MR110-RM transducers
Wu et al. (2019)[47] *Ultrasonic health monitoring of Lithium-Ion batteries*	Strong dependence between ultrasound ToF and battery degradation. Potential for overcharge battery failure early indication, ultrasound indicates earlier than swelling or temperature	Pulse frequency: 1MHz Wave path: Pulse/echo Cell type: 1.8Ah & 0.7Ah LCO pouch cells Charge type/rate: CCCV 0.5C to 4.2V cycling, CCCV 0.5C to 5V until swelling abusive Temperature: Chamber 45°C to accelerate aging	Piezoelectric transducer (PZT-5A) mounted with epoxy, instead glycerin
Popp et al. (2019)[30] *State estimation of Lithium-ion batteries by simplified ToF measurement*	Real application testing. Various temperatures and C-rates. Temp has significant effect on ToF so temp required for BMS. Changing C-Rate make SoC less reliable but can use algorithm to improve	Pulse frequency: 30kHz Wave path: Pitch/catch – across surface Cell type: 12Ah pouch cell Charge type/rate: CCCV / 0.1, 0.5 & 1C Temperature: 50% cycling 5-45°C	Commercial piezo-electric transducer discs, K-type thermocouple

Authors, *title/aim of work*	Conclusions/analysis	Test parameters	Sensor type
Oca et al. (2019)[52] *Electrical abuse tests assessment based on US characterisation*	US confirms irreversible physical modifications under abuse conditions	Pulse frequency: 120-500kHz Wave path: Through pulse Cell type: 0.5Ah pouch cell Charge type/rate: 10C to 7.6V (2x maximum)	Small ceramic piezoelectric transducers
Chang et al. (2019)[53] *Real-time measurement of li-ion batteries based on air-coupled US*	Feasible to estimate battery power using air coupled US detection	Pulse frequency: 400kHz air coupled Wave path: Through pulse Cell type: 36Ah Temperature: 25°C constant	Air coupled transducer
Li and Zhou (2019)[55] *Numerical solution, fluid-solid coupling based air-coupled US detection of stomata defect*	Stomata defect at different positions of li-ion battery correctly characterised in simulation and experiments	Pulse frequency: 400kHz Wave path: Through pulse air coupled Cell type: 6Ah Charge type/rate: Defect detection	
2020			
Chang et al. (2020)[35] *Adverse effects of temperature shifts on Li-ion batteries, acoustic study*	Acoustic signal effective parameter for determining when gassing occurs	Pulse frequency: 2.2MHz Wave path: Pitch/catch through Cell type: 0.21Ah LCO pouch cell Charge type/rate: CCCV / 0.1C Temperature: Transitioning between 5, 20 & 60°C	Transducer
Zappen et al. (2020)[36] *High temp abuse, impedance, spectroscopy and ultrasonic measurement*	Impedance and US show distinct changes in temp ranges, SEI dissolution, evaporation of solvents	Pulse frequency: 2.2MHz Wave path: Guided waves Cell type: 3.3Ah pouch cell Temperature: High temperature	Bonded sensor
Pham et al. (2020)[42] *Acoustic ToF spectroscopy and X-ray imaging*	Direct measurement and analysis of onset of gassing using US	Pulse frequency: 2.25MHz Wave path: Pulse/echo Cell type: 0.21Ah pouch cell Charge type/rate: CCCV	Commercial probe
Bommier et al. (2020)[43] *Acoustic detection of lithium metal plating*	US can detect lithium plating, degree determined by difference in ToF	Pulse frequency: 2.25MHz Wave path: Through pulse Cell type: 0.21Ah pouch cell Charge type/rate: CCCV, various C-rates Temperature: Controlled, various	Commercial probe
Robinson et al. (2020)[32] *Identifying defects in li-ion cells using US*	Deliberately built defects, defects in commercial sources detected using US, validated using X-rays	Pulse frequency: 10MHz - 1D linear phased array 1-5MHz Wave path: Various methods Cell type: Bespoke cells - 0.4Ah commercial cells Charge type/rate: Defect detection	Commercial probe
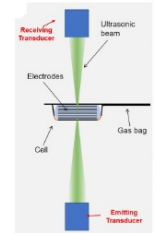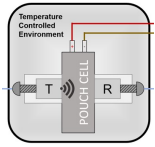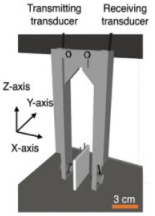
Authors, *title/aim of work*	Conclusions/analysis	Test parameters	Sensor type
Bauermann et al. (2020) [33] *Scanning acoustic microscopy (SAM) imaging tool to localise defects*	SAM promising tool to visualize defects. More appropriate for flat thin cells with thin casing like pouch cells	Pulse frequency: 15MHz, 100MHz Cell type: Commercial coin and pouch cells	
Bommier et al. (2020) [44] *Acoustic Monitoring of SEI Formation and Long-Term Cycling in NMC/SiGr Composite Pouch Cells*	Acoustic technique that can offer insights on SEI formation and capacity degradation of Si/graphite composites	Pulse frequency: 2.25MHz Cell type: 0.51Ah NMC/SiGr Composite pouch cell Wave path: Through pulse Charge type/rate: C/50, C/7, C/5 & C/2.5	Transducer
Chang et al. (2020) [45] *Measuring effective stiffness on li-ion batteries via acoustic signal processing*	Acoustic waveforms can be used to estimate stiffness of active storage material	Pulse frequency: 2.25MHz Wave path: Through pulse Cell type: 0.21Ah pouch cell	Commercial probe
Deng et al. (2020) [34] *Ultrasonic Scanning to Observe Wetting and "Unwetting" in Li-Ion Pouch Cells*	The ultrasonic imaging technique is a very sensitive method to probe failure mechanisms in Li-ion pouch cells	Pulse frequency: 2MHz Wave path: Through pulse Cell type: 0.24Ah pouch cell Charge type/rate: CCCV / 1C 3000 cycles	Focusing transducer
2021			
Hodson et al. (2021) [38] *A Initial Exploration of Coupled Transient Mechanical and Electrochemical Behaviors in Lithium Ion Batteries*	Gained insights into lithium-ion concentration accumulation and depletion at the electrode/electrolyte interface	Pulse frequency: 2.5MHz Wave path: Through pulse Cell type: Pouch cell Charge type/rate: C/2	Commercial probes
Chang and Steingart (2021) [46] *Operando 2D Acoustic Characterization of Lithium-Ion Battery Spatial Dynamics*	Enabled spatially resolved operando scanning to detect local variations in phase behavior for the entire cell area during charging	Pulse frequency: 2.25MHz Wave path: Oil filled through pulse Cell type: 0.4Ah pouch cell Charge type/rate: CCCV various C-rates	Commercial probes

Table 4: Summary of acoustic battery inspection literature review

3.3 Review Summary and Conclusions

Ultrasonic monitoring is a well-established method of obtaining feature rich data from a battery. Each battery, regardless of chemistry or design, undergoes redistribution of density as a function of charge along with bulk moduli changes in anode and cathode layers[19,30]. Many studies now exist that use ultrasound to exploit this, as well as the monitoring of battery ageing[40], gassing[44] and swelling[50]. A further advantage of this method is the simple application of a sensor at a low cost making it suitable for implementation into a BMS[30,56].

Much of current ultrasound/battery studies have focused on improving accuracy by using pulse techniques and instrumentation experiments[30,51,56,57]. Other studies have used ultrasound data combined with traditional SoC and state of health (SoH) estimation methods to reduce errors, as well as implementation in predictive models and machine learning algorithms[40,57].

A common approach in most studies is the selection of a single peak in the time domain waveform, be that of an individual wave[40,41,47,56] or from a signal envelope[51,57]. From the time of flight (ToF) and signal amplitude, measurements are recorded and compared with battery information such as SoC and SoH. In previous work there is little discussion of the characteristics of the wave response and what causes it to return to the capturing sensor in the manner it does. Much of the focus in Section 6 is on this analysis on signal responses and how different parts correlate differently with driving factors such as battery charge and cell temperature during standard test conditions.

Studies using non-standard testing conditions such as fault detection, electrical abuse and thermal abuse[32,36,52,55] attempt to utilise the non-invasive nature of ultrasound monitoring to provide real-time insights into potential cell issues with some success. The work contained in Section 7 implements the analysis methods developed in Section 5.2 to conduct non-standard, thermal abuse tests.

- There is a lack of discussion in literature regarding from which part of the signal measurements should be taken. Further to this, signal processing methods are rarely stated, with little evidence of methodologies in obtaining quantitative results from ultrasound A-scans.

- There is a lack of signal response analysis in the frequency domain. Measurements are almost exclusively taken from the time domain throughout the litera-

ture.

- No discussion about the nature of waves and reflections and what may may be causing the signal responses to take the form that they do. Often entire sections of signal are referred to as a reflection, which may be an oversimplification. On occasion a peak in a signal may be attributed to a specific layer in a cell, this may be an assumption that does not fully hold.

- Most studies use commercial probes. Some use bonded sensors. No evaluation of signal quality of either method takes place.

- Little discussion about the effect of temperature on the signal. Holding ambient temperature constant does not prevent potential for battery driven temperature changes. No evaluation of the extent charge/temperature affects the signal or if the two can be isolated for precise and accurate measurements of each.

- No hardware evaluation, changes in ultrasound could come from sensor/couplant.

4 1D Wave Model

To aid understanding of the complex nature of waves travelling through multi-layered bodies such as a lithium-ion battery, a 1D model is developed. This chapter describes the model that was created to simulate a wave or series of waves pulsed through multiple layers. Model outputs are specifically designed to provide insights into the features in wave responses gained during experimental testing and throughout existing literature.

4.1 Model Construction

A model was created to predict the transmission and reflection of a sound wave through a pouch cell represented as a 1D layered body. The passage of a 1D wave through a body is governed by the partial differential equation (PDE) wave equation:

$$u_{tt} = c^2 u_{xx} \tag{4.1}$$

Where u is the wave position at point x and at time t, c is the wave speed through the material at position x.

Note that the second derivative of a function can be estimated using the central difference:

$$f''(x) \approx \frac{f(x + \Delta x) - 2f(x) + f(x - \Delta x)}{\Delta x^2} \tag{4.2}$$

Using this technique to give estimations for the second derivatives in the wave equation:

$$\frac{u(x, t + \Delta t) - 2u(x, t) + u(x, t + \Delta t)}{\Delta t^2} = c^2 \frac{u(x + \Delta x, t) - 2u(x, t) + u(x + \Delta x, t)}{\Delta x^2} \tag{4.3}$$

Building this into a MATLAB model to numerically approximate the travelling wave using the following finite difference scheme where i is each point of the wave in space and j is each point of the wave in time

$$\frac{u_{i,j-1} - 2u_{i,j} + u_{i,j+1}}{\Delta t^2} = c^2 \frac{u_{i-1,j} - 2u_{i,j} + u_{i+1,j}}{\Delta x^2} \tag{4.4}$$

With starting conditions initialising sine waves, the model has information to make forward estimations in time based on the wave development by rearranging 4.4 to make the next point in time $(u(i, j + 1))$ the subject of the calculation as follows

$$u_{i,j+1} = \frac{\Delta t^2 c^2}{\Delta x^2}(u_{i-1,j} - 2u_{i,j} + u_{i+1,j}) + 2u_{i,j} - u_{i,j-1} \tag{4.5}$$

In which each of the points below enables the forward estimation

- Previous position $(u_{i-1,j})$

- Current time and position $(2u_{i,j})$

- Next position $(u_{i+1,j})$

- Previous time $(u_{i,j-1})$

Equation 4.5 is built into a Matlab script with c being a field of values created to simulate the changes in material properties across the cell. To obtain instantaneous visualisations of the effects of changes the c values using the same numerical solution to the wave equation, an excel sheet was created as shown in Figure 4.1.

Changing the c value (speed) for the cells in the third row from positions 7 to 11 causes a material interface to appear, this in turn shows reflections occurring at this boundary with the remaining energy transmitted through. Changes in the c field changes the wave response accordingly in the sheet and is visualised using the conditional formatting.

Differences in the wave speed c field will result in the transmission/reflection effect shown in Figure 2.3. The reflection coefficient is the proportion of a wave amplitude reflected at a boundary and is given by:

$$R = \frac{Z_2 - Z_1}{Z_2 + Z_1} \tag{4.6}$$

Where Z_n is the acoustic impedance of the material $Z_n = (\rho_n c_n)$, ρ being the material density and c being the sound velocity for the material. The reflection coefficient R varies between 0 and 1 and the transmission coefficient is R-1.

	dt= 0.04					K= 100		S= 0			
	dx= 0.03										

speed		0.5	0.5	0.5	0.5	0.5	0.5	0.15	0.15	0.15	0.15	0.15	
pos		1	2	3	4	5	6	7	8	9	10	11	
time		0	0.03	0.06	0.09	0.12	0.15	0.18	0.21	0.24	0.27	0.3	
0	0	0	0	0	0	0	0	0	0	0	0	0	U0
1	0.04	0	0.22	0.33	0.32	0.23	0.13	0.02	0.01	0.00	0.00	0.00	U1
2	0.08	0	0.39	0.61	0.61	0.45	0.25	0.04	0.01	0.00	0.00	0.00	U(j,i)
3	0.12	0	0.49	0.79	0.83	0.65	0.37	0.07	0.02	0.01	0.00	0.00	
4	0.16	0	0.50	0.85	0.95	0.81	0.48	0.10	0.03	0.01	0.00	0.00	
5	0.2	0	0.45	0.80	0.97	0.88	0.57	0.16	0.04	0.01	0.00	0.00	
6	0.24	0	0.35	0.67	0.87	0.85	0.61	0.22	0.05	0.02	0.00	0.00	
7	0.28	0	0.24	0.48	0.67	0.73	0.59	0.29	0.07	0.02	0.01	0.00	
8	0.32	0	0.13	0.28	0.42	0.52	0.49	0.36	0.10	0.03	0.01	0.00	
9	0.36	0	0.03	0.07	0.14	0.25	0.35	0.43	0.13	0.03	0.01	0.00	
10	0.4	0	-0.07	-0.12	-0.12	-0.02	0.20	0.49	0.17	0.05	0.01	0.00	
11	0.44	0	-0.16	-0.29	-0.34	-0.23	0.08	0.52	0.22	0.06	0.02	0.00	
12	0.48	0	-0.24	-0.42	-0.49	-0.36	0.01	0.52	0.28	0.08	0.02	0.00	
13	0.52	0	-0.29	-0.50	-0.55	-0.37	0.01	0.49	0.33	0.11	0.03	0.00	
14	0.56	0	-0.31	-0.51	-0.51	-0.30	0.04	0.43	0.39	0.14	0.04	0.00	
15	0.6	0	-0.28	-0.43	-0.38	-0.17	0.10	0.36	0.43	0.17	0.05	0.00	
16	0.64	0	-0.19	-0.26	-0.17	-0.01	0.16	0.28	0.46	0.22	0.06	0.00	
17	0.68	0	-0.05	-0.02	0.07	0.15	0.19	0.21	0.48	0.26	0.08	0.00	
18	0.72	0	0.13	0.24	0.31	0.29	0.22	0.14	0.48	0.31	0.10	0.00	
19	0.76	0	0.30	0.48	0.51	0.41	0.24	0.09	0.45	0.36	0.13	0.00	
20	0.8	0	0.42	0.65	0.66	0.49	0.27	0.06	0.41	0.40	0.16	0.00	
21	0.84	0	0.46	0.72	0.73	0.55	0.30	0.05	0.35	0.43	0.19	0.00	
22	0.88	0	0.41	0.67	0.72	0.58	0.34	0.07	0.28	0.45	0.23	0.00	
23	0.92	0	0.30	0.53	0.63	0.56	0.36	0.10	0.22	0.45	0.26	0.00	
24	0.96	0	0.16	0.32	0.46	0.48	0.35	0.15	0.15	0.44	0.29	0.00	
25	1	0	0.02	0.11	0.24	0.34	0.32	0.21	0.10	0.41	0.32	0.00	
26	1.04	0	-0.09	-0.09	0.01	0.14	0.24	0.26	0.06	0.36	0.34	0.00	
27	1.08	0	-0.15	-0.24	-0.21	-0.07	0.13	0.31	0.05	0.30	0.34	0.00	
28	1.12	0	-0.19	-0.34	-0.38	-0.26	0.01	0.34	0.05	0.23	0.33	0.00	
29	1.16	0	-0.21	-0.40	-0.48	-0.38	-0.08	0.35	0.08	0.16	0.30	0.00	
30	1.2	0	-0.22	-0.40	-0.49	-0.41	-0.11	0.33	0.11	0.09	0.26	0.00	
31	1.24	0	-0.21	-0.37	-0.43	-0.34	-0.08	0.28	0.15	0.03	0.19	0.00	
32	1.28	0	-0.18	-0.29	-0.30	-0.21	-0.01	0.21	0.21	-0.02	0.12	0.00	
33	1.32	0	-0.12	-0.17	-0.13	-0.02	0.08	0.13	0.24	-0.05	0.03	0.00	
34	1.36	0	-0.03	-0.01	0.08	0.16	0.14	0.06	0.25	-0.07	-0.06	0.00	
35	1.4	0	0.08	0.18	0.28	0.30	0.18	0.00	0.25	-0.08	-0.15	0.00	
36	1.44	0	0.20	0.37	0.45	0.38	0.19	-0.05	0.24	-0.08	-0.23	0.00	
37	1.48	0	0.31	0.52	0.55	0.40	0.17	-0.07	0.19	-0.07	-0.30	0.00	
38	1.52	0	0.37	0.58	0.57	0.39	0.15	-0.08	0.12	-0.05	-0.34	0.00	
39	1.56	0	0.36	0.55	0.52	0.36	0.14	-0.06	0.03	-0.05	-0.36	0.00	
40	1.6	0	0.28	0.42	0.41	0.30	0.13	-0.04	-0.06	-0.05	-0.35	0.00	
41	1.64	0	0.13	0.22	0.25	0.21	0.12	-0.01	-0.15	-0.06	-0.32	0.00	
42	1.68	0	-0.03	0.00	0.06	0.11	0.10	0.02	-0.23	-0.09	-0.26	0.00	
43	1.72	0	-0.17	-0.21	-0.14	-0.02	0.04	0.05	-0.30	-0.13	-0.19	0.00	
44	1.76	0	-0.25	-0.37	-0.32	-0.17	-0.04	0.05	-0.34	-0.18	-0.10	0.00	
45	1.8	0	-0.27	-0.45	-0.46	-0.33	-0.14	0.04	-0.37	-0.23	-0.02	0.00	
46	1.84	0	-0.25	-0.46	-0.54	-0.46	-0.24	0.01	-0.37	-0.28	0.06	0.00	
47	1.88	0	-0.21	-0.41	-0.55	-0.53	-0.33	-0.05	-0.35	-0.32	0.12	0.00	
48	1.92	0	-0.16	-0.33	-0.48	-0.51	-0.38	-0.13	-0.32	-0.34	0.16	0.00	
49	1.96	0	-0.12	-0.25	-0.37	-0.43	-0.38	-0.23	-0.28	-0.34	0.17	0.00	
50	2	0	-0.08	-0.16	-0.23	-0.29	-0.34	-0.34	-0.25	-0.32	0.15	0.00	

Figure 4.1: Wave equation applied in excel, using conditional formatting green cells show high amplitude and red cells show low amplitude. The thick black vertical line of the sheet shows a material boundary.

The boundaries are fixed and rather than c being a single constant wave speed value, it is built as an array with variable values to simulate differences in wave speed across the length of the body, modelling the properties of various material layers. As the wave encounters a different c value, some energy from the passing wave is transmitted and the rest is reflected, like that of the reflection coefficient R. The wave speed c is obtained using:

$$c = \sqrt{\frac{E}{\rho}} \tag{4.7}$$

Where E is the elastic modulus. A summary of the finite difference scheme is shown

in Figure 4.2. By recording values adjacent to the model boundaries, simulated waveforms, such as those gained using contact transducers, are captured. The side with the initial pulse being a pulse/echo simulation and the opposing side simulating a pitch/-catch through pulse.
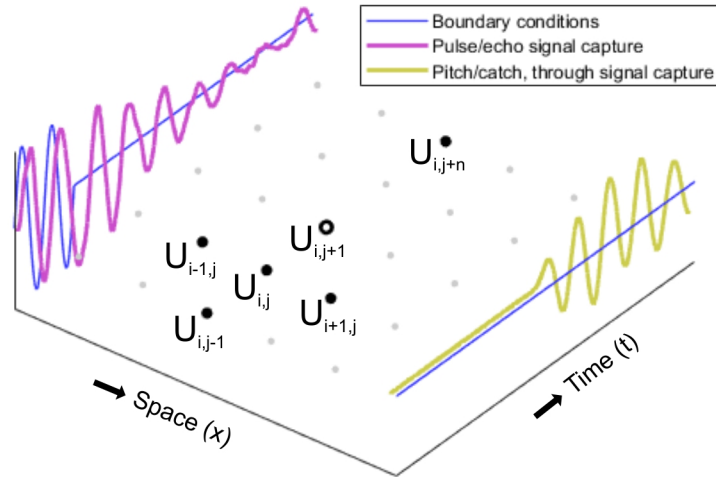
Figure 4.2: Finite difference scheme showing points in time/space used to calculate point $u_{i,j+1}$. Boundary conditions of left side include the initial pulse (blue). Position used to capture pulse/echo signal shown in magenta, pitch/catch through wave shown in yellow.

4.2   Input Parameters

To model the ultrasonic wave passing through a simulated battery a matrix was created to represent the cell body in time and space. The length of time was specified (typically 20μs in steps of dt = 2.7ns giving 7500 data points) and the cell body width (typically 5mm in steps of dx = 20μm giving 250 data points). A base wave speed was set at v = 3000m/s to ensure the Courant–Friedrichs–Lewy (CFL) condition is met for model stability, where $CFL \leq 0.5$ from equation:

$$CFL = v\frac{dt}{dx} \tag{4.8}$$

The initial pulse was initialised in the time domain starting at $t = 0$, being n number

47

of consecutive sine waves (typically $n = 3$). The wavelength was determined by setting a single sine wave to 1µs representing 1MHz, stacking and scaling these according to the user requested cycle numbers and pulse frequency. The finite difference model calculated the wave position at each point across the cell body after which the time step was increased and the next iteration of the wave was calculated. The c array represents the wave speed across the battery, this varies simulating the various material properties of layers within the cell. Each block of identical wave speeds across the array represent the dimensions of each layer. As the wave encounters these changes in c the wave equation underpinning the model transmits and reflects proportions of the passing wave according the nature of the change in wave speed.
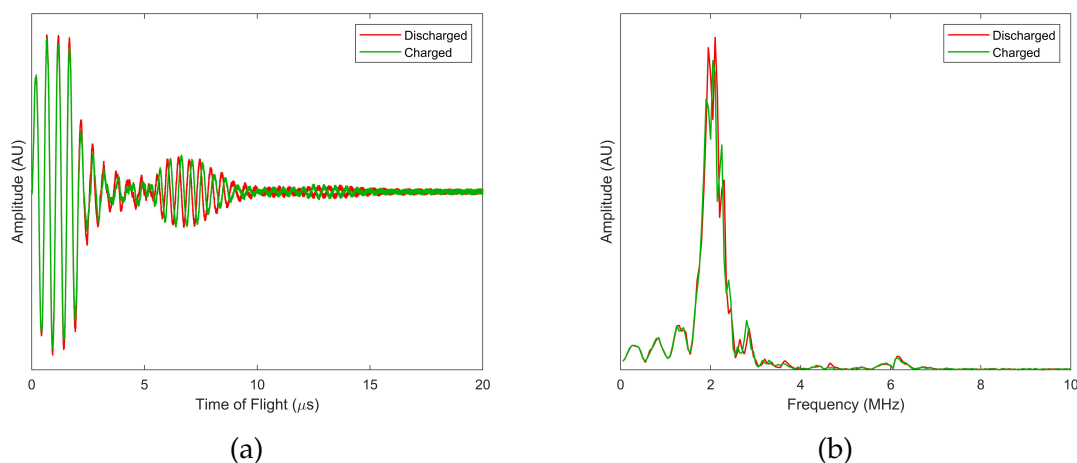
Figure 4.3: a) A-scan waveform generated by pulsing through the layers a simulated battery cell (red wave is discharged, green is charged state). b) Fourier transform for the simulation showing the main wave activity focused around the 2MHz region

The wave speeds for the various components were generally taken from the density and elasticity values provided by Hsieh et al.[19], calculated using equation 4.7 the layer dimensions were based on those provided by Ladpli et al.[57]. Two separate matrices were generated where certain layers in the body alter in the time domain T to represent either stepped/partial or complete charge and discharge of the battery. This charge simulation used the range of density values for $LiCo0_2$ (cathode) and graphite (anode) and alters them linearly in multiple steps or a single step. The anode layer(s) decrease wave speed during charge whilst the cathode layer(s) increase wave speed. These localised layer density changes alter the nature of the wave reflections and provide differing wave responses, a simulated signal response, known as an A-scan, and Fourier transform are shown in Figure 4.3.

4.3 Sample Outputs

Figure 4.4 shows some sample output from the model at four time steps. The top half of each plot shows a different density distribution to the bottom half (although the overall density value remains unaltered) which can be thought of as charged/discharged states of a battery.

(a)	(b)	(c)	(d)
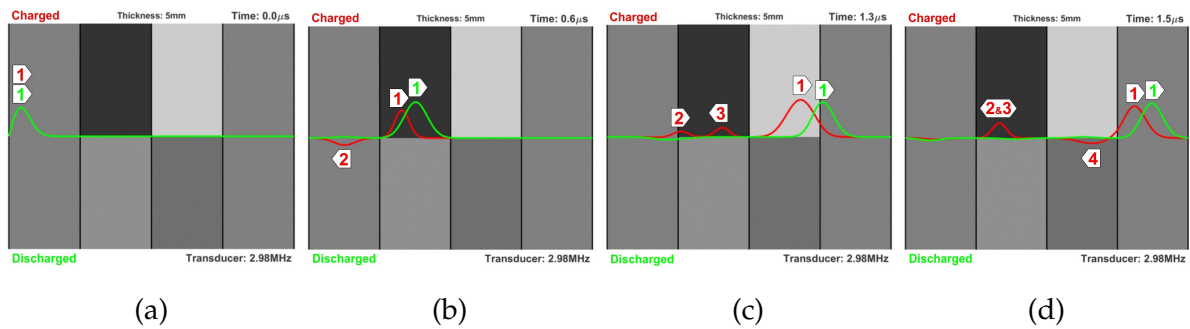
Figure 4.4: Simple four layered body wave model with differing density distribution. Notice due to the relatively even distribution of the theoretically discharged (bottom) half of the model, where the wave passes through layers with almost all the wave transmitted and very little reflection. These reflection/transmission events occur as every wave (including new waves) reaches each interface, in either direction. This causes the signal to quickly develop in complexity meaning direct measurements are difficult to take or unreliable.

For illustrative purposes, this simple case simulates four layers in a 5mm body thickness with an ultrasound sensor pulsing a single wave at a frequency of 3MHz. The timing of each capture is shown in the top right corner.

a) The model starts at 0.0μs and the two waves are overlaid with only the green, discharged state, wave visible.

b) By 0.6μs, the red wave (charged state) is only partially transmitted and some part of the wave is reflected back towards the source, in addition the red wave slows down somewhat and lags behind the green wave. This occurs as the red wave encounters a significant change in material property as this transmission/reflection effect occurs in such instances.

c) By 1.3μs the red wave has passed through a second material property change and produced a third wave of note, reflected back towards the source, the second wave has reflected from the boundary and is now following behind the initial pulse.

d) At 1.5µs both waves marked 2 & 3 pass through each other and form a constructed wave larger than each of the individual waves travelling through the body as they are of the same phase, by this time the incident wave has passed through a third layer interface and a new wave, wave 4 is reflected back towards the source. Notice the initial phase of waves 2 and 4 contrasted with wave 3, this is a result of change of material property values, 2 and 4 moved to a higher density material whilst wave 3 created as reflection traveling into a lower density material.
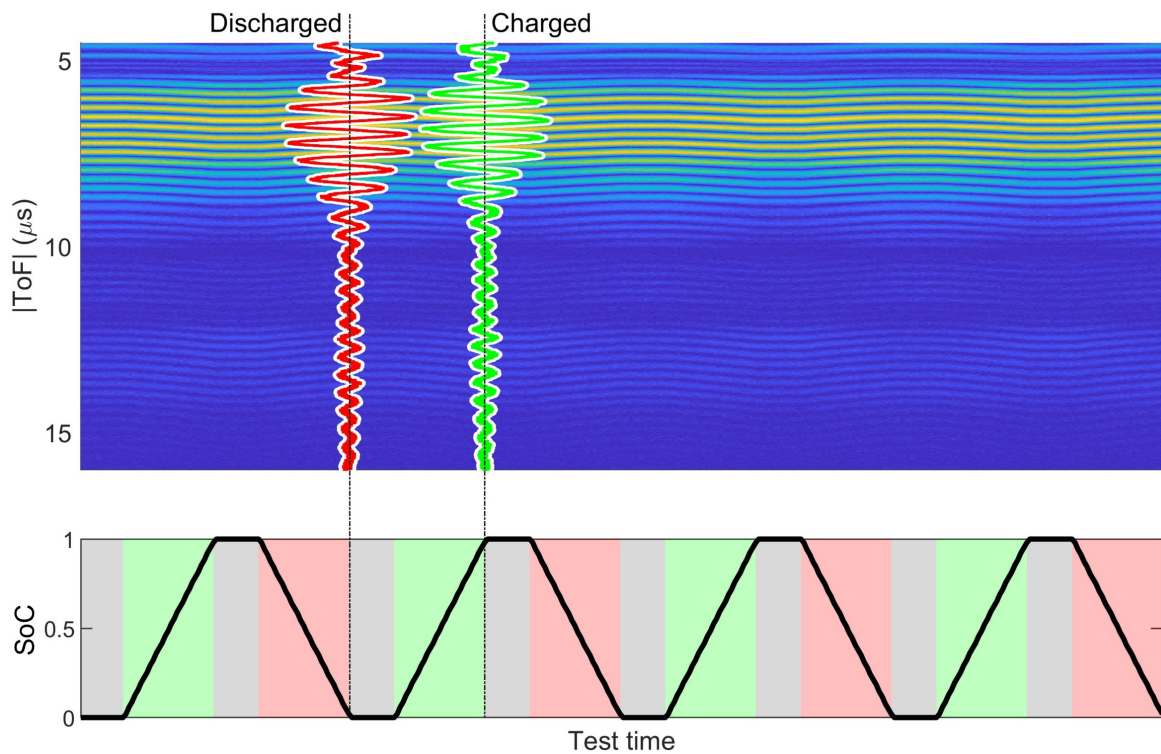
Figure 4.5: Predicted ultrasonic amplitude intensity map as a battery is charged and discharged. Each waveform (A-scan) is stacked (two sample signals shown, discharged state in red and charged state in green) to form a surface plot, where the high (yellow) intensity regions represent the larger amplitude signal peaks. The absolute values are shown in this plot for clearer viewing. In b) The battery SoC is plotted over a colour coded background to identify the part of the charge cycle (green = charge, red = discharge, grey = rest). The black dashed vertical lines show the position of the two sample waveforms.

A typical pouch cell geometry configuration based on values in Table 5, with density and therefore wave speed values changing according to a battery charging profile, produces a series of simulated ultrasound wave responses that can be stacked to form the amplitude intensity plot shown in Figure 4.5.

Table 5: Elastic modulus and density values of electrodes and separator for ultrasonic wave response simulation

Component	Charge (%)	Elastic Modulus (GPa)	Density (kg/m3)	Wave Speed (m/s)	Thickness (µm)	Citation
Anode (Graphite)	0	30	2078	3800	96	
	20		2213	3700		
	40	30	2348	3600	96	
	60		2484	3500		
	80		2619	3400		
Anode	100	30	2754	3300	96	
Separator		0.7	550	1128	25	
Cathode (LiCoO$_2$)	0	184	5663	5700	60	
	20		5488	5800		
	40	184	5312	5900	60	
	60		5137	6000		
	80		4961	6100		
Cathode	100	184	4786	6200	60	

Electrode material wave speeds increase/decrease as a function of the battery charging as lithium passes back and forth between anode and cathode during cycling. For the model, a constant current charge/discharge is considered, as such the density values move to their end values in a linear, incremental fashion. For more accurate modelling, changes in the elastic modulus should be included in calculations, however as with the model utilised by Hsieh et al.[19], the modulus is held constant and is considered sufficient for these estimation purposes.

The changes in density distribution cause ultrasonic wave response changes, stacking A-scans to form a signal intensity surface plot and synchronising with battery shows a clear relationship between charge layers [cathode-separator-anode-separator] can be specified. The thicknesses of all layers and number of active layers can also be specified and the frequency and number of the initial pulses (2MHz and 2 cycles in this example).

Figure 4.6a illustrates the same model as that in Figure 4.5 with the grey scale representing the density/wave speed and relative thickness of each layer (top) and two A-scan responses (charged in green, discharged in red) overlaid (bottom). A box is drawn to show the region of the signal containing the 'first reflections'. Figure 4.6b is the same model except for an arbitrary change in the separator material density (550kg/m^3 to 1450kg/m^3) which, once again holding the elastic modulus constant for this estimation, results in a change in separator wave speed of 1128m/s to 685m/s, all other parameters remain unaltered. Inspection of the bottom panel shows the change
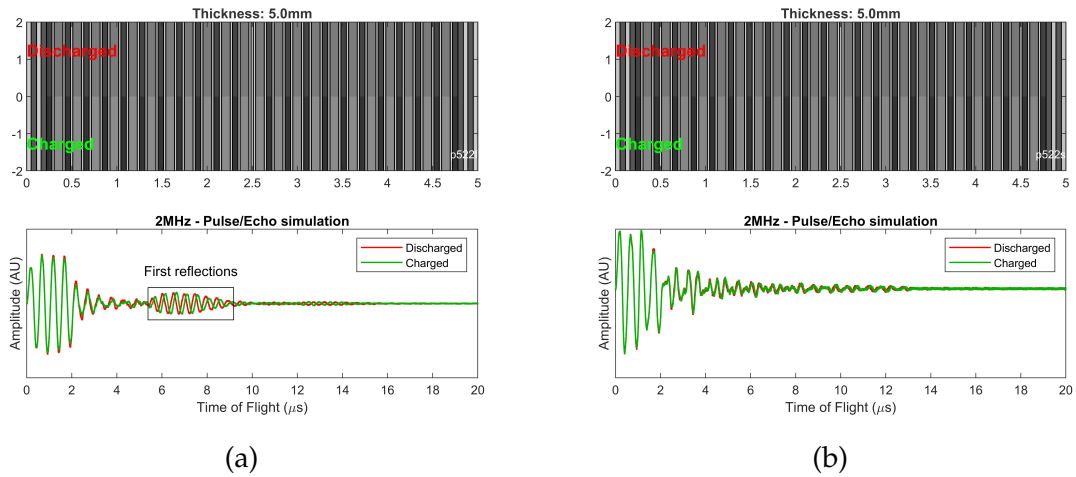
Figure 4.6: Model based on values taken from Table 5, separator wave speed for a) is 1128m/s and is altered to 685m/s in figure b) all other material properties and all dimensions remain the same for both models. This change creates a very different signal response as shown in the wave form.

of separator property has a significant effect on the wave response. Two things are immediately clear resulting from this change, firstly, the change between charged and discharged states is greatly diminished in the right-hand model and secondly, the clear wave response has collapsed, there is no obvious region containing the first reflections and does not lend itself to taking an envelope from which to take readings. Model animations of Figures 4.6a & b are included in the supplementary material (Figures S.1 & S.2 respectively), showing the propagation of the incident waves through the multiple layers of the cells with A-scan generation displayed in 'real-time'.

4.4   Model Consistency

In order to check the consistency of the model, a simple layered body is created using values designed to provide clear reflections from which measurements can be taken to match with expected values. In this example a three layered bearing pad is simulated using the wave speed appropriate for the materials used. The top plot in Figure 4.7a shows the arrangement of the three layers with a 35mm steel layer, 5mm interlayer and 2mm PTFE layer. The graphic is in two halves with the default layer on top and the slow interlayer on the bottom. The steel and PTFE are the same for both models all according to Table 6.

The ultrasound pulse/echo responses are displayed in the center panel in Figure 4.7a.

Table 6: Three layered bearing pad values for model time of flight consistency purposes.

Material	Speed of sound (m/s)	Thickness (mm)	Travel time within material, single path (us)	Time of flight, pulse/echo (us)	
				Default	Slow
Steel	5900	35	5.93	11.86	11.86
Interlayer	4700	5	1.06	13.98	
Interlayer (slow)	4000	5	1.25		14.36
PTFE	1350	2	1.48	16.94	17.32

This shows a discrepancy between the model using the default interlayer material (green) and the slow material (red), the red reflections lagging behind the green. The bottom panel of Figure 4.7a shows a the Fourier transform to confirm that the signal is showing a response centered around 5MHz, which was the chosen pulse frequency.

The successful check for consistency is shown in Figure 4.7b where the calculated time of flight values from Table 6 are marked in the default and slow model. The reflections back from the steel/interlayer, interlayer/PTFE and PTFE/opposing face are all timed exactly where they should be according the calculations. The slower interface material shows the signal responses lagging, apart from the first reflection as this would not have encountered any material differences.

The waveform development plot shown in Figure 4.7c provides insights into the nature of the reflections. The yellow line shows the path taken by the waves that show up as a small collection of peaks in Figure 4.7b, each are highlighted in a circle. This wave development plot can help provide context to parts of signal that otherwise would be subject to assumptions, it is convenient to think of parts of the signal as reflections from definite parts of the layered body, however this insight shows that even with a simple three layered structure, the signal contains difficult to interpret characteristics.

This model consistency check was been conducted using this simplified example as this model does not incorporate some important features that would likely be factors in a complex system such as a battery cell. For example, the material elasticity, acoustic impedance and near-field effects[58]. Additionally, it would be difficult to exactly recreate the specific layer parameters of the cell that would enable direct comparisons. This validation does confirm that the model produces the correct number of reflections with each having appropriate timings, giving confidence the model is producing sensible results, if not totally correct.

This brief study does not provide any experimental validation for the model, it dis-
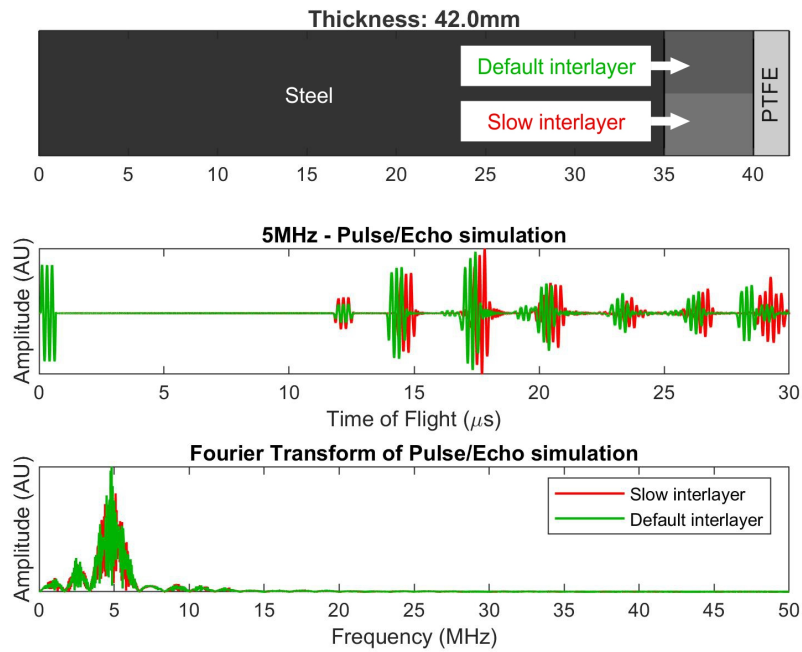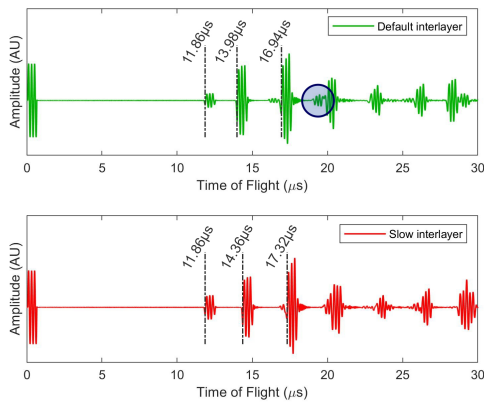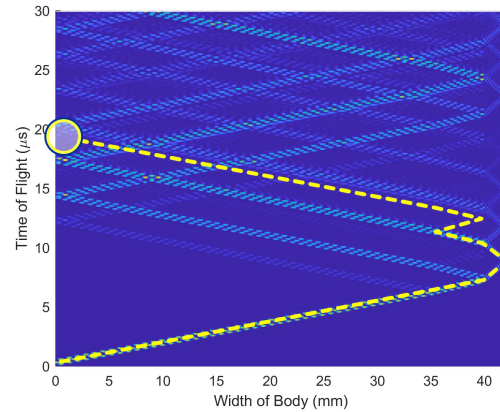
Figure 4.7: Model consistency check based on values taken from Table 6, a) contains the model generated graphical illustration of the three layered bearing pad (top), the pulse/echo single sensor waveform response (center) and the signal response in the frequency domain (bottom). b) shows the waveforms for each of the two models with the expected timings marked up based on the layer thicknesses and speed of sounds. c) is the waveform development plot providing insights into signal responses with routes traceable to the characteristics at the sensing edge.

plays the timing of waves and the reflections from boundaries agree with the calculated values precisely. Questions remain about the phase and amplitude of reflected and transmitted waves, it is assumed that the timings and subsequent constructive

and deconstructive interference of multiple waves can be trusted. In future development it would be worth while obtaining wave responses for a simple system such as this bearing pad experimentally for direct comparisons with the modelling to asses the accuracy of all features in the signal such as amplitude and signal attenuation.

4.5 Parametric Study

The panel of plots in Figure 4.8 show the historical wave development of the battery modelled in Figure 4.6a as it passes through the cell layers. This clearly shows a set of first reflections (highlighted in the white box) back to the sensor side of the battery cell (width = 0mm) which occurs between approximately 5μs and 8μs. This region corresponds with the collection of peaks in the bottom panel of Figure 4.6a.

(a)

(b)
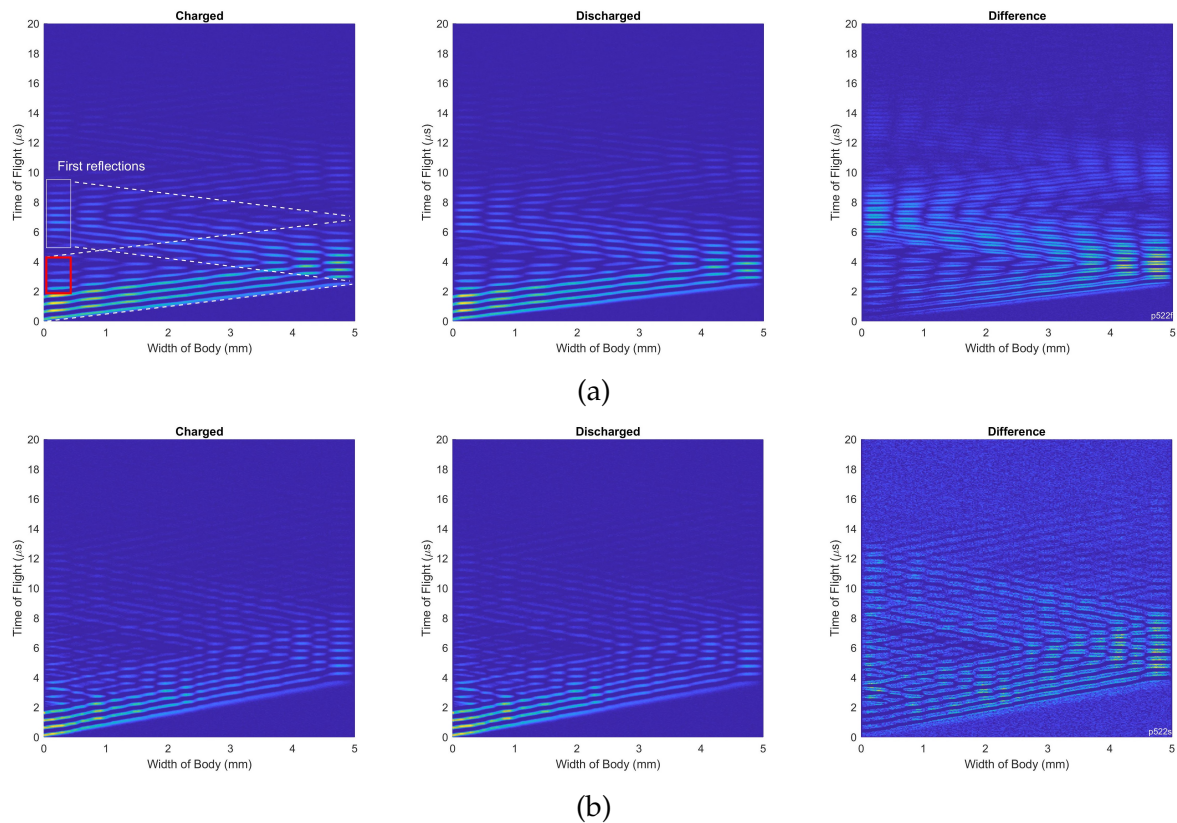
Figure 4.8: Waveform development, showing only wave peaks. For a) and b) Left-hand side is wave development for the charged state, centre panel shows the wave development for the discharged state and the right-hand side shows the absolute difference between the two charge extremes.

Observation of the difference panel (Figure 4.8a top right) confirms that these differ-

ences are driven by the incident waves (together with localised reflections and accumulated transmissions highlighted in the red box) reaching the opposing side of the body and returning the sensing edge of the cell. It can be assumed that waves of this nature collect and return information gathered through each layer of the cell twice (there and back) and would naturally be the most accurate to read.

Using the model in this way demonstrates the complex interactions of transmissions and reflections that sum to form a particular waveform response. The change in separator properties cause the convenient first reflection group to break down (as shown in Figure 4.8b). Essentially the lower separator speed of sound causes a greater acoustic mismatch between separator and electrode and hence greater reflection at each interface (as shown in equation 4.6). The most intense regions in the differences plot are close to the first active layer encountered after the casing.

This results in the signal struggling to penetrate the body causing a loss in battery measuring capability. In certain geometries, the signal can be dominated by reflections from large changes in material properties close to the sensor (casing materials/thickness) that will necessarily dominate the signal response. Locating a current collector can also have an effect as explored by Maier et al. [56], without knowing the precise construction of the cell it is difficult to ensure the signal response is optimised in terms of ultrasound correlation with SoC.

It would therefore be beneficial to have a method to identify the best waveform location to correlate with battery state of charge. To this end, experimental tests have been carried out with detailed analysis of the signal during different charge stages to explore methods of combating weak or unintuitive signal responses.

During experiments, a pulse frequency of 1–2 MHz was used, similar to the 2.25MHz used by Hsieh et al. [19], this gave the clearest response and best battery charge correlations during testing. Using lower frequencies provided diminished changes in wave response, whereas higher frequencies produced more unpredictable signals with lower battery charge correlations. The effects of frequency choice can be visualised and the problems explained using model data.

Three frequency choices were 0.5MHz, 2MHz and 5MHz, all other parameters are held constant. The plots in Figure 4.9 show the absolute differences between the wave developments for both fully charged and discharged states. The higher amplitude, yellow regions are where there are highest discrepancies whilst dark blue shows low/no discrepancy. The development of the 5MHz wave collects some differences (Figure 4.9a),

(a) 5MHz pulse

(b) 0.5MHz pulse

(c) 2MHz pulse

(d)
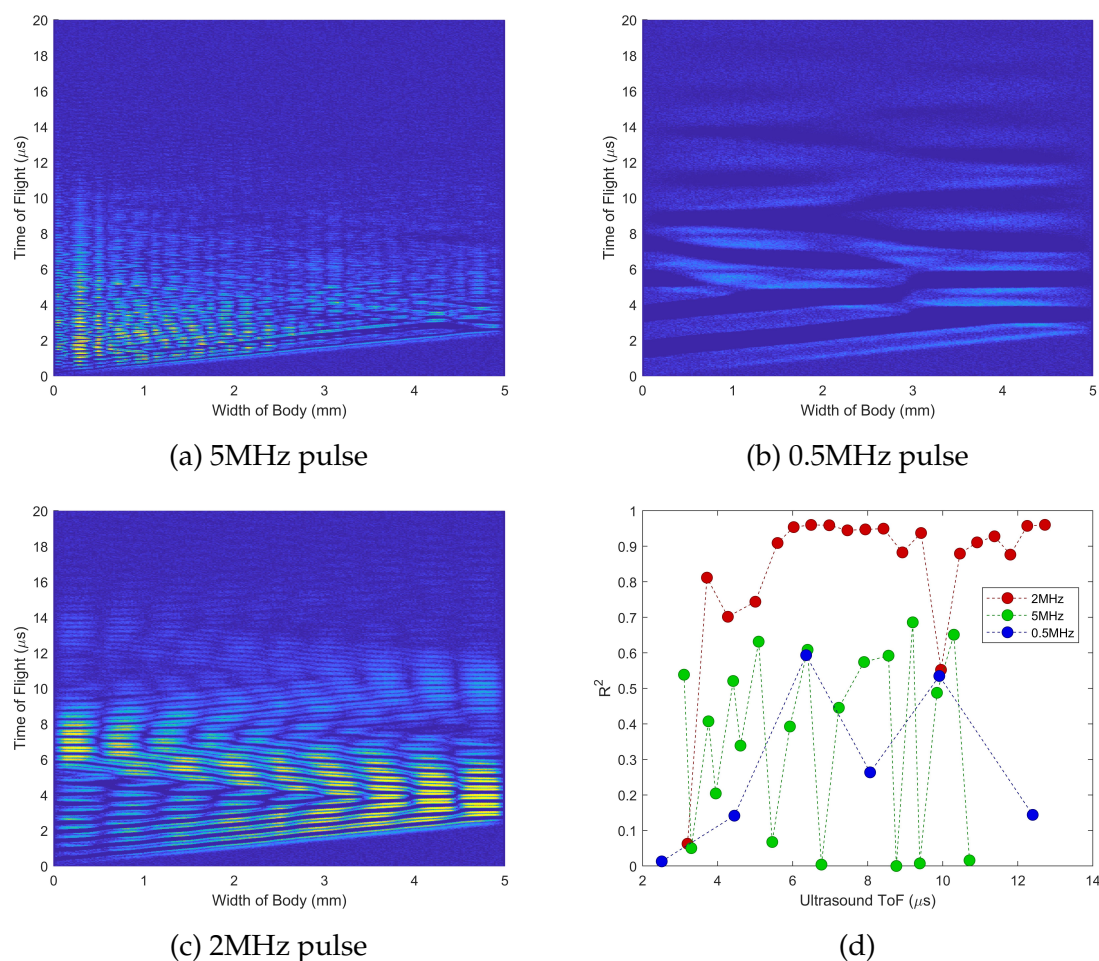
Figure 4.9: Charged/Discharged difference in ultrasound response plots. a) 5MHz shows small changes in wave development occurring close to initial pulses with lack of meaningful cell penetration. b) 0.5MHz wave passes through body almost unaffected by the changing properties in narrow layers. c) 2 MHz passes through the cell with the incident waves gathering and accumulating changes, travelling back to the recording sensor side. d) Ultrasound ToF/battery charge correlation show 2MHz has strong relationship with battery SoC.

these are accumulated close to the initial pulse side of the cell, the differences fail to accumulate due to lack of cell penetration of the wave. As a result, the signal is dominated by layers close to the pulse/echo edge and are susceptible to temperature bias as this would include a high proportion of cell casing reflections. The 0.5MHz waves (Figure 4.9b) only detect minor changes as the wavelengths are considerably larger than the narrow layers they pass through, note a lack of wave development with yellow, high intensity changes. The 2MHz wave (Figure 4.9c) shows significant differences collect along the wave paths as they return to the sensing edge with a clear region of first reflections. This illustrates that 2MHz offers a good balance between cell penetra-

tion (lower frequency) and detail from layer reflections (higher frequency), providing solid theory behind the sensor/pulse selection process. Figure 4.9d shows the effect on the SoC correlations of the three frequency choices, the 2MHz performs well whilst the 0.5MHz and 5MHz register very weak/no useful battery charge correlation and are unsuitable in this instance. Animations are included in the supplementary materials (Figure S.3: 5MHz, Figure S.4: 0.5MHz and Figure S.5: 2MHz) showing wave propagation, A-scan generation for charged and discharged states and a plot showing the difference in signal between the two.

4.6   Modelling Temperature Effects on Signal

The speed of sound is temperature dependent. In the model, temperature effects are simulated by altering the wave speeds at a global rather than local level. The whole wave speed array c is raised and lowered uniformly according to a specified temperature profile, based on the assumption that temperature change would affect the cell body as a whole and uniformly. This provides an opportunity to observe change in ultrasound responses combining cell level changes (temperature) with localised battery layer changes (elasticity/density).
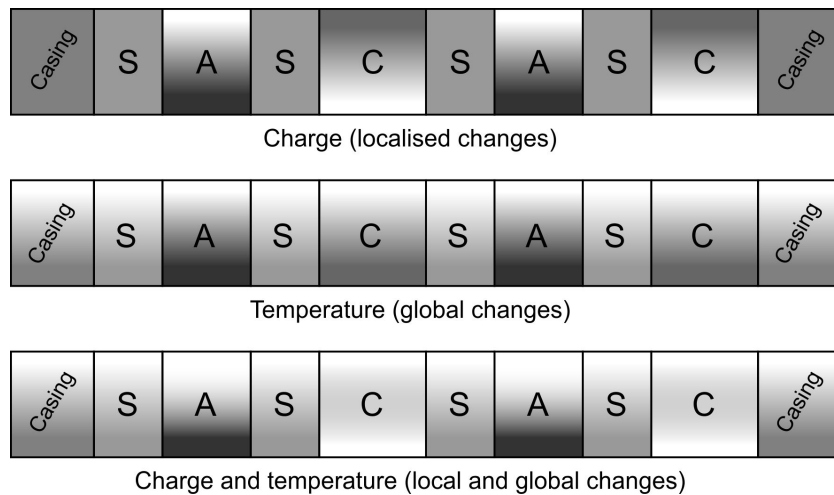
Figure 4.10: Changing wave speed profiles with respect to charge and/or temperature.

Figure 4.10 shows layer wave speed represented as greyscale bars, including; casing, anode (A), separator (S) and cathode (C). During charging (top bar) the electrodes change shade, in opposing directions. Where temperature is the only change (middle bar) all layers change shade, uniformly in the same direction. When both charge and

58

temperature are factors, the shading of each is overlaid. For the anode this accentuates the change whilst in the cathode the change is somewhat negated.

A cropped section of four modelled A-scans is shown in Figure 4.11. A wave response for a discharged cell undergoing no change in temperature is plot in red, acting as a benchmark. The response from the same cell when fully charged, with no change in temperature (the top bar in Figure 4.10) is shown in green, this could represent a cell charging using a low C-rate. The blue signal is the same cell fully discharged but the whole cell has increased in temperature (middle bar in Figure 4.10) +10°C in this instance, this could be simulating a resting cell subjected to ambient temperature changes. Finally, the magenta response is the signal where the cell is both fully charged and the +10°C increase in temperature are modelled (bottom bar in Figure 4.10). This could represent a cell charge cycling at a moderate C-rate whilst also subjected to the ambient temperatures.
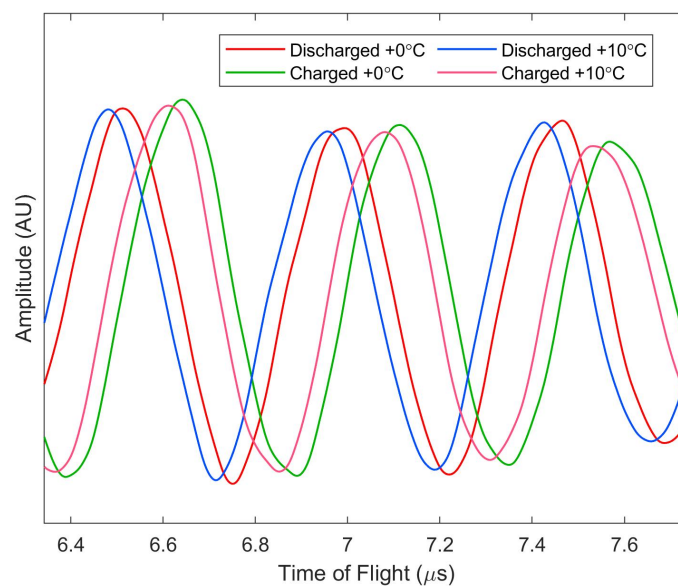
Figure 4.11: Modelled ultrasound wave response with respect to charge and/or temperature.

This modelling shown that as the temperature of a cell changes, due to ambient temperature fluctuation or internal cell reactions, the wave response is affected. A method of measuring this temperature effect is discussed in section 6.3. A possible calibration technique is suggested in section 6.7, aiming to reduce the impact of temperature changes on the ultrasound wave response.

4.7 Ultra High Frequency Ultrasound (UHFUS) Modelling

The frequencies of waves used in the ultrasonic monitoring of battery cells in current research has ranged from 30kHz[30] (just above the threshold of the definition of ultrasound) up to 15-100MHz[33]. The recent development of ultra high frequency ultrasound (UHFUS) enables transducers up to 70MHz[59]. The waves at such high frequency would have drastically shorter wavelengths, and as such would be capable of passing through layers in their entirety returning complete reflections back to the sensor. This modelling study shows how this increase in sensitivity to battery structure, has the potential to provide different insights to those currently obtained. This method would provide battery layer information from signal changes in the frequency domain, opposed to measurements commonly taken from the time domain.

When waves travel through a body and encounter waves travelling in the opposite direction, constructive and deconstructive interference with the signal will occur. When pulsing reflected waves in a layer with a multiple of one quarter wavelength of the signal, a standing wave arises. The travelling waves appear to stand still with nodes fixed at zero and antinodes at the signal peaks. The model will only resonate with half wavelengths as the boundary conditions are set to zero. Examples of resonant standing waves are shown in Figure 4.12. The plots simulate a) 0.75MHz, b) 1.5MHz and c) 2.25MHz waves through a single layered body of width 2mm and wave speed of 3000m/s. A modelling animation of the 3/2 wave is included in the supplementary materials, Figure S.6.

(a) 1/2 wave	(b) 1 wave	(c) 3/2 waves
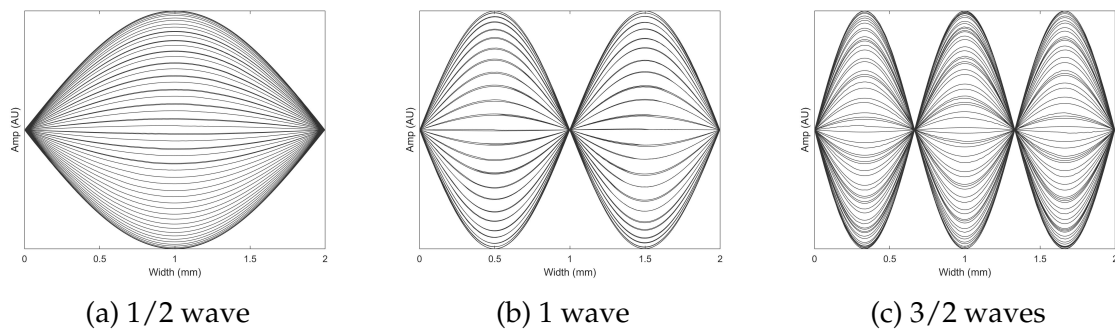
Figure 4.12: Examples of resonant standing waves through a 2mm body of wave speed 3000m/s.

Finding the resonant frequency of a layer is desirable as the amplitude is increased resulting from the constructive interference of the transmitted/reflected signal. The benefits of the increase in amplitude is obviously improved signal to noise ratio, a

resonant frequency can provide layer information by boosting the signal should this resonance be found. Figure 4.13 shows comparisons with (a) pulsing at a resonant frequency compared with (b) just below and (c) just above the resonant frequency. Notice the standing waves created when 4 waves are pulsed at 6MHz through a 2mm body with a wave speed of 3000m/s. Using equation 2.2, this gives a wavelength of 0.5mm, a quarter of the bodies width. This would be identified in the FFT plot in Figure 4.13d where the 6MHz shows much higher amplitude than the 5.5MHz and 6.5MHz signals.

(a) 6MHz pulse

(b) 5.5MHz pulse

(c) 6.5MHz pulse

(d) FFT comparison
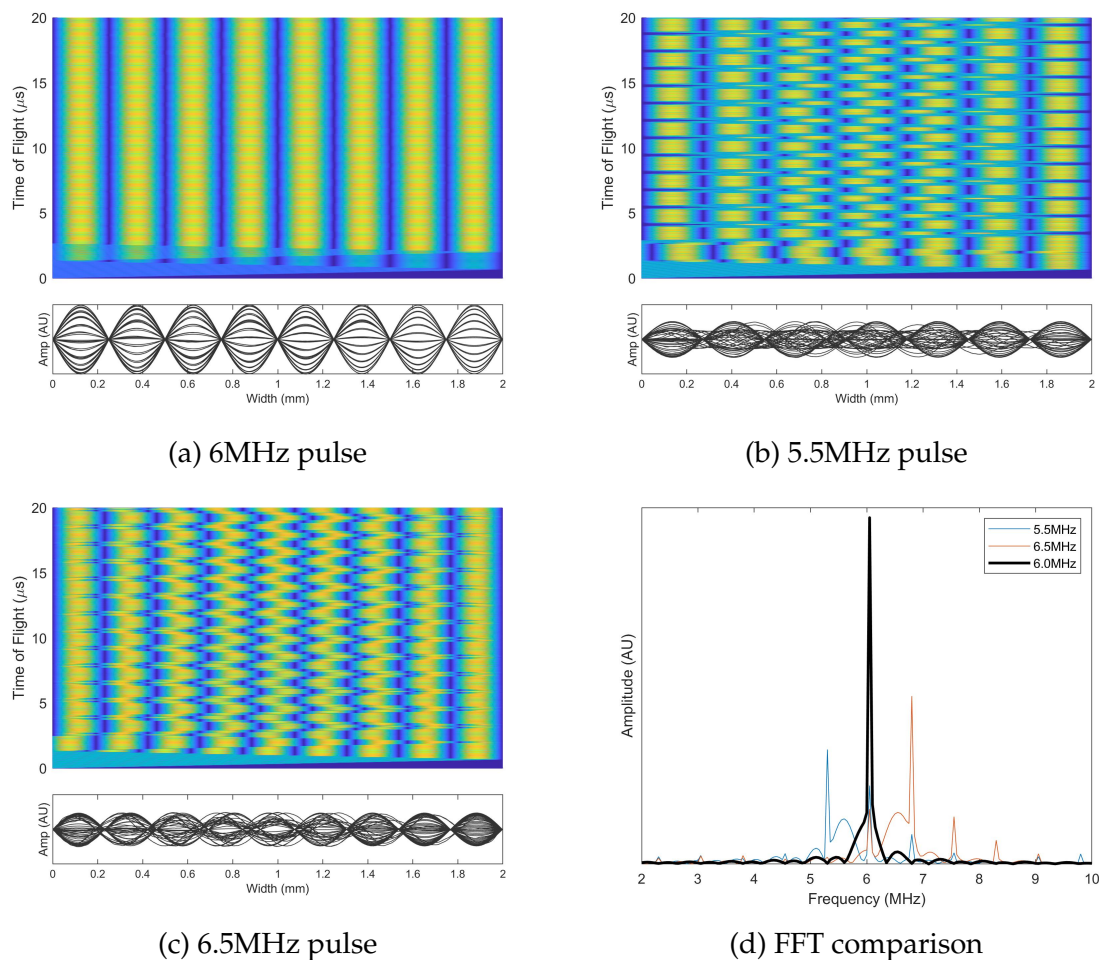
Figure 4.13: a) standing wave created by pulsing 2MHz waves through a 2mm body with wave speed property of 3000m/s. b) 5.5MHz and c) 6.5MHz fail to create resonant standing waves. d) high amplitude for the resonant frequency on the FFT.

To find the resonance of a layer using modelling, the layer thickness must by less than at least half a wavelength of the pulsed signal. Table 7 shows layer parameters similar to those in Table 5 along with the full and half wavelengths for 2MHz, 10MHz and UHFUS 70MHz pulses. The green wavelengths mark the waves that could successfully

Table 7: Model cell layer properties, wavelengths for 2MHz, 10MHz and 70MHz pulse frequencies. Range of minimum frequencies suitable to achieve 1 wave or 1/2 wave inside of layers. Waves smaller than layer shown in green. Suggested frequencies shown in blue.

Component	Thickness (μm)	Wave speed (m/s)	2MHz 1 wave (μm)	2MHz 1/2 Wave (μm)	10MHz 1 Wave (μm)	10MHz 1/2 wave (μm)	70MHz 1 wave (μm)	70MHz 1/2 wave (μm)	Range MHz (min)
Anode (d)	96	3800	1900	950	380	190	54	27	20-40
Anode (c)	96	3000	1500	750	300	150	43	24	16-32
Cathode (d)	60	5700	2850	1425	570	285	81	41	48-95
Cathode (c)	60	6500	3250	1625	650	325	93	47	54-108
Separator	25	1128	564	282	113	57	16	8	23-45

pass through each layer providing a full reflection at the interface with adjacent layers.

Running the 40MHz-70MHz ultra high frequency sweep through the cell gives the results shown in Figure 4.14, the surface plot is the absolute values of the waves passing through the layers (a single sine wave would show as a double peak). A resonance appears to exist in the cathode layers, characterised by the consistent single half wave that occurs throughout the response duration, similar to the ordered waves in Figure 4.13a. This is more clearly visible in the zoomed window on the right. This single peak, half wave, is present in both charge and discharged states. A resonance is identified in the anode layers throughout the cell where a 2-wave set of peaks appears, again this is marked clearly in the bottom panel of the zoom window.

Interestingly, the resonance, although somewhat weakened when discharged is still evident. However there are now three peaks visible which would be a 3/2 standing wave similar to that shown in Figure 4.12c. The time domain wave responses gained from pulsing at such high frequencies does not yield much if any useful information. In fact looking along the sensing edges (left most: pulse/echo or right most: pitch/catch) of the main body in Figure 4.14 would resemble noise with such a chaotic response. The signal in the frequency domain however, will show frequencies that produce resonances.

Comparing the signal FFT with the modelling parameters in Table 7 using the resonances identified in the wave development plot, some notable frequency activity can be seen. When discharged the cathode layers have a wave speed of 5700m/s and a thickness of 60μm, a 1/2 wave resonance is noted in the cathode layers in Figure 4.14, which would give a wavelength of $\lambda = 120$μm. Using equation 2.2, the frequency of this wavelength would be 47.5MHz. This is approximately marked (a) on the discharged FFT in Figure 4.15.
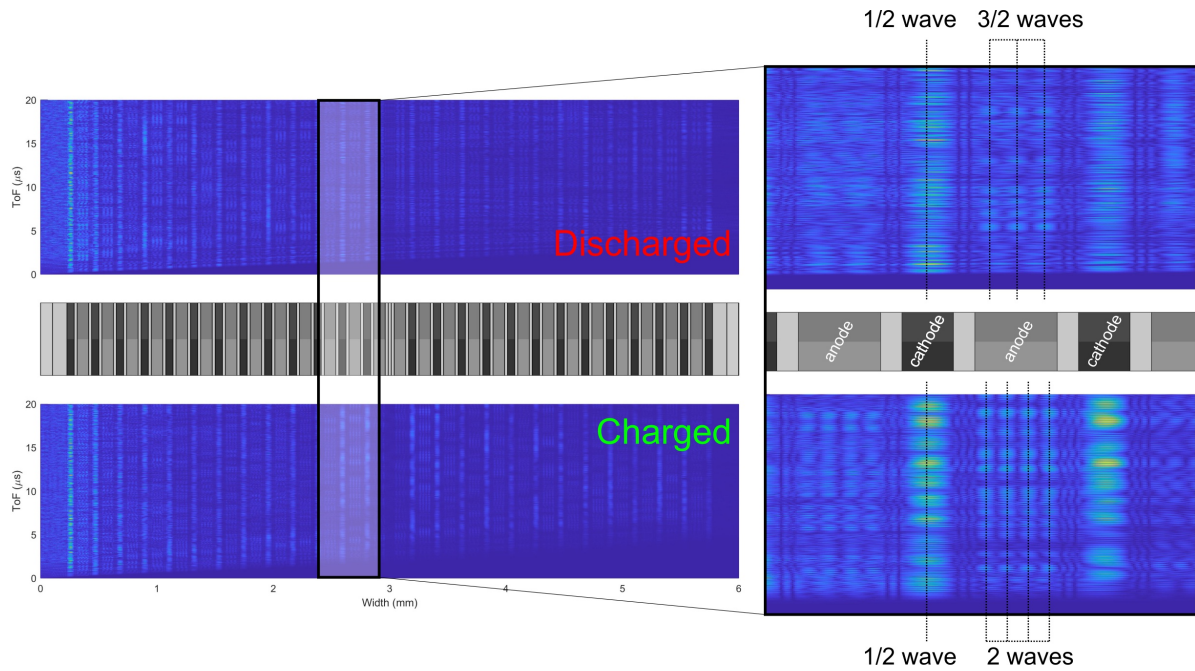
Figure 4.14: Identified wave resonances when pulsing ultra-high frequency ultrasonic waves through a multilayered body.

When charged the cathode layers still produce a 1/2 wave resonance, however with the altered material density and therefore wave speed (6500m/s), this shows as the 54MHz resonant frequency, marked (b) on the charged FFT. The anode (thickness 96μm), when discharged produces a 3/2 standing wave (albeit inconsistent), with a wave speed of 3800m/s. This would show up at approximately 59MHz and is marked (c) in the discharged FFT whilst the 2 wave resonance in the charged anode with wave speed 3000m/s features at 62MHz in the charged signal, marked (d).
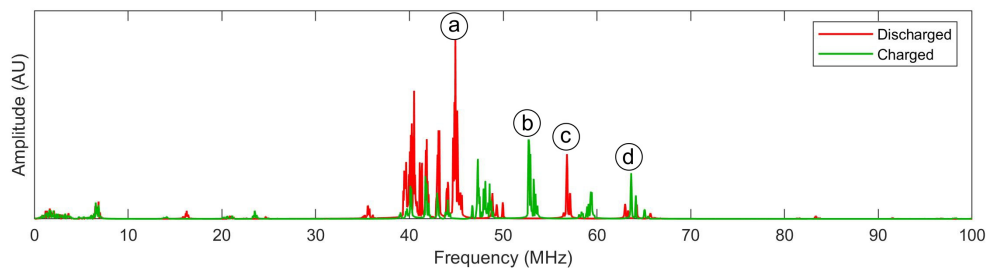
Figure 4.15: Signal response of a through pulse in the frequency domain with notable frequencies marked.

These insights were gained very late in to the work and as such have no experimental data to see if these assumptions and results would hold and be achieved when testing

on a cell. The theory and modelling covered suggest this would form an interesting avenue to explore in future.

When conducting this work, some key observations arising to guide the experiments would be as follows. A FFT is best taken from a through pulse, for reasons covered in section 4.5, high frequency signals will struggle to penetrate a cell, in pulse/echo such high frequencies as this have signal dominated by early layers, a through pulse is desirable as the response is guaranteed to have passed through all layers. This demands a pair of sensors rather than one and will undoubtedly require signal amplification to force the waves through. The FFT itself does not necessarily alter linearly, so taking measurements is difficult, there will be a transition if the resonance changes the wave multiple, such as the 3/2 to 2 wave transition seen in the anode. Tracking this transition would be challenging.

It is accepted that whilst this method appears to work with modelling, only experimental testing will confirm if the resonance method will work, it is assumed that there would be some success as the material changes during charge cycling are still well defined and consistent across the cell. From the modelling, with the battery parameters stated, Figure 4.15 shows there is activity in the 40-65MHz frequency range. Using a chirped pulse to include these frequencies would be recommended. The minimum frequencies to achieve resonance in a cell containing the modelled parameters are shown in blue in Table 7. In theory, resonance could be achieved using a 32-54MHz frequency range.

The advantages of this ultra high frequency battery inspection would be that this method would go beyond providing a measurement of change within the cell of a single parameter such a charge or health. Using this method could potentially advise upon specific parameters from within the cell providing measurable changes, such as wave speed and thickness of components. Deviations from standard/expected parameters would show clearly in the FFT of the signal, being a sensitive monitoring method.

4.8   Conclusions

- From this modelling, the sensor and pulse frequency choice is established. Visual representations of the effects of pulse frequency selection are displayed in Figure 4.9, the discussion contained in Section 4.5 states that lower frequency options can struggle with cell penetration whilst lower frequency is prone to loss of layer

detail. Providing a theoretical explanation why $\approx$ 2MHz is an optimal frequency for a battery cell based on modelling created for this work.

- The modelling contained in this section, based on the 1D wave equation. Successfully simulates reflections where the wave encounters material boundaries.

- Small dimensional, density or layer ordering changes can cause the signal to vary from battery to battery, this can impair the intensity of wave changes as a function of state of charge and could render envelopes difficult to obtain should that be the method of measurement.

- Purpose designed outputs provide good insights into the development of a transmitted signal as it travels through battery layers. The wave development plots and animations show wave travel in space and time.

- Whilst the model gives indications of the wave responses expected when pulsing through a cell. Further development would be required to expect more precise results for direct comparisons with experimentally obtained signals. This would involve the more complex wave speed calculations, designed to include material elasticity for example, a variable held constant throughout this work.

- Modelling ultra high frequency (up to 70MHz) pulses through a battery cell provides some preliminary evidence that obtaining resonant standing waves, trapped in layers could feedback on layer specific changes. The modelling in this section guiding decisions on potential future work.

- Simulation of temperature effect on signal response built into model, by altering the wave speeds of all layers uniformly.

5 Apparatus and Data Analysis

In this chapter the apparatus used during experimental testing is described. This covers hardware and software used to both generate and acquire the ultrasound signal pulses in addition to the sensors, bonding methods and selected pulsing parameters. Battery charging equipment and charge cycling software is detailed. Battery cell surface temperature recording equipment is described. Details of a test kit developed for large capacity cell testing are included in this chapter. An overview of test data synchronisation and processing is provided in this section. The development, process and sample outputs of a bespoke MATLAB script are covered, providing details of various data comparison methods and visualisations.

5.1 Set Up and Equipment

The pouch cells used during testing were all commercially sourced lithium polymer rechargeable cells having a nominal voltage (V) of 3.7V, a discharge/charge cut-off of 3.0V/4.2V and a capacity of 2Ah. The maximum discharge/charge current for the cells was 2000mA (1C)/1000mA (0.5C). Later in the work, testing is performed on 52Ah large capacity cells.

Commercial longitudinal contact transducers were used to both transmit and receive an ultrasound pulse in a pulse/echo arrangement as this is the simplest and most cost-effective method of capturing ultrasound data. The sensor was clamped in place and a high temperature ultrasound gel was used as couplant. The clamps were hand tightened enough to hold the sensor in place, minimum pressure was applied such that the sensor could be moved slightly while held in place. This was to ensure no possibility of causing an accidental wave interface and in general care of the battery itself.

The sensor was connected to a PICOSCOPE 5000 Series oscilloscope which was used to generate the pulse and record the reflected waves. The pulse consisted of 2–3 sine waves at a frequency of generally 2MHz according to the discussion in Section 4.5. The response signal captured ranged from 0–2µs to 12–30µs with a time resolution of 2–8ns. Signal captures were taken from every 60s to 300s depending on test length and each capture was recorded as the average of 20 captures taken at 20Hz.

Bespoke LabView software was used to control the PICOSCOPE in both signal generation and capturing the signal response. The software was also connected to a NI-9211

thermocouple input module to record the surface temperature of the cell during charge cycling. A schematic of test configuration is shown in Figure 5.1, cell images are shown in the top left corner. As the C-rates for the charge cycles were low and within the manufacturers stated maximums, no swelling occurred during testing and the cells remained in perfect physical condition throughout.
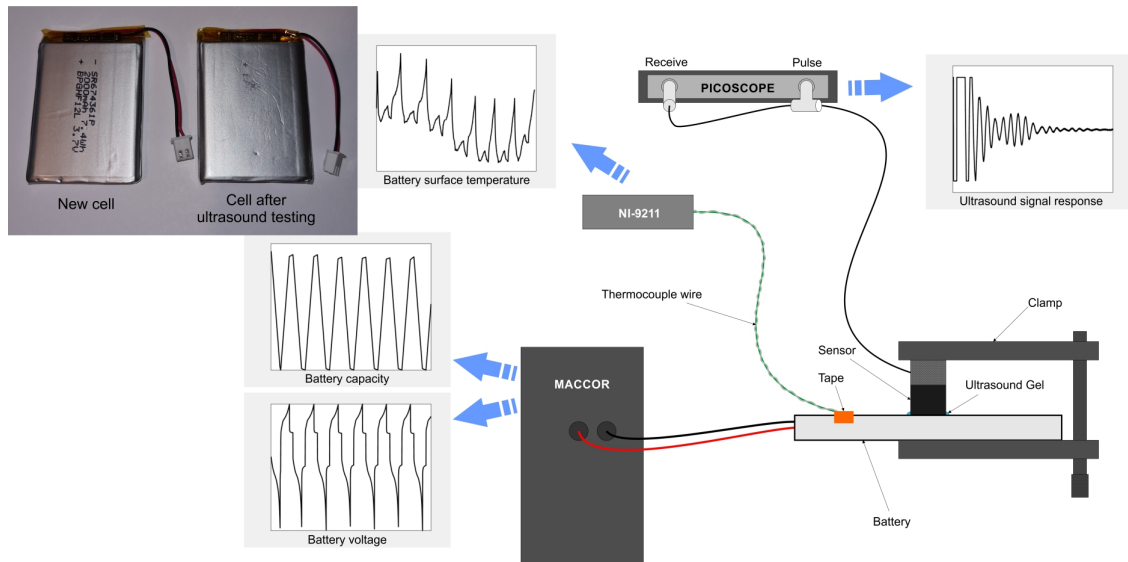
Figure 5.1: Test set up schematic.

The battery was connected to a MACCOR 4000 Series Test System (shown in Figure 5.2a) which controlled the charge cycling stages. Test were cycled according to a custom built programme generally consisting of a combination of fixed current, fixed voltage and timed rest periods. In the fixed current stages, the rate of charge/discharge was generally 0.5C. The MACCOR records the battery voltage during charging and charges up to 4.2V and discharges down to 3.0V, additionally, the Ah/s data is accumulated during cycling to provide a battery capacity profile, providing an alternative state of charge rating for the cell.

A Cadex C7200 advanced battery analyser (shown in Figure 5.2b) was acquired during the course of this work and was used for some of the later testing. This provided a convenient means of bench-top battery charge cycling testing. Whilst the control over battery procedures is not as detailed as with the MACCOR, robust CCCV tests were successfully conducted using the Cadex. A 07-110-0115 SmartCable adapter for the Cadex was used. This adapter had crocodile clips that were attached to wires inserted into the battery connection block as shown in Figure 5.3. The Cadex C7200 was con-
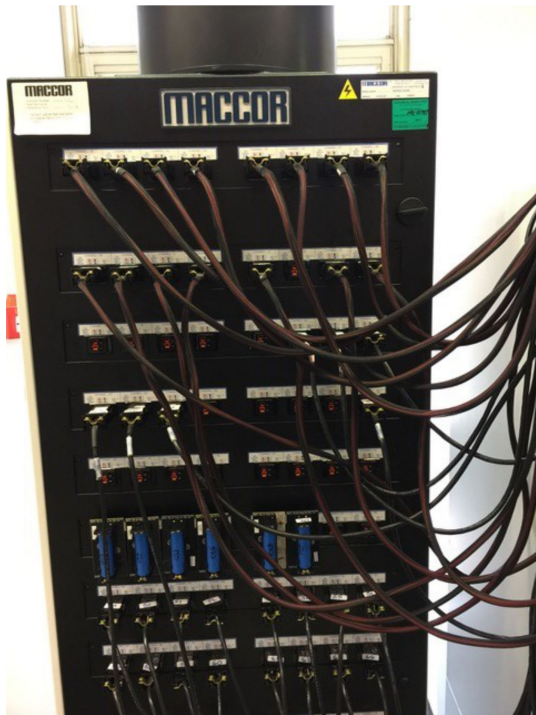
(a) MACCOR 4000 Series   (b) Cadex C7200

Figure 5.2: Battery charge cycling apparatus.
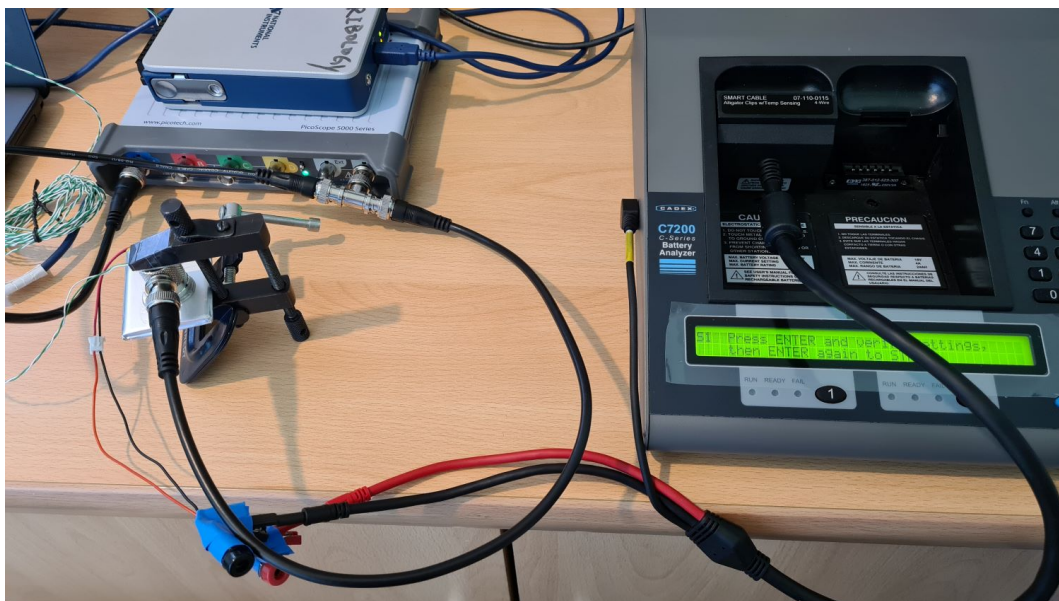
Figure 5.3: Cadex C7200 during bench-top testing.

trolled using BatteryShop software installed on a laptop dedicated to hardware control and data acquisition.

To facilitate the generation of high amplitude pulses through large capacity cells, with the option to place multiple sensor pairs across the cell surface. An ultrasound test kit was designed and built to specifically meet these requirements. Contained in the test kit, shown in Figure 5.4 is the standard PICOSCOPE 5000 oscilloscope, a high frequency amplifier and a 16 channel multiplexer (MUX).

Figure 5.4: High frequency amplifier, 16 channel, ultrasound monitoring test kit.

The results gained in the majority of testing in this work were obtained using the test set up in Figure 5.1, with no amplification and a single sensor in pulse/echo configuration. Table 8 shows a pulse/echo signal response, without amplification, records maximum peaks measuring approximately 0.004V. Using this as a benchmark, pulsing through a standard 2Ah cell is over twice the signal power at 0.01V. Using the amplified test kit in the same configuration (through pulse) provides a signal response with peak amplitudes of approximately 0.14V, 14x amplification. Using this method through large capacity 52Ah cells measured a signal with peaks measuring 0.04V, a 10x improvement in signal strength on the benchmark.

The signal response amplitude when the the MUX is active remains intact, albeit with cross-talk effects at the beginning of the wave response. As such the test kit is regarded

Table 8: Signal amplitude values for various cells, amplification and sensor configuration

Cell	Sensor configuration	Amplified	Voltage (V)
2Ah	Pulse/echo, single sensor	No	0.004
			0.01
	Pitch/catch, through pulse	Yes	0.14
52Ah			0.04

as powerful, versatile ultrasound monitoring equipment designed and developed during this work. The large cell capacity results are covered in Section 6.7.

5.2 Analysis Methods

Three data sets were retrieved (ultrasound response, charge data, surface temperature) during an experiment. The ultrasound data contains various information types, such as signal amplitude and time of flight changes which will vary based on which part of the signal a measurement is taken. Also signal power and frequency domain information is obtainable from the waveform. Additionally, the battery charge data provides voltage, current and estimated battery capacity information. The analysis method developed was designed to incorporate all methods of data analysis such that the same data sets can be arranged in a variety of ways to assess the strongest correlations. There is also capability of tracking and measuring multiple signal peaks across the signal response to compare the results of each peak individually. The flow chart in Figure 5.5 shows these various methods of analysis available, the outputs of which will be discussed in detail.

The plots in Figure 5.6 show the initial formatting and data synchronisation process, the ultrasound and battery charge information is presented here with the peak tracking evident in Figure 5.6b. Note the tracking is colour coded to match the nature of the charge cycle which reveals a clear, significant and repeating pattern throughout the cycle stages. This peak tracking is a viable option for the automation of battery readings and therefore suitable for use in a battery management system.

Some studies take measurements directly from the waveform and select a peak from which to take readings[41,47,56], most commonly, the largest peak found in the response. Popp et al. use a Schmitt-trigger method that captures a signal peak over a threshold and turns these into digital rectangular signals from which to measure[30] and signal power has been used as a means of capturing and quantifying ultrasound signal re-
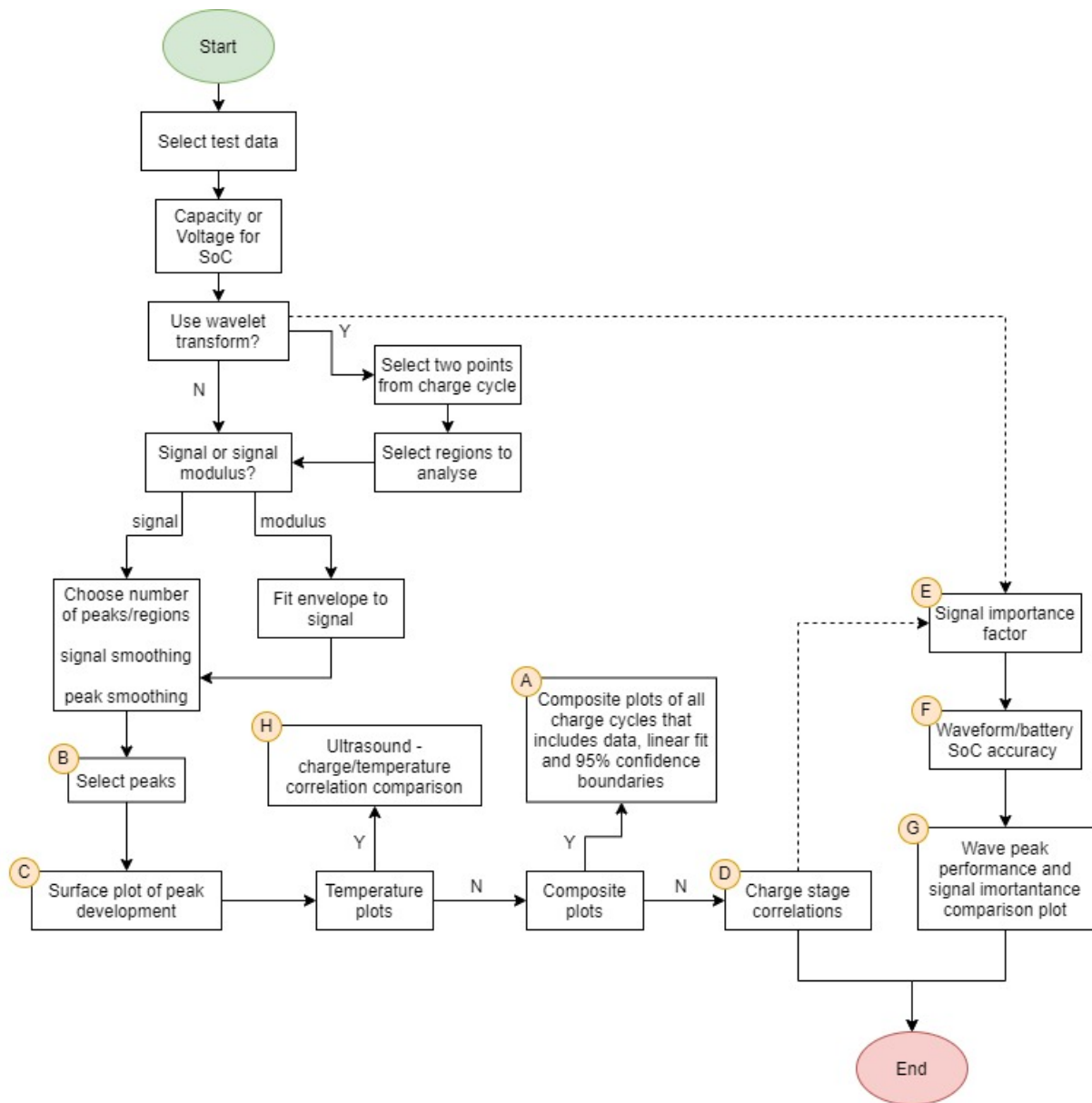
Figure 5.5: Analysis flow chart for analysis script created in MATLAB.

sponse[19]. Others have taken a readings from the peak of a signal envelope[51,57]. This can often, but not always, correlate with battery state of charge, however obtaining an envelope that remains consistently strong across charge cycling is difficult to guarantee whereas selecting a peak directly from the signal is always possible. The problem with opting to measure from a single peak is being able to correctly identify the peak that carry battery charge insights. The following section compare the results of various measuring options to help identify a robust signal analysis strategy.
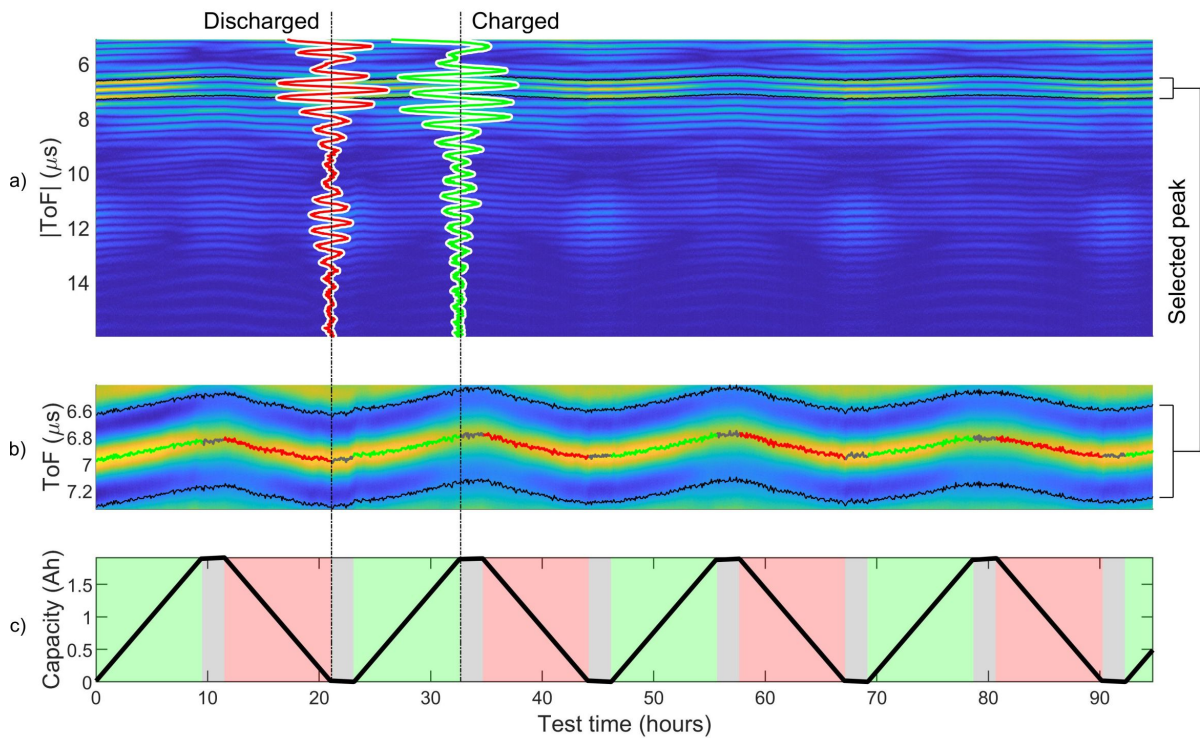
Figure 5.6: a) Measured ultrasonic amplitude intensity map as a battery is charged and discharged, each waveform (A-scan) is stacked (two sample signals shown, discharged state in red and charged state in green). The absolute values are shown in this plot for clearer viewing. The black solid lines show the area bounded by the user with a zoom of this in b) the peak is tracked throughout the test, each point is colour coded to identify the part of the charge cycle (green = charge, red = discharge, grey = rest), in c) The battery capacity is plotted over a colour coded background following the same colour coding. The black dashed vertical lines show the position of the two sample waveforms

Comparisons between measuring directly from a single peak and a signal envelope (taken using the envelope.m function in MATLAB) are shown in Figure 5.7, plots (c) and (e) relate to the single peak selected in plot (a), and plots (d) and (f) relate to the envelope peak from the same signal in plot (b).

Peak tracking using either an individual peak or the envelope peak provides the ability to take amplitude and time of flight measurements as the battery is charge cycled. The peak tracking is colour coded (red: charge, green: discharge, grey: rest) to highlight the battery charge status in Figure 5.7c and d. The change in time of flight and amplitude is recorded from this peak tracking throughout the duration of the charge cycling test, taken at the maximum point of the peak. Figure 5.7e and f, show correlation plots for the amplitude (top row) and time of flight (bottom row) measurements taken dur-

ing charge cycling, the plots are also colour coded to show the different charge states according to the same scheme, with shaded points identifying data by its particular cycle.
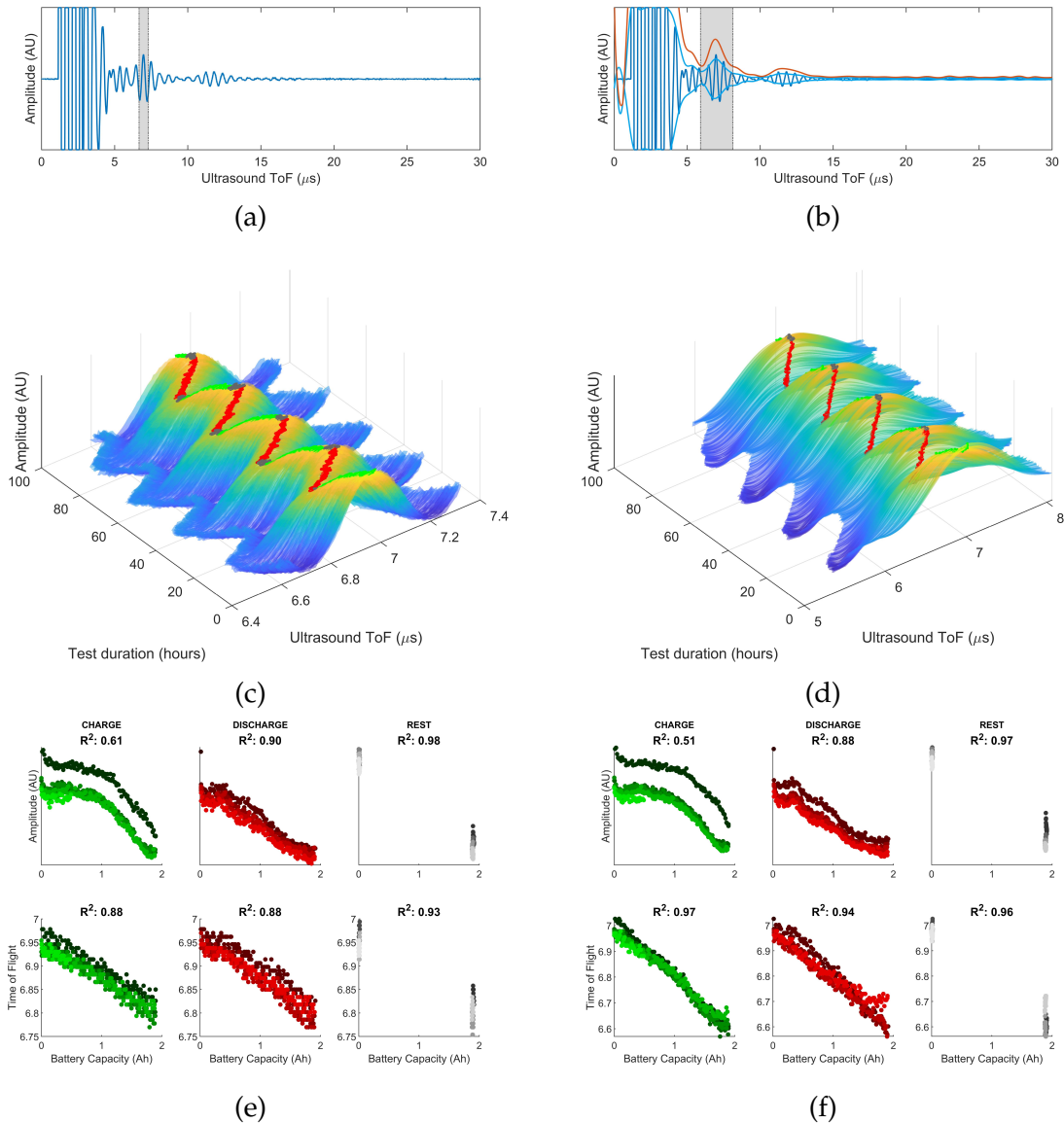
Figure 5.7: a) A single peak directly taken from the ultrasound response is selected and tracked throughout the test [step B in the flow chart Fig. 5.5] b) the peak of an envelope can also be tracked in the same manner c) the graphical display of the peak evolution throughout the test [step C in the flow chart] d) graphical display for the envelope tracking e) separated correlation plots for charge/discharge/rest for the single peak for both signal amplitude (measured in arbitrary units) and time of flight [point D in flowchart] f) correlation plots for the envelope.

The accuracy of each method typically depends on the signal and it is not obviously predictable which method will yield the best correlation. An envelope can help with

signal to noise ratio and can perform some data smoothing effects. It can however combine the effects of the inaccurate parts of signal reducing the overall correlation with battery charge. In the composite plots in Figure 5.8, showing the same single peak and envelope analysis as in Figure 5.7, the signal envelope performs well and provides a slightly stronger R^2 value ($\sim$0.95) with battery state of charge than the single peak ($\sim$0.88).

In addition to the envelope not always providing the strongest charge correlations however, importantly, reliance of taking measurements from envelopes is problematic. As shown in the modelling, in some cases an envelope may be difficult to capture.
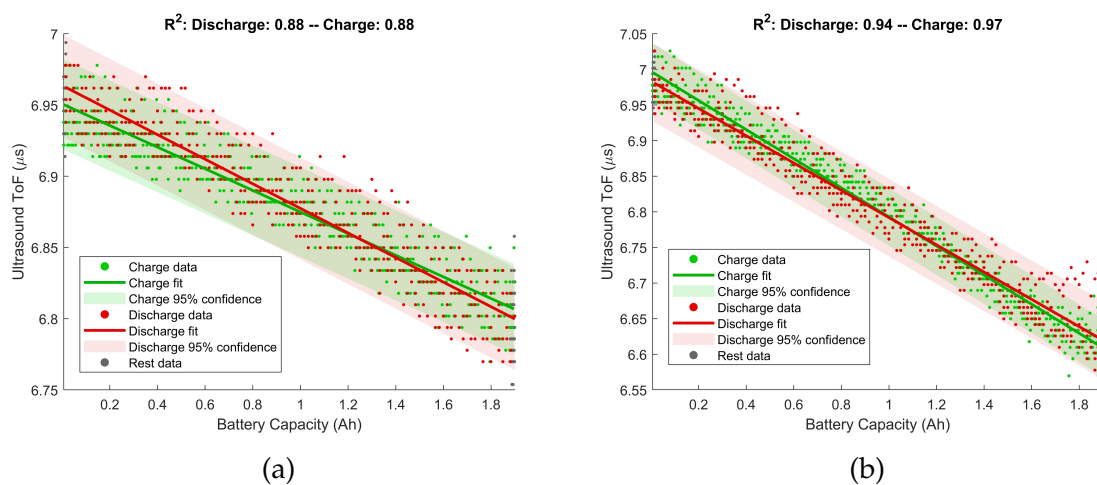
Figure 5.8: a) Using a selected peak directly from a waveform to monitor battery state of charge and b) using the peak of a waveform envelope [point A on flow chart].

A note on the accuracy of the data. As this study is concerned with the quality of different peaks within the signal rather the quality of signal itself, raw captured data is shown throughout. There are several means of improving data accuracy however, denoising can be performed in data processing, the data in Figure 5.9 has been denoised using a `sym4` wavelet twice, firstly the selected peak is smoothed to aid peak tracking accuracy, following from this the peak tracking itself is denoised, along both the ToF and amplitude axes. The results are overlaid, this simple measure both improves the precision of the relationship between US and SoC and gives some further context to results, an isolated cycle becomes clear, likely due to a temperature change.

Data acquisition improvements can also be made, such as increasing the capture rate from 20Hz or increasing the pulse voltage to improve signal to noise ratio. There are several alternative methods of arranging sensors as discussed previously and whilst

many of these studies aim to improve signal accuracy with respect to battery information, this study is focused on the qualities within the signal itself.
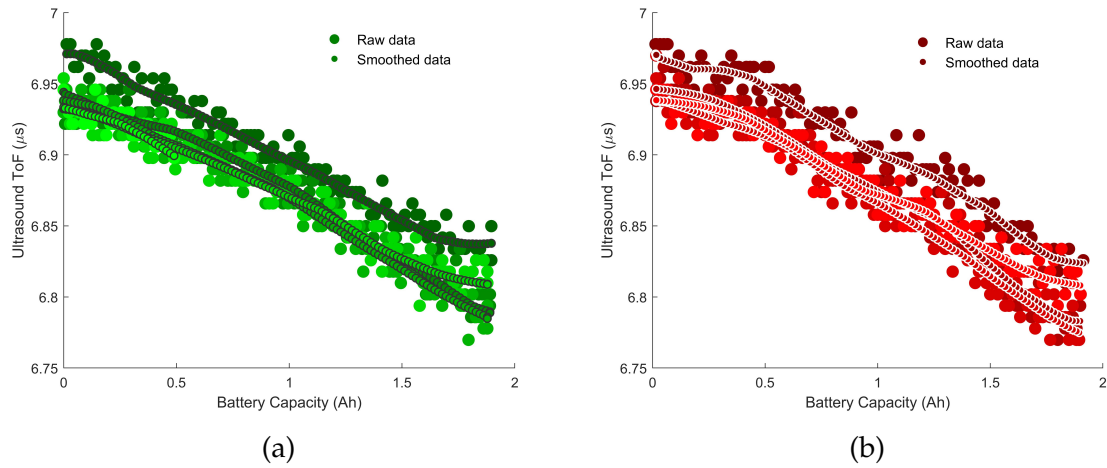
Figure 5.9: a) smoothed charging data b) smoothed discharging data.

5.3 Conclusions

- The experimental apparatus required for ultrasound monitoring of commercially obtained, 2Ah lithium-ion pouch cells during charge cycling tests is detailed. Sensor type, frequency and configuration, bonding methods, ultrasound generation/acquisition, battery cycling and temperature monitoring hardware are introduced.

- Modifications to the standard setup, required to facilitate ultrasonic monitoring across the surface of large capacity, 52Ah cells are detailed. This setup incorporates signal amplification and a 16 channel multiplexer. Sensor placement options are considered to ensure strong signals and battery measurements remain possible.

- Data synchronisation and analysis script created in MATLAB is introduced. A key feature being peak tracking, designed to measure ultrasound reactions with respect to changes in state of charge in a battery cell. Developed a range of analysis tools within the MATLAB script including; visualisation methods, correlation testing, signal enveloping, multiple peak tracking and data smoothing.

6   Standard Charge Cycling Tests

This chapter explores the results of experimental, standard charge cycling tests conducted on lithium-ion batteries. Common ultrasound measuring techniques are investigated, comparing the reliability of each method and how each is affected by temperature fluctuations. Difficulties in obtaining a desired or expected signal response presented by the diverse nature of cell geometries is explored, with a suggested 'smart peak selection' technique developed to combat this.

Modelling developed in this thesis is utilised to provide greater context to received signals. Instrumentation decisions are evaluated using a combination of modelling and experimental results, for example pulse/echo and pitch/catch through pulse configurations and the effect of bonding methods. Tests are conducted on large capacity cells where elevated C-rates are assessed. A suggestion is made for calibrating ultrasound time of flight measurements to reduced temperature effects at high C-rates.

6.1   Measurement from Signal Amplitude or Time of Flight

As previously mentioned in section 3.3, published studies used signal amplitude and time of flight shift to monitor ultrasound changes for battery measuring purposes. In Figure 6.1a, a clear linear relationship between battery SoC and ultrasound time of flight is visible. The same relationship is much less clear for peak amplitude (Figure 6.1b), especially for the charge part of the cycle which has a R^2 value of only 0.01, being non-linear and complicated to measure.

Figure 6.1c shows the correlations for SoC and temperature against change in ToF and signal amplitude in each peak across the whole signal, with the selected peak measured in Figures 6.1a and b highlighted in grey. The highest correlation in this test is the SoC/ToF at the selected peak. Signal peak amplitude can occasionally provide good SoC measurements but being sensitive to temperature changes makes it an erratic and unreliable indicator of battery charge, this is discussed in Section 6.5.

6.2   Difficulties Obtaining Signal Envelope

As mentioned in section 4.3, in some instances, it is difficult to produce suitable envelopes from which to take readings (example shown in Figure 6.2a). From the model
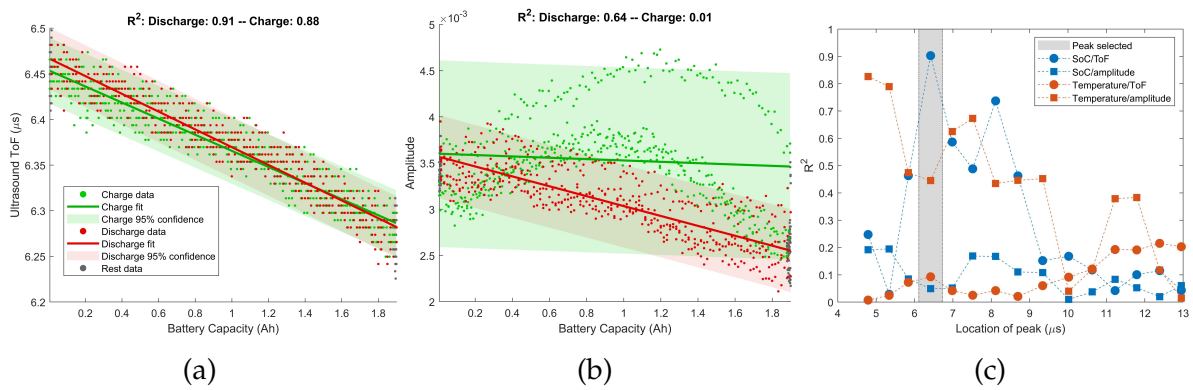
Figure 6.1: Composite plots with linear fit details, a) time of flight from a single peak measurement and b) signal amplitude from the same single peak measurement. c) the location of the peak displayed in a) and b) with measurement correlations from across the signal for comparison, averaged using next peak data for clearer viewing.

in Figure 4.6b it was shown that, apart from being an instrumentation issue, flattened signal could result from the specific nature of the layered properties in the battery, this could typically be caused by some significant interface boundary along the wave path rendering the incident wave unable to return back to the sensor with clarity (e.g. casing, gas build-up, current collector, large layer acoustic mismatch). It is important to note that this is not a signal to noise issue and increasing the pulse voltage will merely increase the whole signal, including reflections.

The linear fit plots in Figure 6.2b and c show the problems when deciding from which part of the signal measurements should be taken. Peak #1 is taken where there is a large defined peak available having good signal to noise ratio and at around 6μs should contain some of the first reflections when comparing with the model and other experimental results. Peak #2 is from much later in the waveform that has suffered significant attenuation with a poorly defined peak. However, peak #1 shows little relationship with the battery SoC, whereas peak #2 has a good correlation. Whilst the R^2 values are not as strong as in other tests, it remains a valuable exercise to identify a suitable method that would maximise the battery information should a signal such as this be obtained.

Note this test contained a constant voltage section in the charge cycling, this is denoted in the peak tracking using a blue line. The blue line shows that the ultrasound peak continues to develop along a similar trajectory to the green (charge) line, until the grey (rest) period is reached. The linear fit for this data confirms the relationship is an extension of the charge data albeit at a different rate which would be expected as the current gradually decreases approaching capacity.
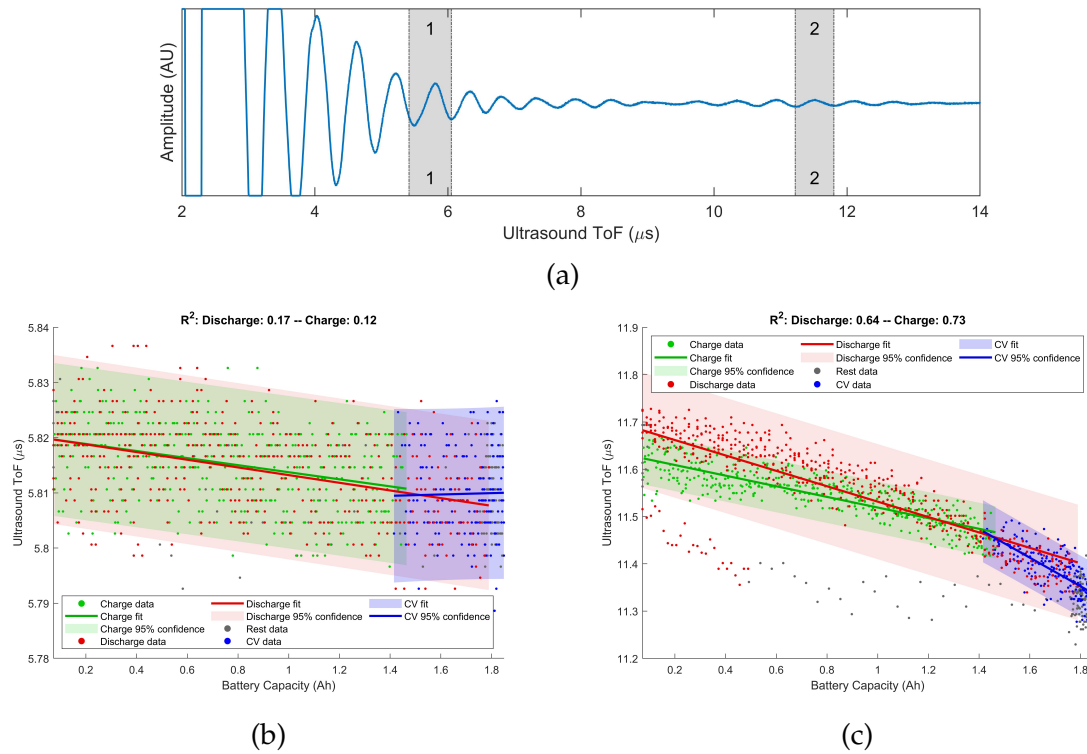
Figure 6.2: a) Experimental test signal response. Not suitable for taking an envelope, two peaks tracked for battery state of charge accuracy. Linear fit for peak #1 shown in b) and linear fit for peak #2 shown in c).

6.3 Temperature Effect on Ultrasound Signal

The speed of sound of materials varies with temperature and since battery temperature fluctuates during charge cycling it needs to be considered. In Figure 6.3a, battery temperature is recorded using a thermocouple data logger as detailed in section 5.1. The temperature data is synchronised with the charge cycling data and the clear repeated effect of charge on cell temperature is evident. The laboratory ambient temperature is also seen to have an effect altering the underline baseline temperature, tracked using the red sine wave with the high being the warmest part of the day and the low being the coolest.

Figure 6.3b shows the correlation between change in ultrasound ToF for each individual peak in the signal response and battery SoC/battery surface temperature. This clearly shows a greater relationship between US and SoC when compared to US and temperature. There is a very strong relationship at 6–9μs with SoC whilst the temperature shows no relationship until a switch in correlation occurs late in the signal.

Changes in global wave speeds are built into the model to simulate cell temperature changes as described in section 4.6, two examples are shown in Figure 6.4. In model a) the temperature gain is set to 5°C during cycling, this occurs both as a combination of ambient cycling temperature and in accordance with the charge cycle. This shows similar results to the experimental data, the correlation is strongest with battery charge. In model b) the temperature gain is increased to 25°C and this results in a reduction in battery charge/US correlation and an increase in temperature/US correlation. This suggests that significant temperature increases, either ambient or internally driven, will limit the charge measurement capability of the ultrasound signal.

(a)   (b)
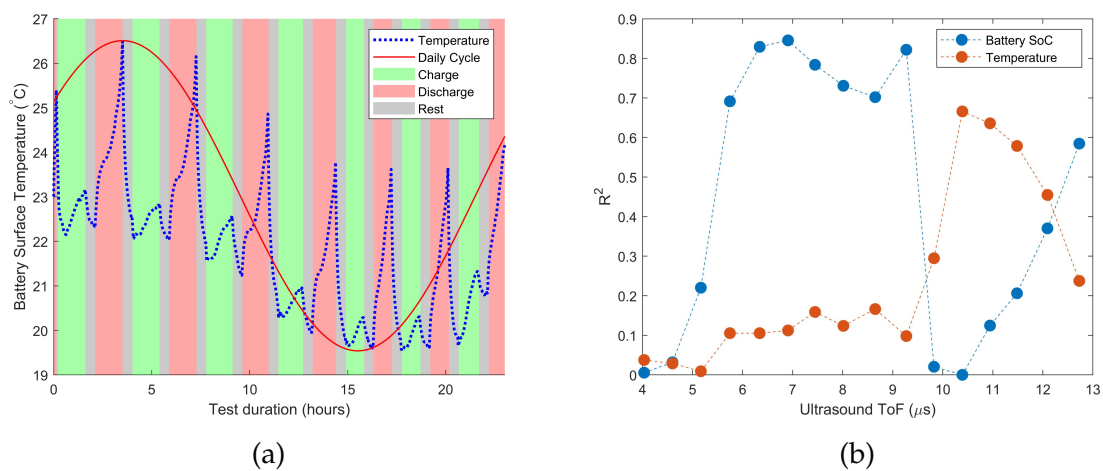
Figure 6.3: a) Battery surface temperature variation recorded during testing. The coloured bars behind the plot denote the stage of charge cycling (charge/rest/discharge/rest). The red line shows the daily cycle in which a maximum and minimum ambient temperature affects the base line. b) Ultrasound/battery SoC and ultrasound/battery surface temperature correlations shown across the length of an ultrasound response [step H on flow chart].

A strong signal with good cell penetration contains good battery density change and therefore battery charge data. Locating this region when taking measurements is vital, parts where the incident wave is traveling through the cell and is away from the sensor edge (for example 0–4μs and 10–12μs in the waveform development plot in Figure 4.8a) show the signal to have weak correlation with battery charge. This is shown in both the experimental data in Figure 6.3b and in the model data in Figure 6.4a. In both cases, where charge correlations diminish, temperature correlations increase. Here, signal peaks contain accumulations of shallow wave penetrations largely influenced by the casing materials where changes in wave speed can only be attributed to temperature changes.
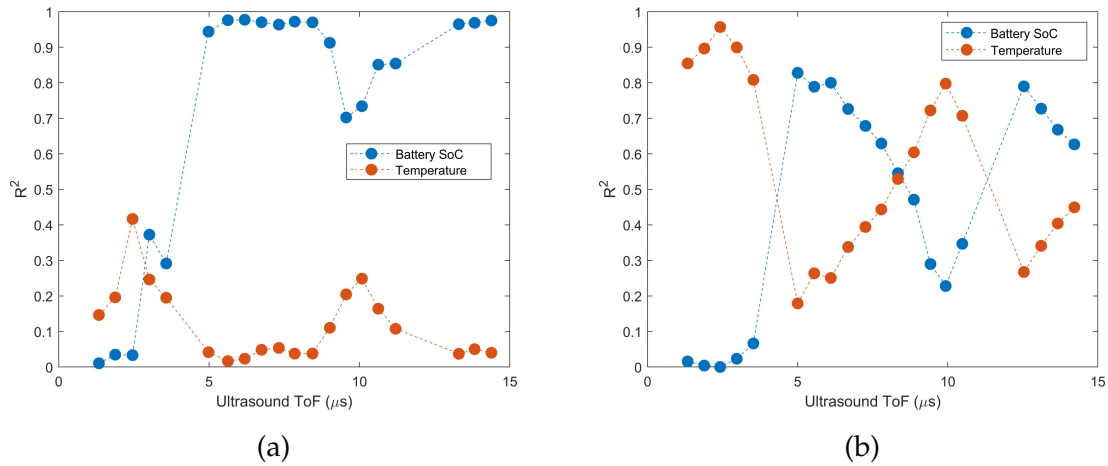
Figure 6.4: Battery SoC/temperature – ultrasound correlation plots a) 5°C gain during charge cycling and b) 25°C gain during cycling. The model increases the global wave speed 1.0 m/s for each °C increase (calculated using ambient temperature shift in time of flight on a resting cell).

6.4 Half Reflections

As discussed in Section 2.2 there are different battery construction types, each of which is not obvious from an external visual inspection of the cell or often by checking the manufacturers specifications. Figure 6.5a shows an experimental waveform response when pulsing through a pouch cell with a thickness of approximately 6mm. In a single sensor, pulse/echo arrangement (top), the collection of peaks in the blue shaded area could be assumed to be the first reflection from the opposing face, with the following collection of peaks in the grey shaded area being a second reflection. The through pulse signal in Figure 6.5a (bottom) shows the the first collection of peaks to reach the opposing side takes approximately 5-6μs and arrive at the opposing sensor face during the blue shaded region. Using this information and displaying the two capture methods side by side shows that the peaks in the blue shaded region in the pulse/echo signal can not be a full reflection from the opposing face. Rather, it appears that this first collection of peaks is a *half reflection*, being a feature of cells utilising the 'jelly-roll' construction.

This center spacing layers and mirroring around the center is replicated using the model as shown in Figure 6.5b, where the same wave characteristics are clearly visible. In this model there are no extra materials at the centre of the cell, the layers that occur in the first half of the cell are mirrored and repeated in the second half, there exists one

(a) Experimental responses

(b) Model responses

(c) Waveform development
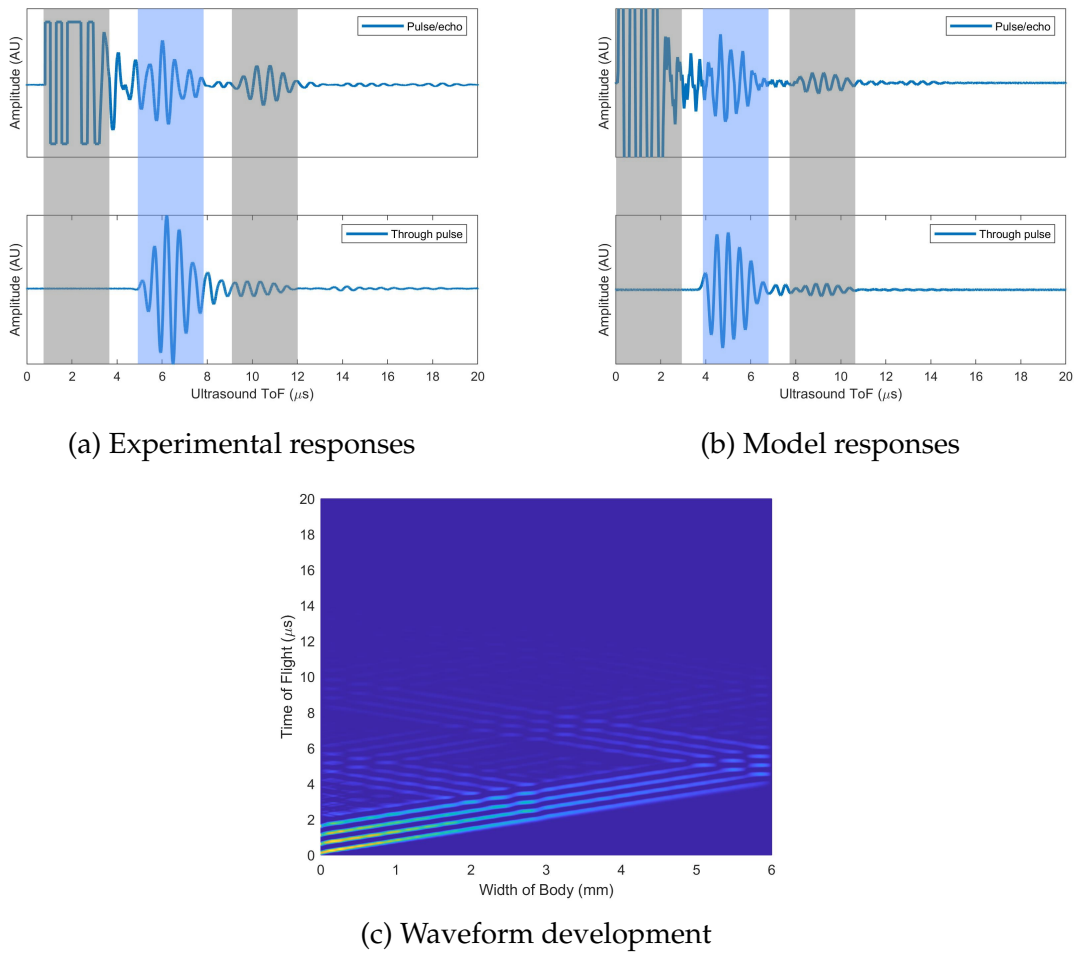
Figure 6.5: a) Waveform response from experimental test, b) Waveform response from model, in each [top] pulse/echo [bottom] through pulse. Shaded regions shown repeating time periods containing reflections. c) waveform development plot from model showing clear reflected signals from approximately half of the cell body

additional separator layer that simulated the space for the layers to wrap around. As this result is from the model, the waveform development plot shown in Figure 6.5c can be inspected. From here it is clear that the first packet of waves received in pulse/echo configuration are a significant collection of waves that return to the sensing edge from the half way point of the cell.

During testing, experimental analysis has been performed on the first reflections, as these have generally been providing the best correlations with battery SoC. This could call into question whether this really is the best place from which to take readings, in the knowledge that the measured signal has not travelled through half of the body under inspection. Any information about layers further than the mid point is compro-

mised and whilst this gives good SoC readings, a holistic view of the cell is hampered. In this model, the central winding space is enough to create the barrier to send a group of signals back to the sensor with strength from which to take readings. Experimentally, this could be any barrier with enough material property discrepancy to cause the large reflection, such as the current collector tabs that are generally attached to the end of the electrode layers and feed outward from the centre space of the winding.
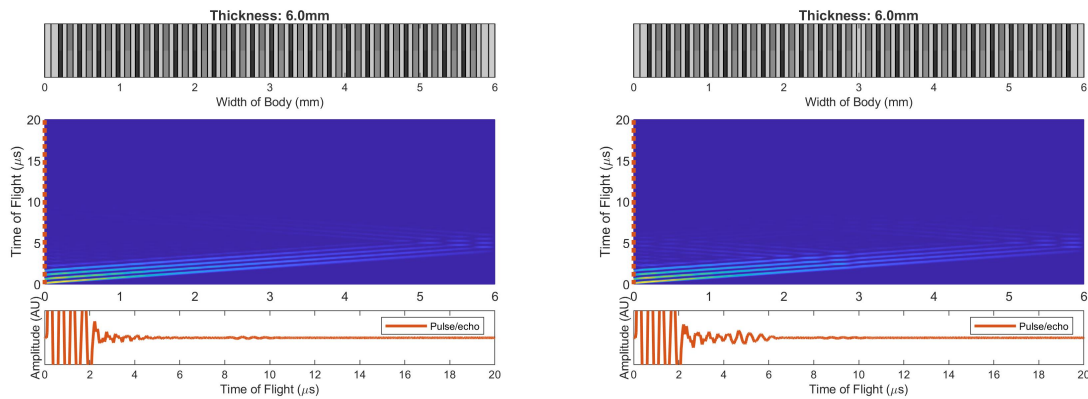
(a) Stacked　　　　　　　　　　　　　(b) Jelly roll

Figure 6.6: a) model of stacked layer construction, b) model of jelly roll construction. In each; [top] scale graphic showing layered construction, [center] waveform development, orange dashed line represents sensing edge, [bottom] waveform response from sensing edge (pulse/echo).

When pulsing through larger cells, or if the power available to generate the ultrasonic pulse is limited, a stacked layered battery construction can present challenges retrieving a measurable signal. The example in Figure 6.6a shows that when the signal has no significant interface to gather reflections from, the waves continue to the opposing edge somewhat intact. There is reliance then on the waves having the strength to complete the return journey with enough power to enable a reading. In this case the signal has attenuated almost entirely and no reading would be possible.

Note the subtle difference in the construction in Figure 6.6b, the jelly roll construction causes the layer structure to mirror and repeat around the centre with a single additional separator included for space. This simple measure is enough for the signal to reflect the signal back toward the sensing edge with enough power from which to take readings. It is believed that the majority of measurements in this work have been taken from *half reflections* such as this. This does present the problem of measurements being potentially blind to any activity occurring in the far side of the cell, such as gassing.

More precise information like the development of uneven layer thicknesses or uneven density distributions would be potentially lost from the far side of the cell. However, currently in ultrasonic inspection of batteries, the analysis and wave interpretations, especially with simple, single sensor methods are not sophisticated enough to retrieve this information if it were available in the signal.

This presents two possible solutions to finding that the stacked construction of the cell under inspection causes the signal to attenuate before returning to the sensor. The first solution is to simply increase the power of the pulses sent through the cell to force the reflection all the way there and back to the sensor. The results of increasing the power with signal amplification is shown in Figure 6.7a, the wave successfully travels the opposing edge and returns intact and with strength from which measurements can be taken. This however, a simple solution in theory, in practice could result in expensive or dedicated equipment to ensure signal strength is sufficient to overcome this issue only present in certain battery constructions.

(a) Increased power   (b) Artificial barrier
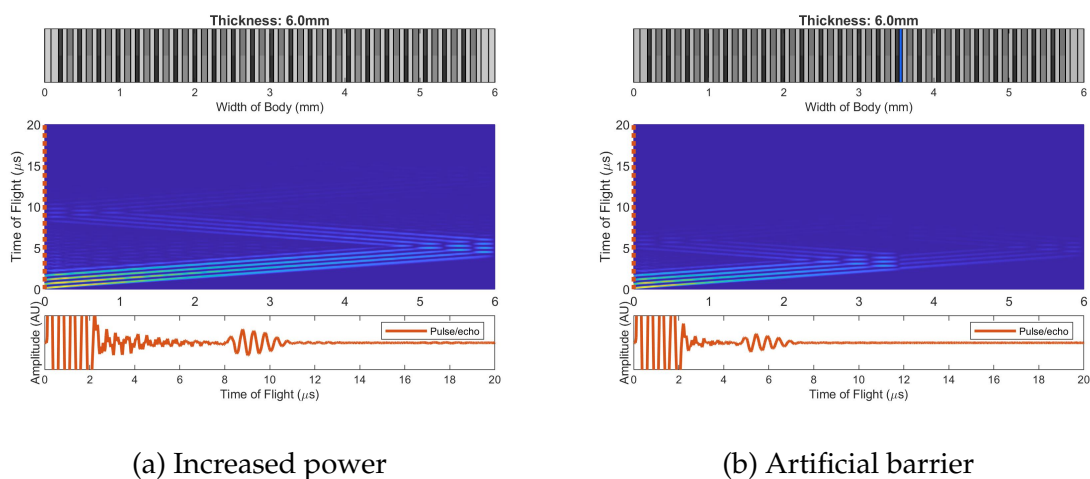
Figure 6.7: a) Result of increased pulse power, reflection now visible at approximately 8-10µs, b) result of including wave barrier, reflection now visible approximately 5-7µs.

An alternative to this could be the insertion, at manufacturing stage, of a wave barrier to force a reflection to the sensing edge early. In the model in Figure 6.7b the barrier is inserted arbitrarily at a depth of approximately 60% into the cell away from the sensor. The barrier has a thickness of 50µm and a speed of sound property of 400m/s, it is shown in the top battery layout plot in pale blue. Notice the collection of peaks present between 5-7µs earlier than reflections in Figure 6.7a of 8-10µs, but strong enough from which measurements could be taken. This is with no more power through the pulse than that in Figure 6.6a. This shows, that at the design and manufacturing stage, the

insertion of some sort of acoustic wave barrier could help in the simple, low cost ultrasonic monitoring of battery cells.

The modelling contained in this discussion provided the motivation to build an amplifier into the test kit for the large capacity cell tests in Section 6.7. In initial sensor tests the standard pulsing configuration would not produce any signal response. Using the modelling to calculate the expected timing of the half reflection confirmed the half space was not present in the cell and as such a more powerful signal would be required to reach the far side of the larger width cell and back to the sensor again. It was confirmed in subsequent discussions that the assumption was correct and that the large capacity cells were of layered construction rather than jelly roll.

6.5 Smart Peak Selection

The following section uses frequency domain methods to monitor where in the signal peaks are changing with respect to two charge reference points. This allows for feed back as to which peaks are preferred when taking battery state of charge measurements. This technique guides away from peaks that correlate poorly with charge cycling and is suitable for automating the measuring process should cell properties change, either through cell discrepancy or with degradation over time.

6.5.1 Cross Wavelet Transform

In the current literature, analysis has almost exclusively focused on ultrasound signals in the time domain, with little regarding the effects of battery changes on the signal in the frequency domain. Gold et al., compare wavelengths of the second compressional wave to the charge of the battery which showed wavelength and amplitude were a function of charge[51]. Apart from this all studies focus on the signal power (the area under the curve of the signal), peak amplitude, or peak time of flight change.

Various methods are tried here to identify if information from the frequency domain can aid in determining parts of the waveform that have strongest correlations with change in battery SoC.

- A fast Fourier transform (FFT) will provide signal information in the frequency domain at the expense of losing all time-based information.

84

- The short-time Fourier transform (STFT) technique is a time-frequency analysis and can help identify not only changes in frequency but also where in the time domain these changes occur. This method has been previously used in attempts to detect acoustic echoes embedded in a signal response through layered bodies[60]. The STFT method suffers from a necessary comprise between good time/frequency resolution.

- A method that somewhat eliminates this time/frequency accuracy trade-off is a continuous wavelet transform (CWT) which has also been used to detect echoes in multilayered structures[61].

Experimental data time/frequency plots transformed using a CWT are shown in Figure 6.8a (charged) and Figure 6.8b (discharged). These plots show the amplitude across the frequency spectrum (y-axis) and along the waveform duration (x-axis), with yellow being high amplitude and blue being low amplitude. Activity is observed across a broad range of frequencies, with concentration around a 2MHz frequency band by around 6μs before attenuating by approximately 10μs, this region would be expected to be the location of the first reflections. The greyed regions denote the cone of influence (COI), a feature of wavelet transforms that causes lower frequency bands to have increased edge effects and must be disregarded.

The battery ultrasound measurements rely on change in signal (ToF/amplitude) rather than an absolute measurement value (i.e. variation in ultrasonic response are observed as a battery feature, such as charge changes). As such, a useful tool to use to monitor these changes in the time/frequency domain is the cross wavelet transform (XWT). This method was developed by Grinsted et al., originally to monitor the Arctic oscillation being a key aspect of climate variance in the Northern Hemisphere[62], but can be applied to any two sets of time series data. A XWT plot is shown in Figure 6.8c, regions in the time/frequency domain that share high common signal power properties are denoted as high intensity (yellow), the arrows show the phase changes with right arrows showing in-phase, left arrows anti-phase, down arrows charge lead discharged by 90° The black border surrounding certain parts of the plots denoted regions with 5% significance against noise, a feature which is not used in this analysis. The COI is again rendered on the plot showing regions at lower frequencies where insights are to be disregarded

From the XWT shown in Figure 6.8c, a parameter for determining the most accurate
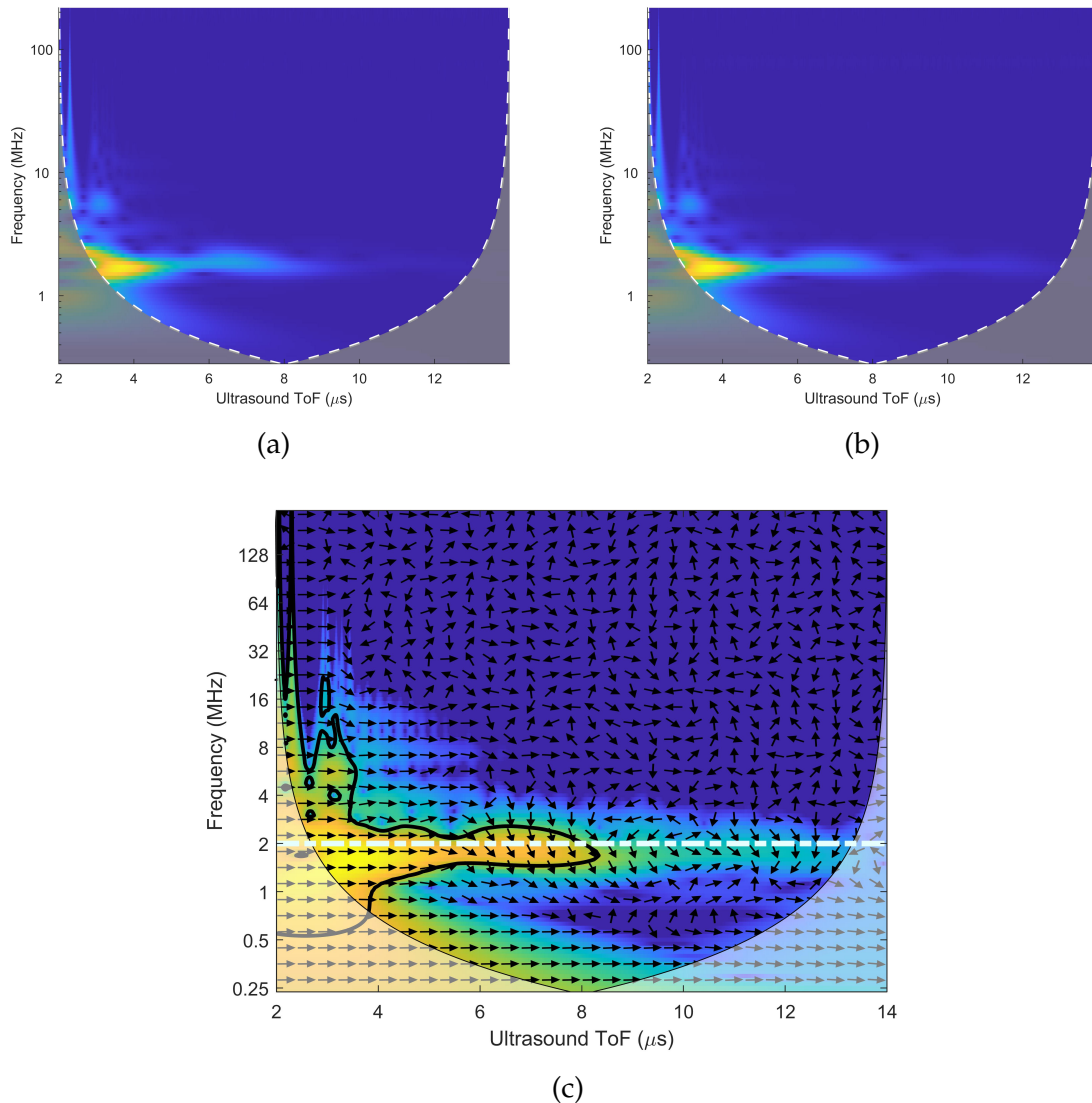
Figure 6.8: a) Continuous wavelet transform (CWT) for the signal when the battery is charged, and b) discharged, c) cross wavelet transform (XWT) showing frequency bands where both signals have strong similarities in amplitude shown in the higher (yellow) intensity regions, arrows mark the phase shift between the signals [arrow right: in phase, left: anti-phase, down: charged leading discharged by 90°][62]

part of the signal from which to take battery charge readings can be obtained. It can be safely assumed that the pulsing frequency is a known value and as such that frequency can be isolated (shown by the dotted white line at 2MHz in Figure 6.8c). Taking the intensity value along this line gives the XWT amplitude plot shown in Figure 6.9a. This is normalised between 0 and 1 and has a large peak at the beginning of the signal at around 3μs. This peak corresponds to the incident pulse and would be of no practical
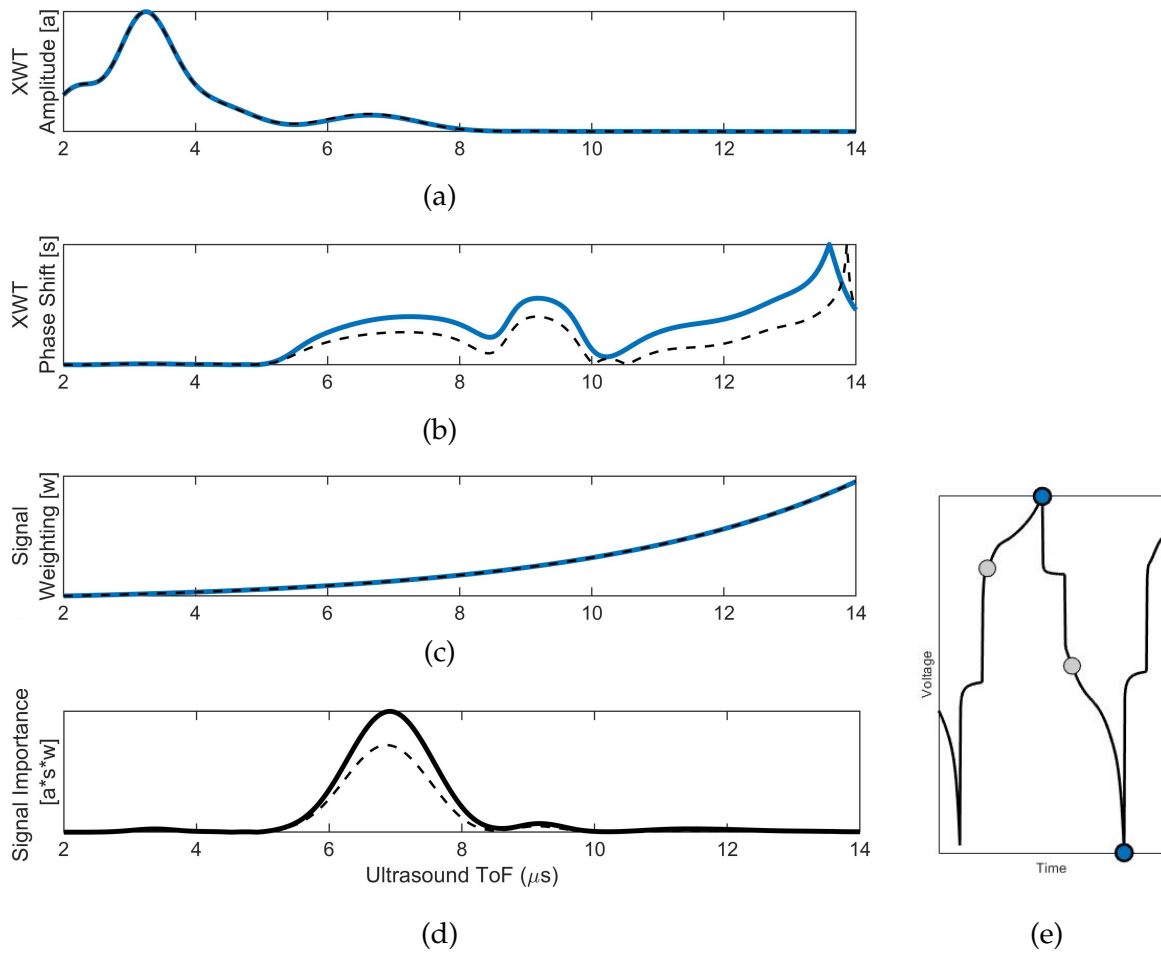
Figure 6.9: Signal importance factor calculation [point E on the flow chart]. Solid lines represent reference taken at charge extremes (blue markers in plot e), dashed lines from reference taken at arbitrary partial charge points (grey markers in plot e).

use. There is however a second peak between 6 and 7µs. The phase shift value in Figure 6.9b captures the phase change which is also normalised between 0 and 1. Here it can be seen that there is little or no shift in phase until around 6µs and then there are fluctuations across the selected frequency after this, growing in intensity and erraticism. In Figure 6.9c, there is an arbitrary, exponential function, providing weighting towards later parts of the signal. The weighting is constructed based on the assumption that later peaks in the signal have travelled further, will include more reflections and therefore hold greater battery insights. This additional parameter also serves the purpose of eliminating or deemphasizing the very early parts of the signal (potentially shallow signal depth penetration, dominated by early layer echoes and often prone to transducer ringdown effects). Finally, in Figure 6.9d, the three values are multiplied to

87

provide a signal importance variable. The variable can guide and potentially automate, based on comparing two signal captures, where to measure peaks to optimise the accuracy of battery charge information. It is important to note that this method works from any two, non-identical, wave captures taken whilst charge cycling. In Figures 6.9a-d the dashed lines represent the arbitrary partial charge points marked in grey in Figure 6.9e. Although the intensity of the signal importance factor is lower, the identification of the most important section of the signal remains clear and accurate.

Figure S.7 is included in the supplementary material where three animations are present. The left panel shown the XWT changing during cycling, changing phase arrows are visible across the 2MHz frequency band. The middle panel contains the signal important factor, when normalised it is shown to provide a stable region from which to take charge measurements. The right hand panel shows the charged A-scans move during charge cycling, using the discharged as a static reference. A state of charge bar is added to the left panel that applies to all three plots.

6.5.2 Smart Peak Selection

Using the XWT to define the signal importance factor enables identification of waveform regions that maximise two conditions; (i) good signal amplitude when at both extremes (or any two non-identical parts) of the charge cycle and (ii) have significant phase shift activity.

In Figure 6.10 the smart peak selection region is shown as peaks on the black line (signal importance factor); this shows a clear maximum between 6 and 8μs. By plotting the time of flight/battery charge correlations (blue line) and the signal amplitude/battery charge correlations (pink line) two points become quite clear. Firstly, the smart peak selection region identifies the waveform region that best correlates with battery charge data and the variation for both charged and discharged states is low (narrow band on the shaded region). Secondly, it confirms that time of flight, rather than amplitude, is a more stable measure to gain battery SoC insights.

Figure 6.11 shows an ultrasound response waveform marked up with all the strategies to suggest from which region to extract measurements. The signal itself is drawn with the regions suggested as containing best battery correlations in a thick black line, the signal is faint and thin elsewhere. Each peak selected for analysis has a marker, the size of which represent the strength of correlation with battery state of charge. The
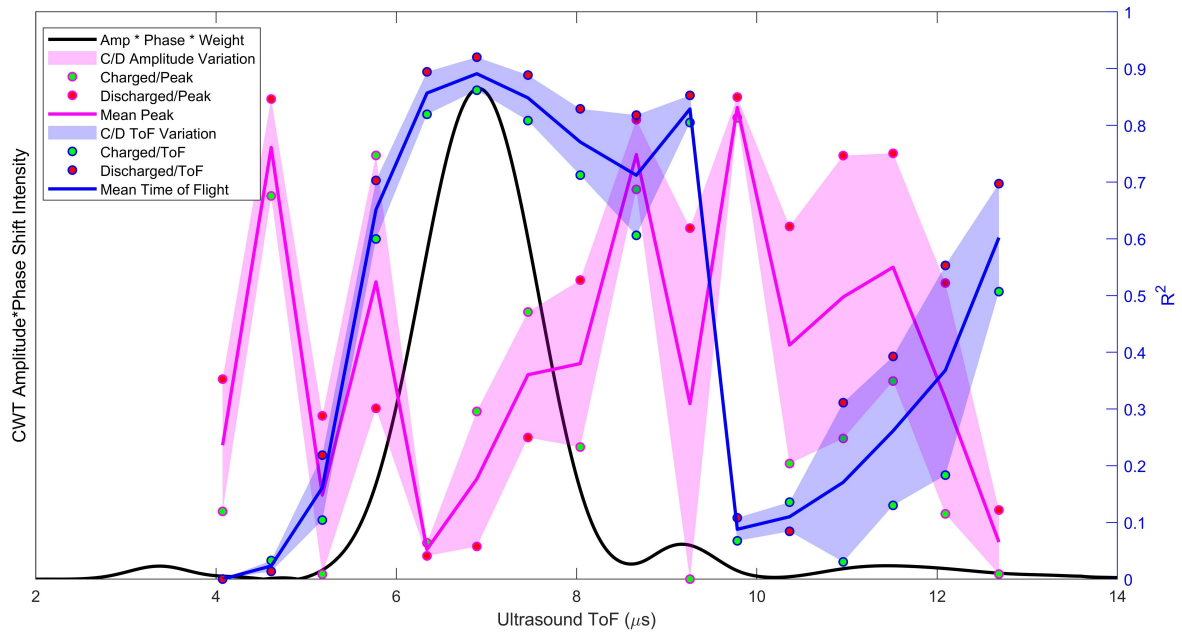
Figure 6.10: Smart peak selection method of locating best region for taking battery measurements [step F on flow chart]. Signal peak amplitude-ToF/battery SoC correlation across the waveform.

deepness of red is used to indicate the discrepancies in correlations between charge and discharge parts of the cycle. This smart peak selection should show large, deep red markers on the peaks of the signal shown drawn with thick black lines. A useful feature of this method of peak selection is that as the XWT amplitude variable detects regions where both signals share high common power, disappearing peaks of interest are automatically filtered out. This helps to guard automatically against unstable recordings.

The point on the peak at around 7μs is large and deep red. This can be seen in Figure 6.10, where the ToF/battery SoC R^2 values during both charging and discharging are 0.86 and 0.92 respectively. The point at the peak at around 11μs is small and almost white, this can be seen in Figure 6.10 where the ToF/battery SoC R^2 values whilst charging and discharging are 0.03 and 0.31 respectively and would be unsuitable for battery monitoring purposes.

Many signals produce a noticeable collection of peaks that represent the first reflection waves that have travelled there and back through the battery. This is an intuitive place to take measurements from and are appropriate to capture signal envelopes, however some signal responses do not provide this. The signals in Figure 6.12 are taken from
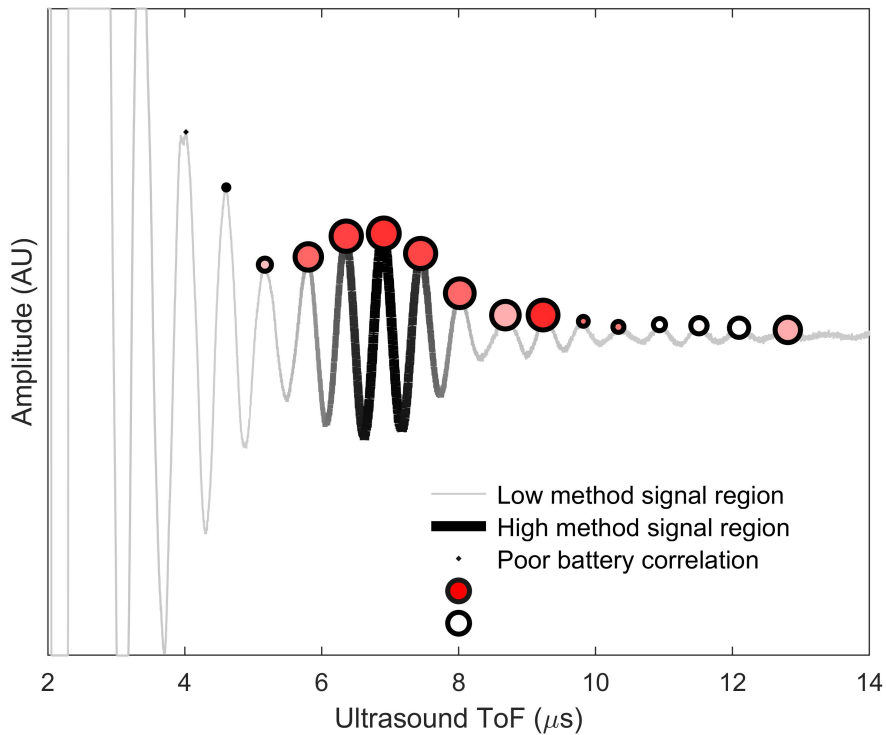
Figure 6.11: Smart peak selection waveform mark up. The ultrasound response waveform is displayed with thick black lines to denote regions of signal that are favoured by the smart peak selection method. The size of the point at each peak represent the strength of correlation with battery state of charge (large points are best) and the deepness of the red in those points shows the variance between charge and discharge parts of the cycle (deep red is best). [step G on the flow chart].

batteries of the same specification and manufacture as previous using identical test equipment and methodology. The signal in Figure 6.12a is difficult to envelope and gain a defined peak from which to take measurements. However, here are a collection of peaks that would appear suitable for taking charge measurements. The signal drawn in thick black between 13 and 15μs contains two or three peaks that have strong correlation and low charge/discharge variance.

The signal in Figure 6.12b is lower quality and no obvious peaks are evident with a good signal to noise ratio as good candidates for taking charge measurements. The smart peak method in this case highlights very early (3 to 5μs) signal and these peaks provide poor battery information (the sound wave has not travelled through the cell layers and there appears to some transducer ring down). The second, shorter group of smart selected peaks from 11 to 12μs reveal the region that contains peaks containing

best battery charge correlations. Recall from the modelling data, that early signal is usually dominated by casing and suffers from lack of cell penetration and should be avoided, the second shallow peak would be preferable.
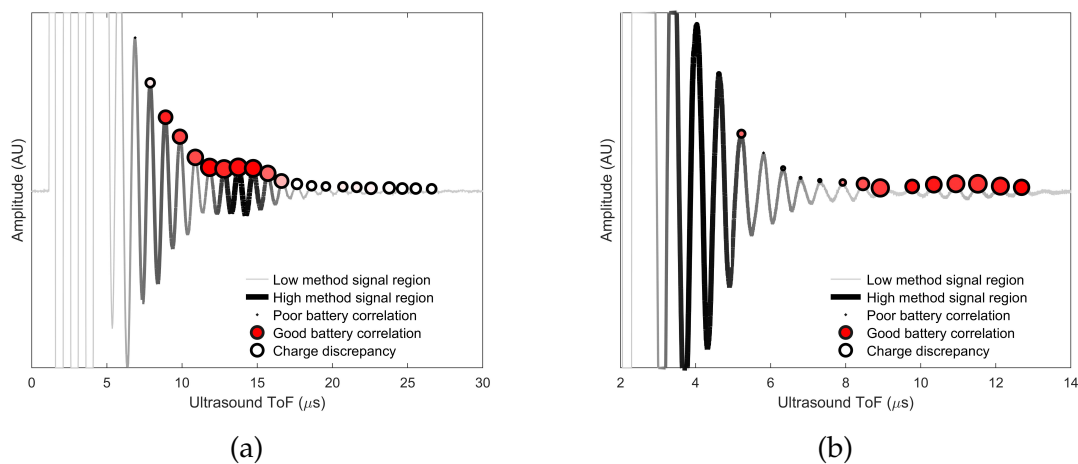
Figure 6.12: a) Signal that is difficult to provide a consistent peak of an envelope, smart peak selection shows that peaks drawn in thick black lines have the strongest battery charge correlations and are most consistent across charge/discharge parts of the cycle. b) This signal has little scope for enveloping, no obvious peak as a candidate for taking measurements, first smart peak region inaccurate, second more shallow region successfully locates peaks with best battery charge correlations.

6.5.3   Combating Potential Sensor Placement Issues

As noted in Section 3.2.4, the spatial resolution of sensor placement can have a significant and damaging effect on the quality of ultrasound signal obtained when pulsing through a cell[48]. It is suggested that the current collecting tab inhibits the expansion of electrode layers where present, and should the sensor be placed over this region it will lead to reductions in peak shift. In addition this, gassing within lithium-ion cells can occur in unpredictable areas causing a reduction in signal quality in the sensing region.

With the cell being a closed body, it is difficult to decide on best sensor placement from visual inspection of a cell. In this work, the sensor was placed as centrally as possible, as seen in the previous section, this generally produced mixed results of varying quality. It is suggested that this smart peak selection method can be utilised to optimise the signal quality where features such as the current collecting tab are encountered or where gassing occurs during battery use or ageing. Whilst this makes no guarantee on

signal quality itself, the smart peak selection will help to ensure that the best signal response with respect to battery SoC is measured, going someway to combating the unknowable and potentially negative effects of sensor placement.

6.5.4   Discussion – Practical Implementation

Ultrasound measurements would likely be used in conjunction with traditional battery measuring methods, such as voltage readings, to enhance the accuracy of charge estimations. The smart peak selection method can help optimise and protect ultrasonic battery measurements, particularly where the signal response is weak or contains unexpected features. Causes of these problems could include variations in battery geometries and sensor instrumentation.

This method of battery monitoring is a practical means of gaining true insights into the internal changes occurring during battery charge cycling. Although this work utilised commercial contact probes to gain ultrasound readings, much smaller instrumentation methods are possible. For example, discs or cut piezoelectric plates, low profile and size order of a few mm's requiring very thin wiring. To ensure responses with good cell penetration additional factors such as adhesion and damping must be considered, this would still allow for a very small and cheap instrumentation set up. Results can be obtained using a single sensor, keeping materials to the minimum required for this method and only one face needs to be accessible. Pulsing/receiving circuits are also small and inexpensive, of the order of £10 s, and with the application of pulse sequencing tables, could control the pulse, signal capture and data processing of all connected battery cells. All the experimental data analysis performed in this study, including peak tracking and smart peak selection requires minimal processing time and power and is suitable for live monitoring purposes. Any improvements in the accuracy of ultrasound data acquisition would improve the accuracy of methods covered in this study.

6.6   Experimental Refinements

This section covers results from testing that are worth noting for future test and analysis reference.

6.6.1 Gel/Glue Couplant

Throughout most of the charge cycling tests in this work, high temperature gel couplant was used in conjunction with hand tightened clamps to maintain pressure and hold sensors in place. Superglue can also be used as ultrasound couplant, the advantage being that of a permanent bond for longer term testing.

A reference test was conducted to compare ultrasonic couplant performance of superglue compared with the high quality signals obtained using gel. Superglue was applied to a 2MHz commercial probe and attached to a standard 2Ah cell as shown in Figure 6.13a. The sensor was applied using firm hand pressure and was held in place for 30 seconds. The concern with this method of attachment is safe removal of the probe for reuse in repeat testing. A superglue de-bonder (Figure 6.13b) was used to remove the sensor from cell surface. With care the sensor could be removed from the cell in perfect condition. The cell after sensor removal is shown in Figure 6.13c.

| (a) | (b) | (c) |
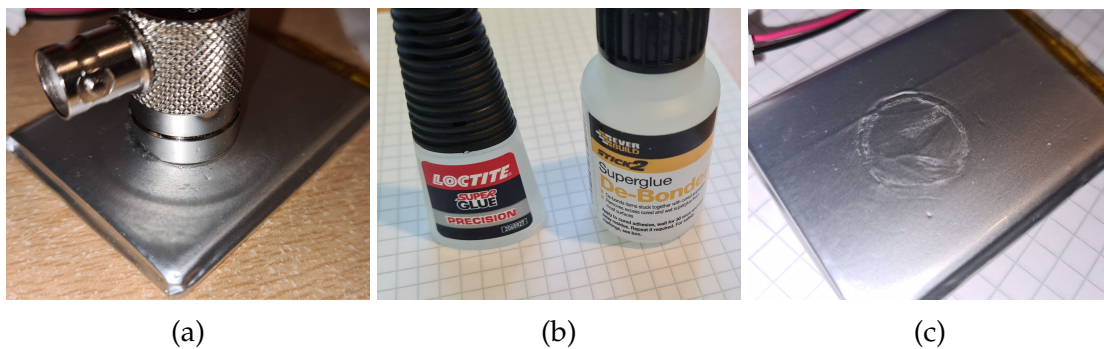
Figure 6.13: Attaching and safely removing a commercial probe to a pouch cell using superglue and superglue de-bonder.

The signal acquired using superglue as couplant is shown in Figure 6.14. The superglue attachment/couplant method is a almost identical to the signal obtained using gel couplant. With the option to safely remove a sensor attached with superglue without damage to the sensor or the battery cell, this semi-permanent attachment/couplant method is to be considered a good long-term attachment method under standard operating conditions. A discussion about the suitability of this bonding method in high temperature conditions is contained in Section 7.4.3.
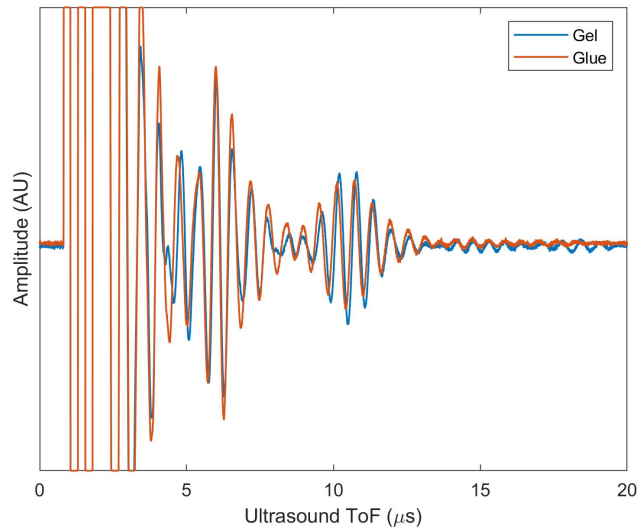
Figure 6.14: Sample signals using different bonding/attachment methods.

6.6.2 Pulse/Echo, Pitch/Catch Through Pulse Comparison

As shown in Figure 2.5 in Section 2.1, there are different sensor configurations measuring the responses of waves taking different paths. In the experiments in this work, single sensor pulse/echo arrangements are almost exclusively employed. For completeness of testing, charge cycling tests were conducting using pulse/echo and pitch/catch, through pulse arrangements to compare. The charge cycling for each test was completed using the Cadex C7200 (shown in Section 5.1), using CCCV charging at 0.5C with a 0.05C cut off. The sensors for the through pulse were positioned on opposing faces of a standard 2Ah commercial cell as shown in Figure 6.15.

The results for the pitch/catch, through pulse test are shown in Figure 6.16a. The first point of note is the absence of excitation pulse at the beginning of the signal, a benefit of this method. There are also signal-to-noise advantages using this method as the wave path is half the distance and attenuates less, that is not evident here, being shown in arbitrary units. The most important result here is the stability of peaks recording high ToF/battery SoC correlations across the whole signal. This is contrasted with the more erratic nature of the pulse/echo correlations shown in Figure 6.16b. It is also worth noting the ToF appears to contain less temperature bias across the signal in the through pulse result, although it still exists.

Whilst the charge/ToF correlations are stable across the whole signal when using a through pulse sensor configuration, if the correct peaks are successfully identified in

94
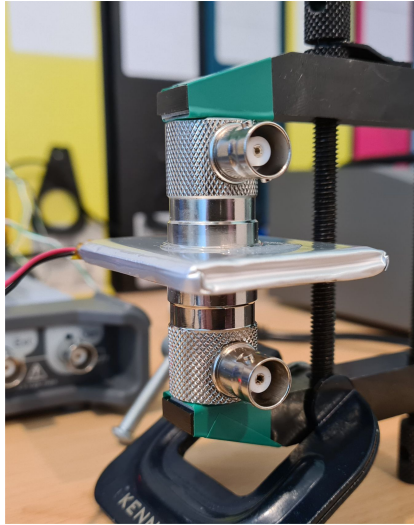
Figure 6.15: Pitch/catch, through pulse sensor configuration.

(a)

(b)
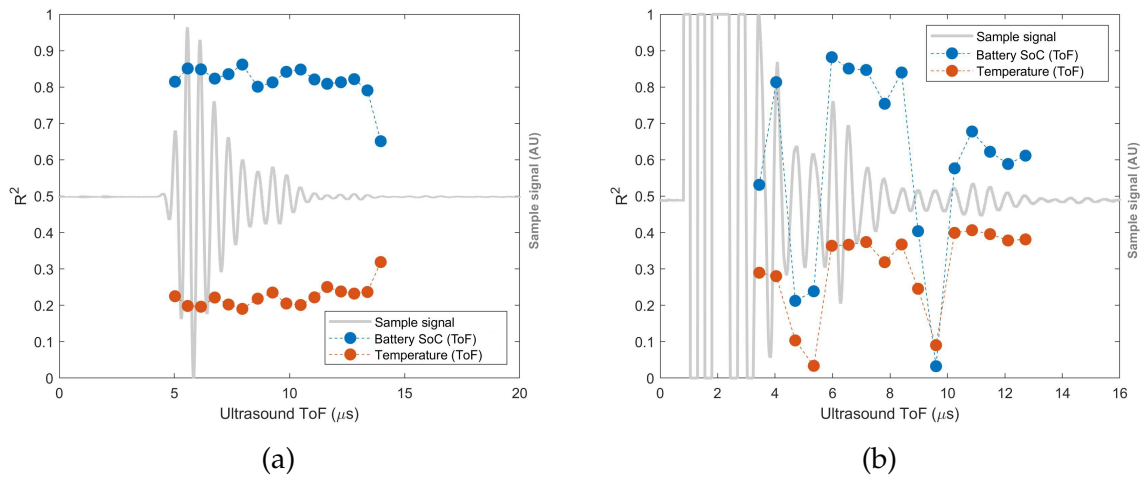
Figure 6.16: Results from charge cycling tests using a) pitch/catch, through pulse and b) pulse/echo sensor configuration. The left axis R^2 refers to the correlations between battery SoC and temperature with the shift in ToF for each peak in the signal response. The markers are overlaid on a greyed out sample signal response to identify each of the tracked peaks.

the pulse/echo signal, the results are of equal quality. In fact, the highest correlation in the pulse/echo test is the 5th peak with an R^2 of 0.88, just over the highest performing peak from the through pulse with an R^2 of 0.86.

The smart peak selection method developed in Section 6.5 is applied to the single sensor, pulse/echo signal, the results of which are shown in Figure 6.17. Recall that regions where the signal is drawn with thickened black lines are the peaks recommended by the smart peak method. The signal is drawn with a black thick line around 6µs, being
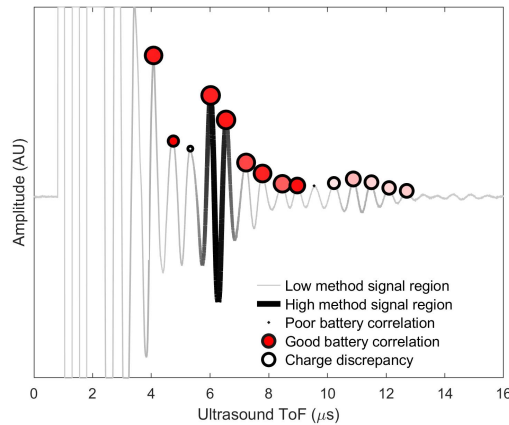
Figure 6.17: Smart peak selection method applied to pulse/echo comparison result.

thin and pale elsewhere. The smart peak successfully identifies the peak(s) with best ToF correlation with battery SoC during charging, noted with the large red dots on peaks in the identified signal region.

6.7   Large Capacity Cell Tests

Ricardo had obtained large, 52Ah high capacity cells to test on using better cycling facilities at the University of Brighton. A suitable test set up was requested to take ultrasonic measurements of the cells during charge cycling tests, the cell is shown alongside the standard cells used during testing in this thesis in Figure 6.18. As shown in this image, the large 52Ah cells were significantly bigger and specifically, thicker than the standard 2Ah commercial cells used in the majority of tests (11.4mm compared to 5.9mm). Testing on a cell of this size was considered important as a verification of the ultrasonic method of layer inspection at larger scale.

Working with a cell of this size presented new challenges. The increase in thickness was a problem for the standard test set up. First attempts were unable to retrieve any signal response from the large cell using a single sensor in pulse/echo configuration. Difficulties in retrieving a response signal were increased as it became apparent using signal amplification there was no centre space/current collector around the middle of the cell to provide a half-reflection, covered in Section 6.4.

Considering these challenges, signal amplification combined with a move to a pitch/-catch, through pulse (covered in Section 6.6.2) set up using commercial probes was

Figure 6.18: Comparison of various capacity cells used during testing.

used. This strategy would ensure retrieval of high quality ultrasound measurements of the large capacity cells, comparable with those obtained from testing on standard commercial cells during this work. To facilitate multiple sensors across the surface to test positional variability, a multiplexer was included in the test equipment set up, providing up to 16 channels. 10 probes were supplied with the test kit allowing for the placement of 5 sensor pairs on the cell. The test kit set up schematic supplied to Ricardo is shown in Figure 6.19. Note the sensor attachment/bonding method recommended in the bottom right corner is superglue, a discussion of this attachment method is covered in Section 6.6.1.

With the ultrasound testing kit delivered to the University of Brighton. In conjunction with Ricardo, the large capacity cells were instrumented according to the set up schematic. The chosen sensor pairing positions are shown in Figure 6.20, a sensor is placed on the opposing face directly inline with each sensor shown to capture through pulse signals.

The cells were subjected to standard charge cycles, at two different rates, 0.5C and 1.5C. Cell surface temperature was also recorded during tests. Results from a sample 0.5C test are shown in Figure 6.21a. Here it can be seen that changes in ultrasound ToF had very strong correlations with battery SoC during charging with $R^2 \approx 0.94$. ToF had a weak relationship with cell temperature with $R^2 \approx 0.38$. These results are inline with those obtained during tests on the standard 2Ah commercial cells shown
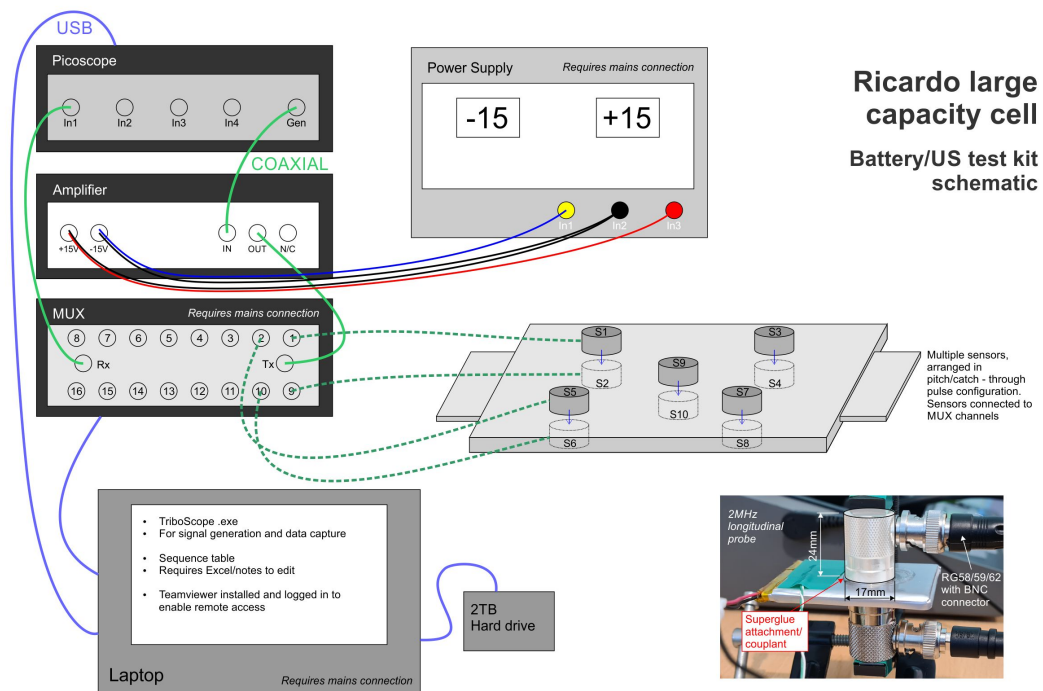
Figure 6.19: High power, multi-sensor, large capacity cell test schematic.
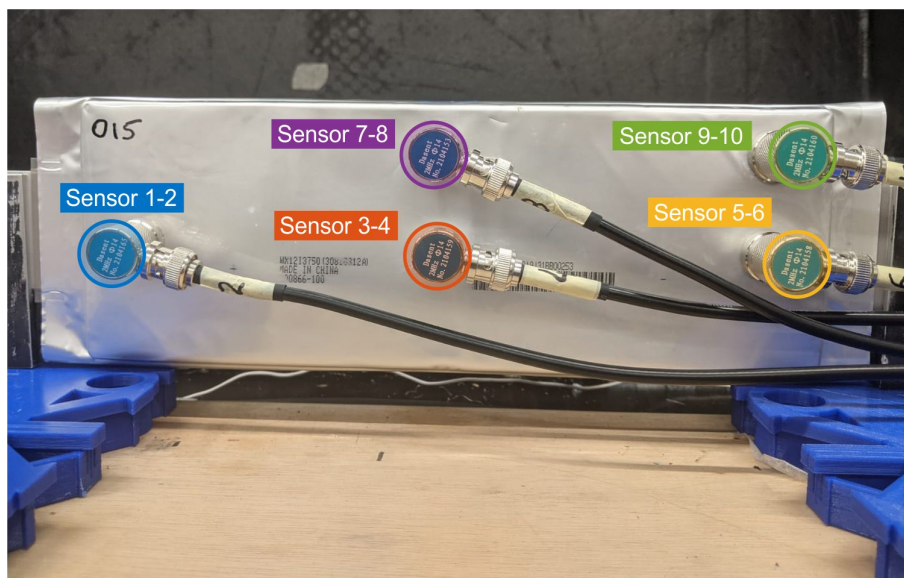
Figure 6.20: Instrumentation of large capacity cell.

in Figure 6.3b. Additionally, there is no requirement for a peak selection method when using pitch/catch through pulse sensing. The red and blue shaded boxes show the narrow deviation (95% CI) in results with the line drawn to show the mean across all selected peaks, this sensor configuration benefit is discussed in Section 6.6.2. There

98

is no obvious discrepancy between any of the sensor positions despite the significant differences in positions across the large cell surface area.
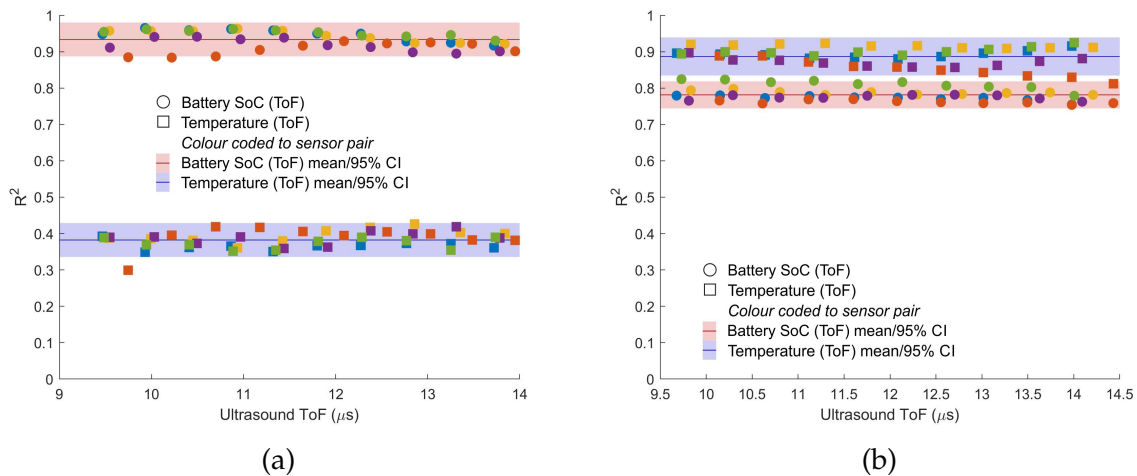
Figure 6.21: Results from large capacity cell tests; a) 0.5C charge rate producing 6°C gain during charge cycling and b) 1.5C charge rate producing a 24°C gain during charge cycling.

As shown in Figure 6.4, modelling showed where the temperature fluctuation of a cell is large enough, the ultrasound ToF will shift bias away from SoC correlation towards temperature correlation. In the modelled example, a 5°C gain during cycling produced heavy ToF bias towards SoC where the 25°C gain shifted bias towards temperature correlation. This effect is shown in the 1.5C charge rate tests that produced a 24°C shift in temperatures across a charge cycle, compared to just 6°C during the 0.5C charge cycle. Figure 6.21b shows a battery SoC/ToF relationship drop in the 1.5C test to $R^2 \approx 0.78$ whilst the temperature/ToF relationship increased dramatically to $R^2 \approx 0.89$. This issue presents significant challenges to the use of ultrasound where elevated charge rates are used.

Based on the assumption that changes in ToF whilst the cell is at rest can only be temperature related (usually the cell returning to room temperature), attempts to combat the effects of temperature on ultrasound signal are made. Whilst this assumption may not fully hold, chemical activity may continue once current is no longer applied, change in material stiffness for example. It was considered worth calibrating the peak ToF measurements using 'resting' cell data based on temperature changes.

The calibrated time of flight is calculated as follows:

$$ToF_c = (\alpha[\beta - T_m]) + ToF_m \tag{6.1}$$

Where β is a temperature benchmark the ToF is normalised to, usually the test start temperature. T_m is the temperature measurement over the test and ToF_m is the measured time of flight of a selected peak during the test. The calibration coefficient α is calculated using:

$$\alpha = \frac{\Delta ToF_r}{\Delta T_r} \tag{6.2}$$

Where ToF_r and T_r are the time of flight and temperature measurements over the calibration region shown in Figure 6.22a, providing a µs/°C value to adjust the signal.
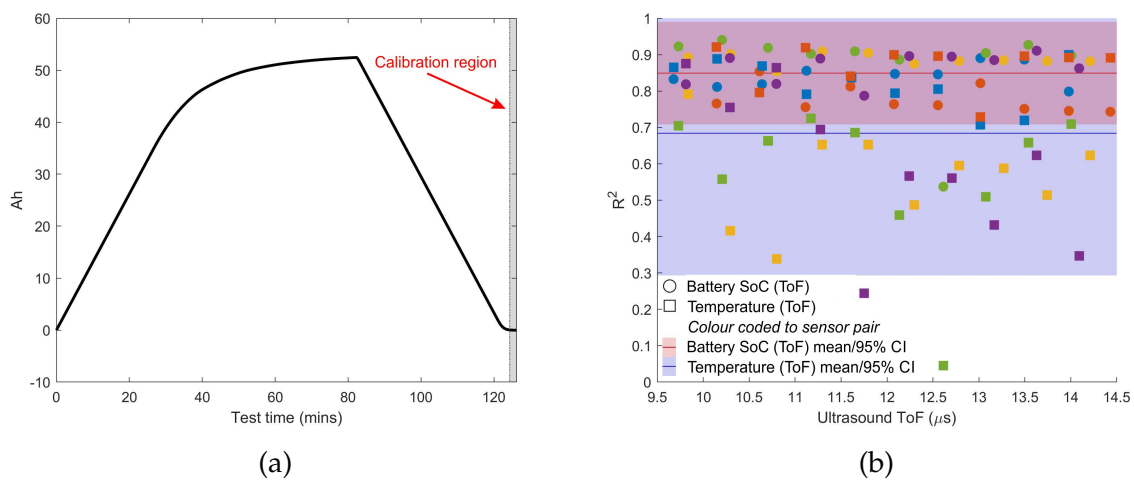
Figure 6.22: Calibrated 1.5C-rate test results; a) calibration data selection region, b) calibrated ToF/SoC correlations.

The results of the calibration are shown in Figure 6.22b. Calibration improved the signal the ToF/battery SoC correlation, increasing the mean from $R^2 \approx 0.78$ to $R^2 \approx 0.85$. It should be noted that the confidence drops with a broad 95% band shown in the red shaded region, it remains true however that there is some improvement after calibration. Conversely, the temperature relationship is severely damaged after calibration. The uncalibrated $R^2 \approx 0.89$ drops below 0.7 after calibration is applied. The confidence region becomes very large once calibrated with a very high spread of results across sensors and peaks.

ToF sees an improvement in the relationship with battery SoC during cycling, despite some loss of confidence in accuracy, whilst the stability of the ToF/temperature relationship is broken. This calibration effect is performed using only a very small region of rest data available from these tests. It is believed that complex reflections in pulse/e-

cho obtained data renders this calibration method ineffective. To explore this further, pitch/catch through pulse ultrasound data should be obtained where the signal takes a more direct path and the temperature effects are evenly spread. Charge cycling programs should be designed to allow for the harvesting of larger quantities of battery rest/thermal change data to acquire more accurate calibration coefficients. This would also help test the linearity of the μs/°C assumption and whether other factors would require incorporation into calibration method, such as stiffening and relaxing of active materials post charge/discharge.

6.8   Peak Variations

Noting the significant discrepancy in the quality of battery estimations across peaks in a signal response, particularly when using a single sensor pulse/echo arrangement, this section takes a closer look at those differences. There are two main reasons for looking at the variations in peak activity; firstly, to see if there may be any method of explaining the differences and secondly, whether any peaks share features and what additional insights may be gained in noting these common characteristics.
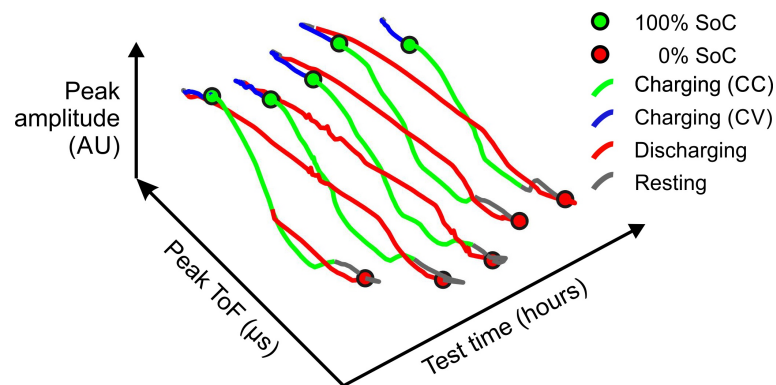
Figure 6.23: Peak tracking throughout charge cycling tests. The lines represent the selected peak ToF shift (μs) and change in amplitude (AU) of the ultrasound signal as the cell is charged/discharged (5 charge cycles in this instance). The green dots mark points where the battery reached 100% SoC, the red dots mark 0% SoC.

Removing the signal surface plot from the peak tracking plots shown in Figures 5.7c & d provides an illustration of the repeating looped characteristics of a selected peak during charge cycling, as shown in Figure 6.23. Rotating isolated peak tracking plots so that test time is flattened, overlays each charge cycle, giving an opportunity to compare the features of changes in individual signal peaks across the signal. This is shown in

Figure 6.24, to aid the comparisons, sketches are drawn to summarise the repeating patterns provided by the selected peaks.
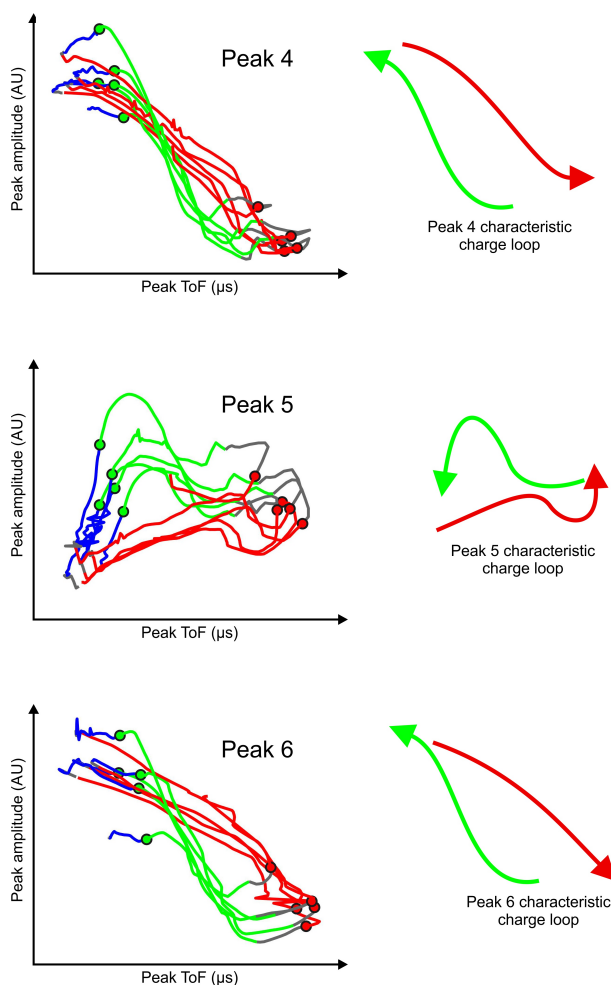
Figure 6.24: Peaks 4, 5 and 6 from a signal response are rotated so test time in hours is flattened to the page showing each peak change loop throughout charge cycling appear overlaid. A sketch of the characteristics of charge/discharge stages of cycling are shown for easy peak comparison. The loop shape correlations are displayed in the boxes, colour coded as shades through red: positive, green: no correlation, blue: negative. This is covered in more detail in later figures.

To assess the features across the whole signal response, individual peak characteristics from the signal shown in Figure 6.16b are displayed in Figure 6.25a. Each plot is colour coded according to the charge state (green = charging[CC], red = discharging, blue = charging[CV], grey = rest). Green markers are placed at the points where the cell was fully charged to 100% and red markers placed where the cell was completely discharged to 0% in the same manner as established above.

The variety of characteristic peak activity is confirmed here with various shapes drawn out with peak tracking. Some peaks form loops (peaks 3 and 7 for example), others have more direct 'to and fro' shapes (peaks 4 and 8) while others have more chaotic natures (peaks 12 and 16). In most cases the green and red markers are consistent within the loops, showing the ultrasound is successfully tracking the cycling nature of the cell during charge. The more erratic markers are found in later peaks in the signal.
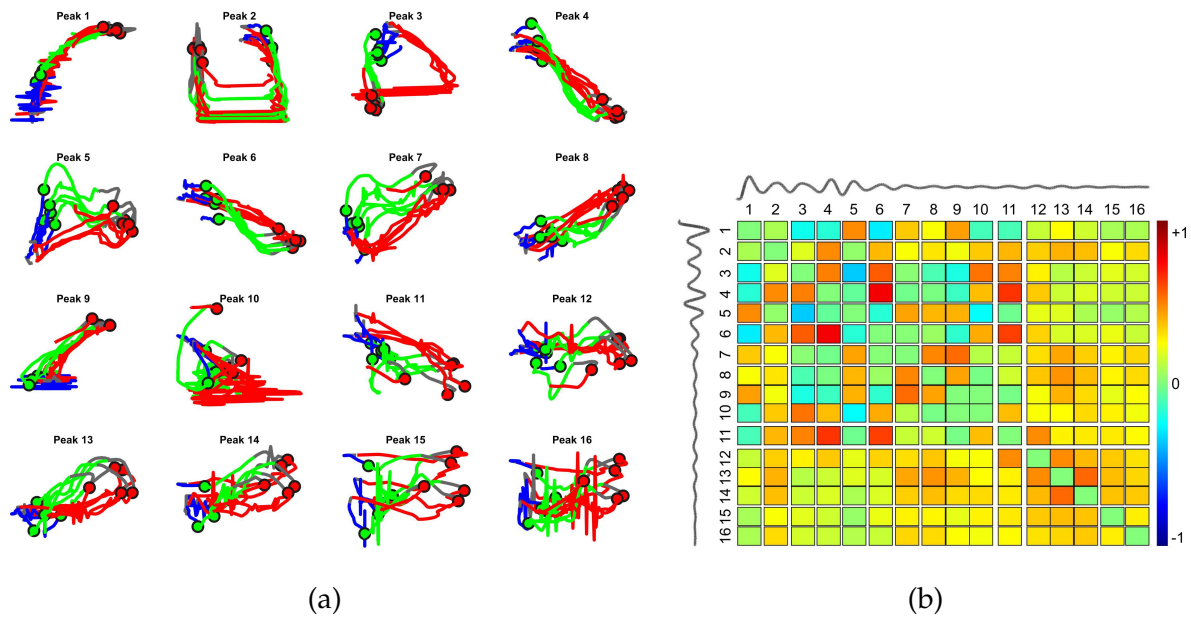
Figure 6.25: Multiple peak tracking, peak characterisation during charge cycling in a single sensor, pulse/echo test set up; a) individual tracked peak activity, colour coded according to charge status (green = charging[CC], red = discharging, blue = charging[CV], grey = rest). b) peak activity correlation intensity plot showing peaks sharing common shapes. Sample waves shown across the top and left hand side with each peak number coded.

To directly compare the characteristic loops of each peak across the signal, an automation of the sketches in Figure 6.24 is conducted using the same methodology developed to study fretting loops by Wade et al. [63]. Using this method the vectors between data points are measured and combined to provide an array variable for each peak, each of these variables can be tested against each other to form a correlation matrix. The intensity of these relationship between these peak characteristic variables are shown in Figure 6.25b, the bar on the right display the color scale where red is perfect positive correlation (+1), blue is perfect negative correlation (-1) and green is no correlation (0). A sample of the wave form is synchronised and plot across the top and left hand axis, each tracked peak is identified with a number to aid comparisons.

The red box for peaks 4 and 6 indicated a strong correlation between the activity of

103

these two peaks during charge cycling. This is confirmed checking the characteristics of each in Figure 6.25a where both peaks have a clear *to and fro* pattern, with a slight hysteresis on the charge stage of the cycle. Peak 11 is also identified as similar to peaks 4 and 6, where the resemblance is apparent although not as strong. The periodicity of peaks 6 and 11 from the start, identified as close in nature to peak 4 is worth noting. It could be that the resemblance of peak activity here is significant, possibly due to half reflections giving attenuated versions of the same peak. There is also a band shaded in orange (approximately 0.4 correlation) apparent at peak 2, around peaks 7 and 8 and again around peak 13. The periodicity may also giving clues as to half reflections and with some calculations, average wave speed through the cell.

Tracking of multiple peaks is performed on the pitch/catch, through pulse test shown in Figure 6.16a. In this test it was noted that through pulse signals are more stable at attaining high correlations with battery charge during cycling, having good correlation across all peaks. This peak consistency is clearly visible when viewing the peak characteristics across the signal in Figure 6.26a, with little discrepancy in the nature of peak activity.

(a)   (b)
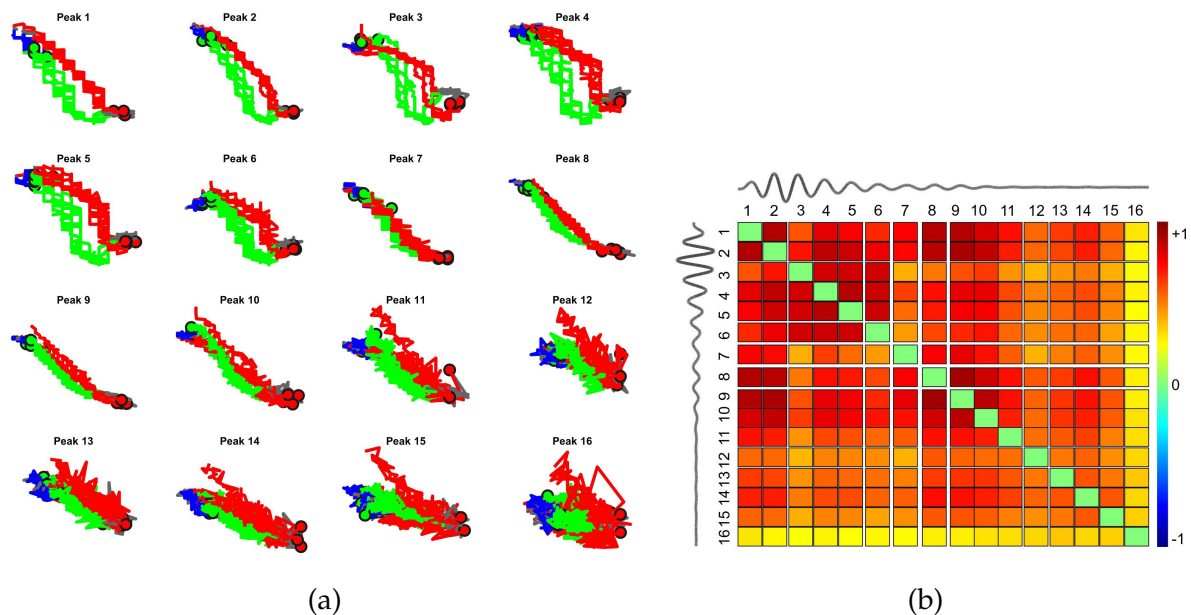
Figure 6.26: Multiple peak tracking, peak characterisation during charge cycling in a two sensor, pitch/catch, through pulse test set up; a) individual tracked peak activity, colour coded according to charge status (green = charging[CC], red = discharging, blue = charging[CV], grey = rest). b) peak activity correlation intensity plot showing peaks sharing common shapes. Sample waves shown across the top and left hand side with each peak number coded.

This consistent peak tracking is confirmed in the correlation intensity plot shown in

Figure 6.26b. It appears that there are repeating bands of high intensity regions, marking out the periodicity of peaks sharing common peak tracking characteristics. Bands of increased intensity form at peaks 1-2, 4-5, 8-10 and 13-14. This could suggest half or full reflections at these peaks, where the waves are attenuated repeats of the same wave paths.

This method of peak analysis was not explored in great detail, being an initial exploration to see whether a) peaks could be characterised according the their 'shape' during charge cycling, and b) whether these shapes could be compared and contrasted to provide insight locked withing the wave responses.

This addition to the analysis script was considered moderately successful, with some potential for further exploration. As discussed, parameterising the 'looped' activity of the peaks can allow for comparisons, repeating patterns maybe capable of providing insights into the layered structure of the cell. Further to this, a template could be set, such as the desirable 'to and fro' nature found in peak 9 in Figure 6.16a. A search could be performed in the background to take readings from peaks matching the template, giving confidence other factors causing hysteresis (such as temperature effects resulting in ultrasound discrepancies) are eliminated. Deviations from observed peaks characteristics may be a sensitive method of assessing a change in battery structure, through abuse or ageing.

6.9   Conclusions

- Time of flight measurements show better correlations with battery state of charge when compared to the signal amplitude.

- Instrumentation variations such as sensor and bonding methods, in addition to variations in the layered construction of a cell, can results in unpredictable signal responses when pulsing through a lithium-ion battery. This can be problematic for some measuring/analysis techniques, such as signal enveloping which may be difficult or impossible to obtain.

- Smart peak selection provides a method of locating the peak with strongest correlation with battery charge. This method is not required when using two sensors in through-pulse configuration but is a useful tool for pulse/echo sensor set ups. The method is shown to work on various signal responses, successfully identify-

ing a region of peaks carrying good battery state of charge information.

- Temperature effects can interfere with the ability to monitor state of charge using ultrasound responses. Temperature effects can occur from internal fluctuations during elevated C-rate charging or externally from ambient temperature changes. Temperature can dominate the signal at high enough temperatures, causing a temperature bias. At lower temperatures, the signal has a charge bias and maintains accurate charge cycling monitoring.

- Method suggested to calibrate signal responses to dampen temperature effects. Trial of the method shows a slight improvement in ultrasound/state of charge correlations, whilst damaging the relationship between temperature and charge. This methodology is attempted using a small amount of rest data, further tests are recommended with larger resting data periods.

- When using a single sensor, peaks do not alter in a uniform manner across the signal. There is an apparent unpredictability regarding how each peak alters during cycling. This is not the case for through pulse signals, where each peak has approximately the same behaviours across the signal. By characterising the shape of peaks during charge cycling, similarities in peak behaviours shows periodicity providing some dimensional insights of the cell.

- Experiments on the large capacity cells agreed with temperature effect modelling in Section 6.3 closely. Both show that charge cycling with small temperature fluctuations ($\approx$ 5 to 6°C gain), produced by a low C-rate charge the signal retain a strong SoC bias. The higher C-rate tests on the large cell cause a 24 to 25°C gain in temperature, this shows an equal temperature/SoC bias in the ultrasound signal in both the large capacity cell test and the modelling.

7 Non-Standard Thermal Abuse Tests

In this chapter, the thermal abuse testing is conducted on the same commercial lithium-ion cells used in SoC tests in section 5.1. Ultrasonic measurements of the cells during thermal abuse tests are analysed to assess whether this method of inspection can provide additional battery cell insights and potential for early warnings of the onset of thermal runaway.

The work in this chapter was undertaken collaboratively with, at the time, PhD student Peter Bugryniec. In his previous work Peter had assessed thermal runaway in lithium-ion cells and studied advanced abuse modelling of these thermal reactions[64–66]. Peter was responsible for the oven during tests, placing samples inside, connecting the thermocouples, operating the oven and safe sample removal and oven cleaning post tests. All other tasks and procedures in this chapter are within the scope of this thesis.

7.1 Introduction
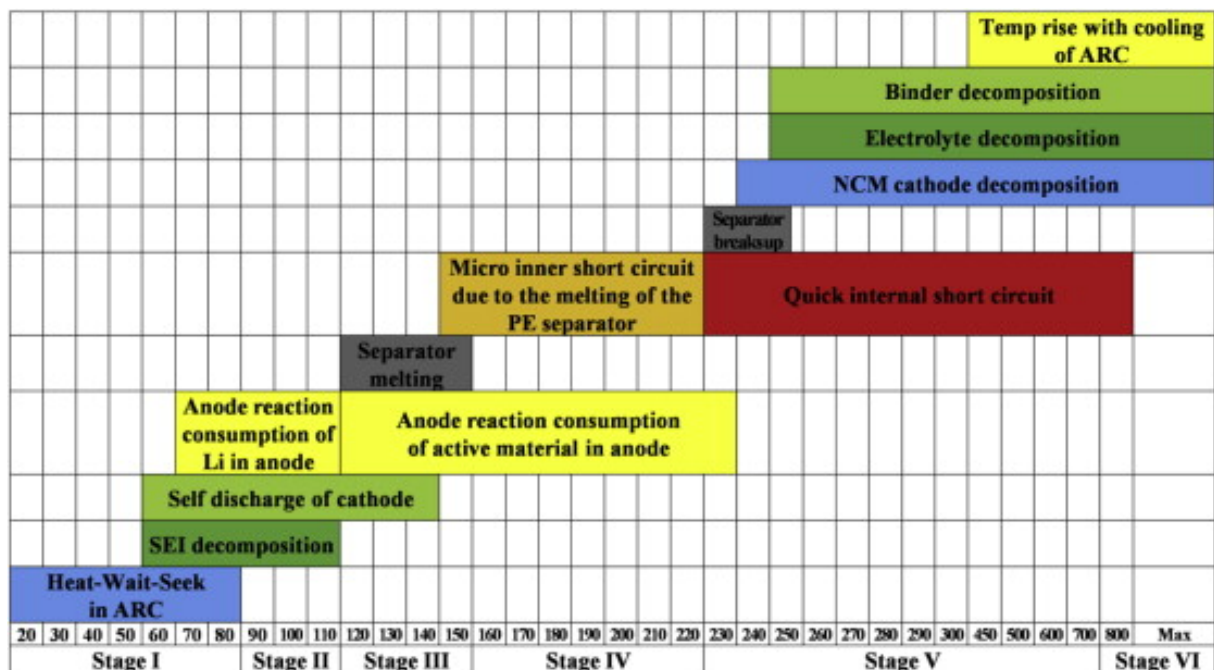
Figure 7.1: Overview of reactions with respect to temperature, Feng et al. (2014)[67].

Thermal runaway (TR) is a significant safety concern for lithium-ion batteries. To investigate thermal runaway, accelerated rate calorimetry (ARC) and oven exposure is

Table 9: Summary of events during thermal abuse tests and expected temperatures/rates.

Feature	Expected value	Reference
Swelling/delamination	40-60°C	[68]
SEI reaction	45°C	[67]
Electrolyte evaporation	60-100°C	[69]
Anode-electrolyte	80°C	[67]
Separator melt (PE/PP)	132°C/163 °C	[67]
Onset of self-heating	0.02-0.1°C min^{-1}	[65]
Thermal runaway	1.0°C min^{-1}	[65]

used [65]. Effects of heating occur in battery cells at certain temperatures, from gassing to thermal runaway. An overview of reactions is shown in Figure 7.1. Table 9 is created summarising key events with expected temperatures for the cell type being tested. The tests were designed to check whether an ultrasound signal response could detect any of these events during cell heating.
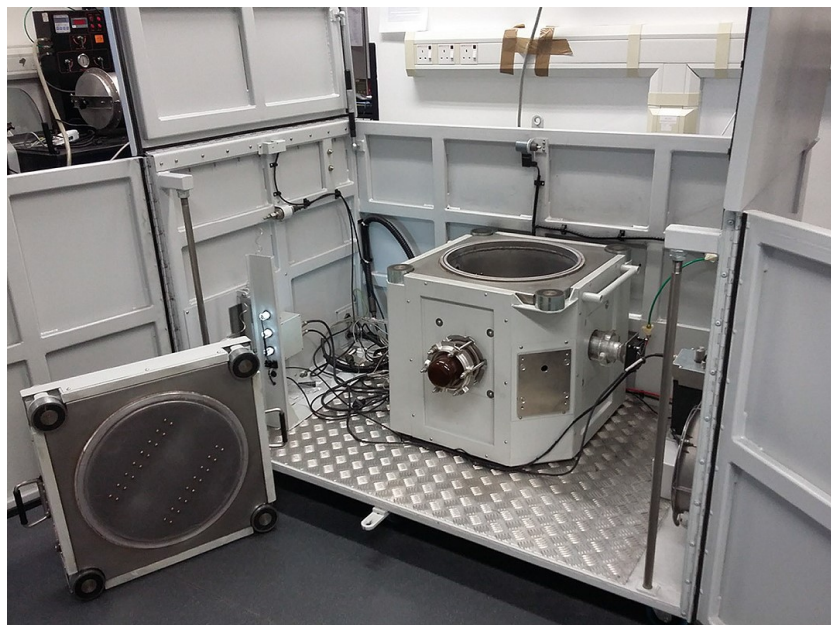
Figure 7.2: Thermal hazard technology ARC EV^{+} [65].

The ultrasonic monitoring equipment used in these tests is the same set up as that used during charge cycling tests in section 5.1, Figure 5.1. However in these tests, as there was expectation of the cell being destroyed should thermal runaway occur, commercial probes were considered unsuitable and the cheaper, disposable option of bonded sensors was initially preferred.

The ARC (Figure 7.2), based in the G28 battery lab in the Kroto Research Institute, University of Sheffield, was used to heat the cell for the test. Two main options were considered for the thermal test parameter, firstly, thermal ramping, in which the cell is heated at constant or in regular stepped fashion. Alternatively heat-wait-seek tests were considered, a test set up designed to monitor the precise onset of self-heating within the cell.

7.2 Phase 1: Initial Exploration Test

The first phase of testing was to conduct thermal ramping of a commercial pouch cell whilst taking ultrasonic measurements. Initially as a means of assessing whether the ultrasound signal response would detect battery changes in general during heating.

7.2.1 Set Up

Commercial probes were rejected in these thermal tests, the ARC would subject the sample cell (the same 2Ah capacity cells used throughout standard charge cycling tests in Chapter 6) and all connected sensors and wiring to high temperatures (over 100°C). This could damage the probe and if thermal runaway were to occur, the probe would be destroyed. Instead, pre-cut circular 3MHz piezo-ceramic elements were obtained, being the closest available to the 2MHz probes used with success in charge cycling tests. These sensors were longitudinal and wraparound, suitable for these tests. The sensor was bonded to the battery surface using Robnor epoxy resin, a coaxial cable was soldered onto the element with the ground wire attached to the wraparound section, shown in Figure 7.3a. A further layer of epoxy was applied to the sensor for added protection, shown in Figure 7.3b.

A type N thermocouple was attached to the surface of the cell, the battery was suspended from the frame that would sit in the ARC to keep the object centrally placed, shown in Figure 7.3c (prior to testing) and Figure 7.3d (after thermal abuse tests). The battery was not specially prepared in anyway and was tested on at approximately half capacity SoC. The cell was not clamped or restricted so any swelling would be allowed to occur.

A thermal ramping test was decided for the ARC to heat the battery cell. The ARC test was designed to heat up to 120°C in steps of 10°C. This test was designed to see firstly,

(a) 3MHz sensor attached to cell

(b) US instrumented pouch cell

(c) Cell in ARC prior to testing

(d) Cell in ARC post thermal abuse test
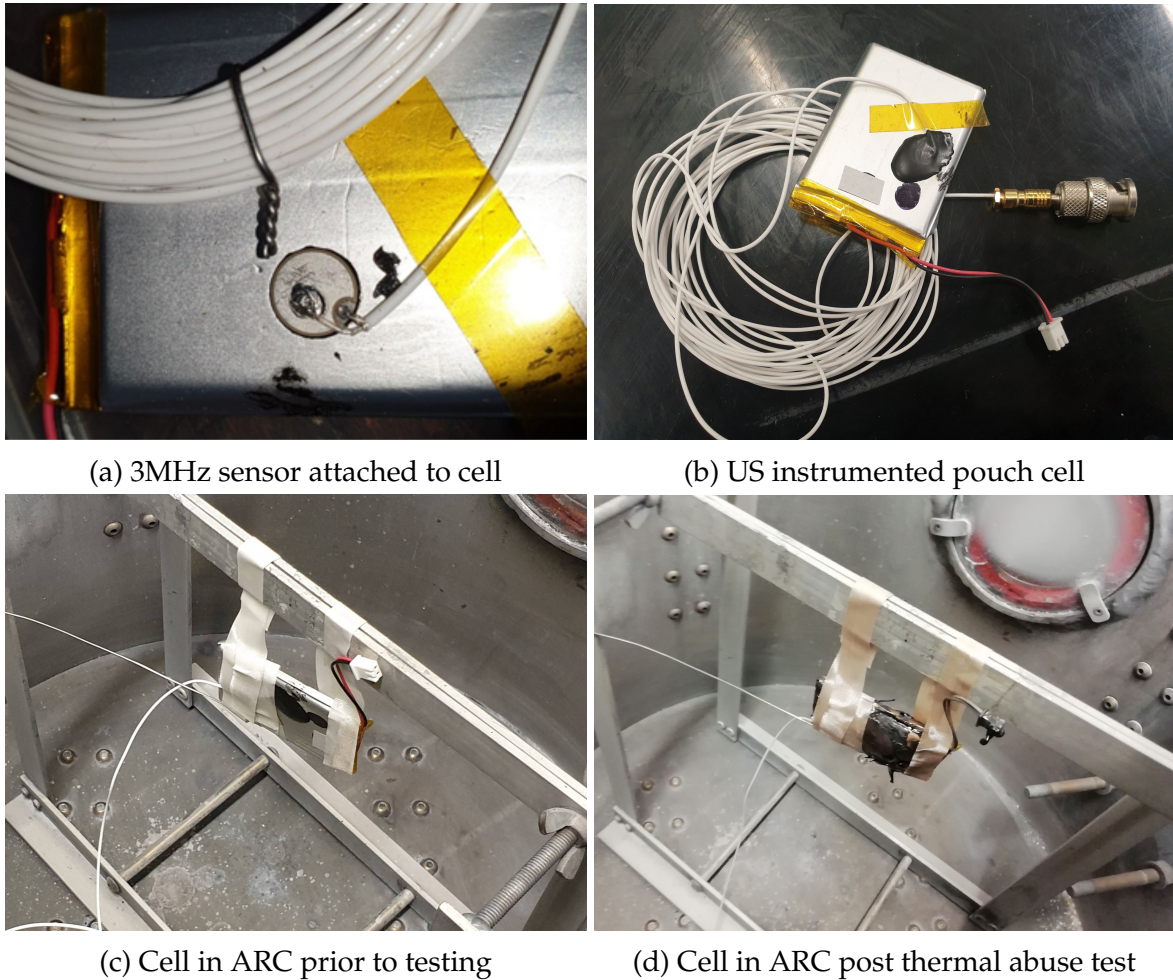
Figure 7.3: Thermal abuse test, sensor instrumentation. Pre and post test, ARC/cell images.

how the ultrasound response from the battery would track the change in temperature and secondly, any deviations from a suspected linear relationship between the two. These deviations would be assumed to be internal changes that could be assigned to expected events within the cell at certain temperatures.

7.2.2 Results and Discussion

The test data was processed using adapted methods developed in section 5.2. A signal peak was selected for tracking throughout the test, the change in signal amplitude and time of flight could then directly be compared with the thermal data to assess the relationship between the two. The peak selected in this instance was at approximately 4µs and is shown in Figure 7.4a. The peak was isolated, tracked and displayed in Figure

7.4b.

(a) Selected peak
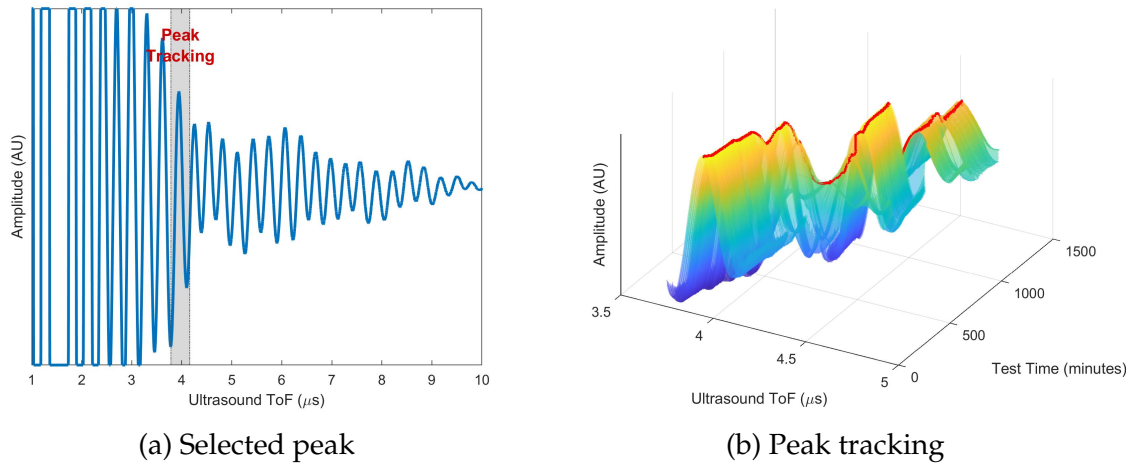
(b) Peak tracking

Figure 7.4: Thermal abuse test, ultrasound signal response.

The peak tracking effectively tracked the peak as the test progressed, this was despite significant shifts towards higher peak timings as the cell was heated (Figure 7.4a - top). The relationship between the ultrasonic signal response and the cell temperature was linear with both the tracked signal peak and the temperature closely matched in their progression, this is shown as the steady red line through the region marked (1) in Figure 7.5a, b & c. The closely matched relationship is clearly evident in the top panel in Figure 7.5b, where the temperature and peak change are almost identical in both timing and scale. This is most obvious in the top correlation plot panel in Figure 7.5c where the relationship is linear up to around 45-47°C.

In Figure 7.5a, there is a temporary 'blurring' of the signal approaching 600 minutes, marked as (2). This could possibly have been due to swelling or gassing, in either case the feature corrected itself as the signal strength returned after around 2 hours. This dip in amplitude is most clearly visible in the bottom panel of Figure 7.5b, marked (2), note the significant drop and return to a stable amplitude for the next few hours. There is a smaller, less noticeable event such as this 'blurring' at around 400 minutes, again the signal corrects itself.

The regions marked (3) are a drastic increase in ToF over the relatively short period where the cell was heated from 55°C to 95°C. The increase in ToF is somewhat greater than expected and features a sudden jump at around 76°C, marked as (6) in Figures 7.5b & c. The purely linear relationship does not hold through this temperature, after this, the ToF appears to remain constant until sharp increases occur.

111
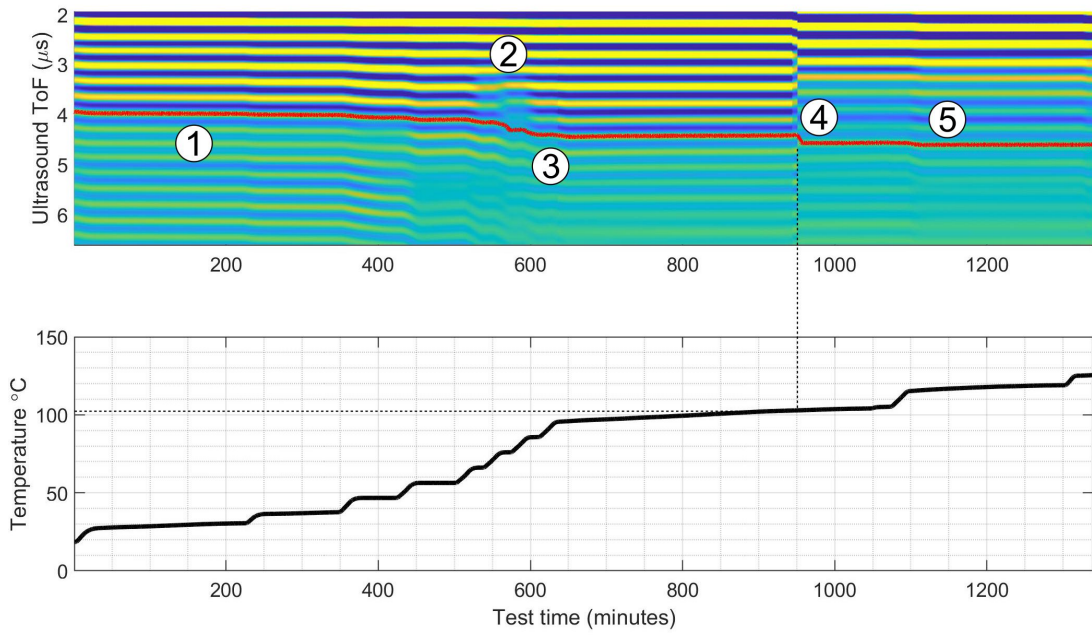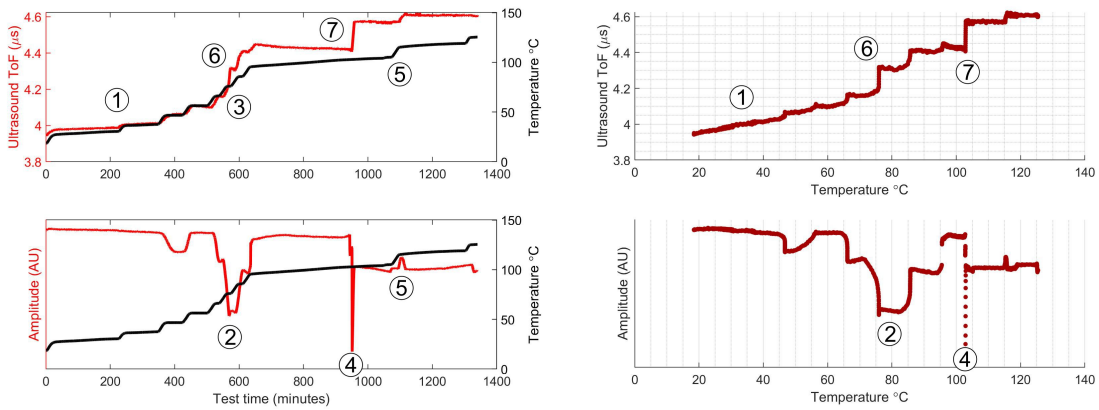
Figure 7.5: Results from initial thermal abuse test. a) peak tracking synchronised with cell temperature, b) ToF/temperature and peak amplitude/temperature comparison plots and c) ToF/temperature and peak amplitude/temperature correlation plots.

There is an abrupt change in signal at approaching 1000 minutes when the cell is approximately 103°C, marked (4) and the dashed lines in Figure 7.5a. This sudden ultrasound feature does not correspond to any thermal characteristic as the temperature is steadily rising for an extended duration when this change occurs. This could be a results of sudden cell changes such as bulging, or a structure change of the polymer separator. It is also possible this was an instrumentation issue, where the sensor

'popped' away from the cell surface slightly due to swelling, causing the altered signal. This 'snap' in signal peak ToF is marked (7), a clear deviation from the linear ToF/temperature relationship, similar in nature to the sudden jump marked (6).

Despite the change in signal, ultrasound continued to track the temperature increases in the battery. Approaching 1100 minutes the cell heats a further 10°C up to approximately 115°C, marked as (5). From the succession of thermal ramping up to midway through the test from 55°C to 95°C, the small increases in temperature do not affect the ToF, only the ramping stages. The ultrasound stopped recording approaching 24 hours into the test and the cell did not go into thermal runaway during this time, likely due to the cell not being charged to full capacity before heating. The cell was heated to the maximum temperature of the ARC on two occasions to force thermal runaway, the damaged cell after the first is shown in Figure 7.3d.

7.2.3   Conclusion

There was little attempt to compare any of the ultrasound features with the values outlined in Table 9 in this initial exploration test. This was due to the lack of repeatability of the test, being a single data set, it would be impossible to know whether a feature, such as the 'blurring' seen midway through the test, occurs regularly or on just this occasion. The inability to decipher what features in the ultrasound response were driven by the changes in the battery sample as it heats, and what is caused by the instrumentation hardware (sensor, bonding, connection, wiring) during heating needed addressing before assumptions could be made. Additionally, the cell did not go into thermal runaway during the test so no prior warnings of this event could be detected.

The test was considered successful however, this initial data analysis revealed that ultrasound would continue to measure changes in temperature during thermal ramping of the cell. There were many features that deviated from a linear relationship between the time of flight of a selected peak and the cell temperature or the constant amplitude measurement of the selected peak.

7.3   Phase 2: Bonded Sensor Tests

In this phase of testing, attempts were made to address the issues presented in the initial battery cell thermal ramp test. The first stage of these tests would be to perform

113

a thermal ramp test on a metal block whilst capturing ultrasound data. Being a single layered object undergoing no changes other than temperature increase, this test would give insight to the effects of the high temperature upon the ultrasound hardware. This in turn would give confidence to the battery tests where cell changes are assumed.

This phase of testing included three repeats of the same parameters. This would provide the repeatability and consistency of results from which fair assumptions and conclusions could be drawn. To increase the chances of setting the cell into thermal runaway, each cell is subject to the heat test whilst fully charged. It was expected testing on the cells in this state would trigger more reactions as the cell temperature increased. In leaving the cell fully charged, each cell was subjected to three discharge/charge cycles from brand new. This process served the purpose of ensuring each cell was in a similar state of health and charge. The ultrasound response was captured throughout each of these cycling tests in the same manner as charge tests in section 6, this would give insight into sensor performance in how accurately the internal changes due to battery charge were measured.

7.3.1 Set Up

The instrumentation calibration tests were performed on a metal block, having a thickness of 9.8mm and a material wave speed of 3984m/s. The sensor attached to the block was a 3MHz longitudinal wraparound sensor, identical to that used in the initial test in section 7.2.1. The sensors were bonded in the same manner using a layer of epoxy resin, the coaxial cable was soldered to the sensor/ground section as shown in Figure 7.6a. A further layer of protective epoxy was applied to the sensor, shown in Figure 7.6b.

The instrumented block was suspended in the ARC in the same manner as the battery cell test as shown in Figure 7.7, the surface temperature of the sample was recorded using a thermocouple. The ultrasound captures were taken using the same equipment and methodology as that used in the charge cycling tests and the initial battery test (Figure 5.1), however, no clamp was used for the sensor as the bonding held the element in place. 3MHz waves were pulsed through the sample, in a pulse/echo, single sensor arrangement. The ARC was set on a thermal ramp test, starting at 50°C, heating the sample in 5°C steps with a wait period of approximately 90 minutes.

Three identical 2Ah cells were used for testing (the same cells as used in Phase 1 in

114

(a)   (b)
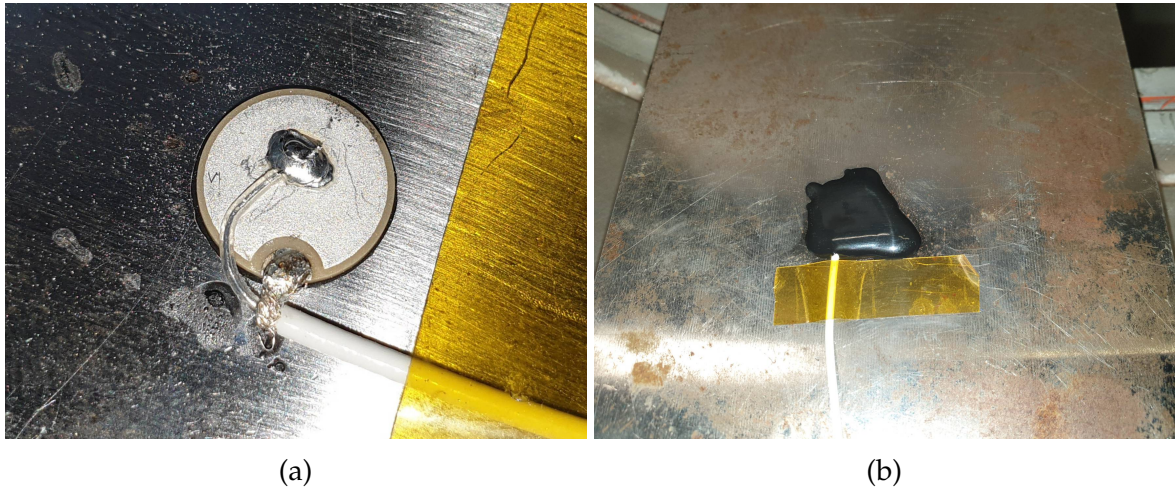
Figure 7.6: Ultrasound instrumentation of metal block, a) circular wraparound element bonded with epoxy, b) covered in epoxy for additional protection.
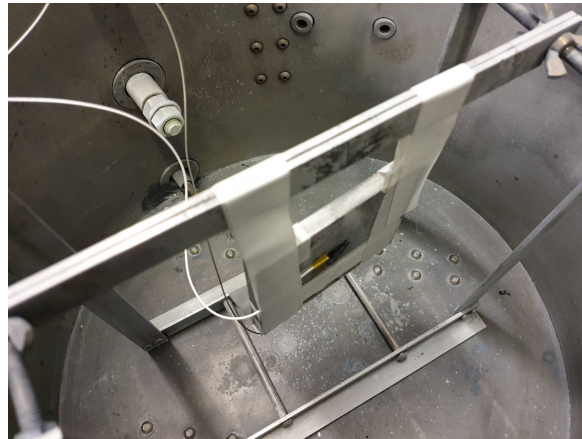
Figure 7.7: Metal block suspended in the ARC.

section 7.2), to ensure test repeatability, all three sensor elements were chosen from the same batch. 10MHz longitudinal wraparound elements were available, with a 3MHz signal in pulse/echo configuration, to be sent through the cells.

The circular piezo-ceramic elements were located at the same position on each cell as shown in Figure 7.8a and each sensor was bonded to the cell using epoxy resin, shown in Figure 7.8b. Coaxial cables were soldered once the elements had been clamped and cured overnight in the same manner as the metal block instrumentation. A further layer of epoxy was applied to the sensors for protection (Figure 7.8c).

Prior to the thermal ramping stage of the test, each cell was charge cycled three times and was left at 100% capacity charge. This process ensured all cells were in an identical
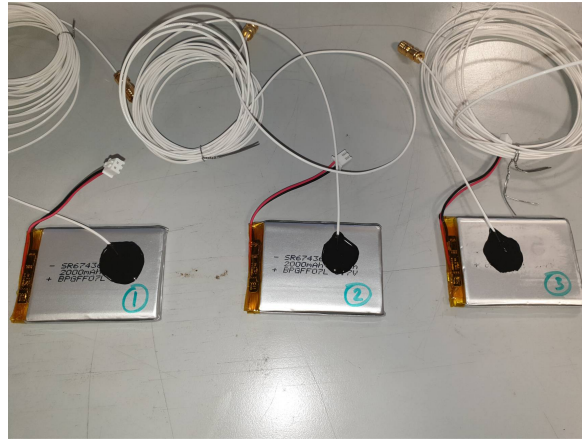
Figure 7.8: Ultrasound instrumentation of three test battery cells, a) elements positioned in same location, b) bonded to cell using epoxy resin and c) additional layer of epoxy for sensor protection.

state and were also more likely to go in to thermal runaway. Additionally, ultrasound measurements were taken during cycling to assess the quality of the signal responses retrieved using this instrumentation method as opposed the commercial probes used throughout Chapter 6. The cells were cycled 24 hours prior to the thermal ramping stage of the test using the MACCOR 4000 Series Test System used throughout charge cycling tests in section 6. The cells were CCCV cycled at 0.5C with a cut off of 0.01C. The cell surface temperature was recorded throughout the charge cycling stage.

For the thermal ramping stage of the test a heat-wait-seek method is utilised to determine the onset of cell reactions. A starting temperature of 50°C was set to 'heat' in

steps of 5°C. Each heat step is followed by a 60 minute 'wait' where the sensitivity of the ARC 'seeks' for a temperature rate of > 0.02°C min^{-1} at which point the onset of self-heating is defined here, whilst a heating rate of > 1.0°C min^{-1} was taken as the cell being in thermal runaway[65].

During the heat stage of the tests, the cell is suspended in the ARC as shown in Figure 7.9. The thermocouple is also attached and protected to the cell surface during these tests using a layer of epoxy resin. For these battery thermal ramping tests, the cell surface temperature and ARC oven temperature were both recorded.
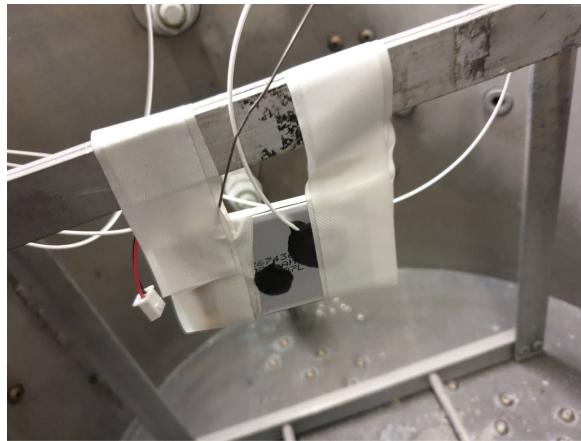
Figure 7.9: Pouch cell test sample suspended in the ARC.

7.3.2 Results and Discussion

Metal Block Reference Test

The results for the metal block test were processed using the same methods as those developed in the charge cycling experiments. Peak tracking was utilised to isolate a single peak and compare the changes in both ToF and signal amplitude with the temperature of the block during heating.

Although peak tracking tracks the single peak across the whole test, visual inspection of Figure 7.10 - top panel shows that the ultrasound signal is lost some 3000 minutes into the test. The dashed line is drawn to show this complete change in signal occurs when the metal block is at around 160°C. After this point, the signal changes to a much higher frequency than the 3MHz pulse used for the test, to a 10MHz signal (the natural frequency of the sensor).

The peak tracking of a single peak in the signal allows for the direct comparison plots
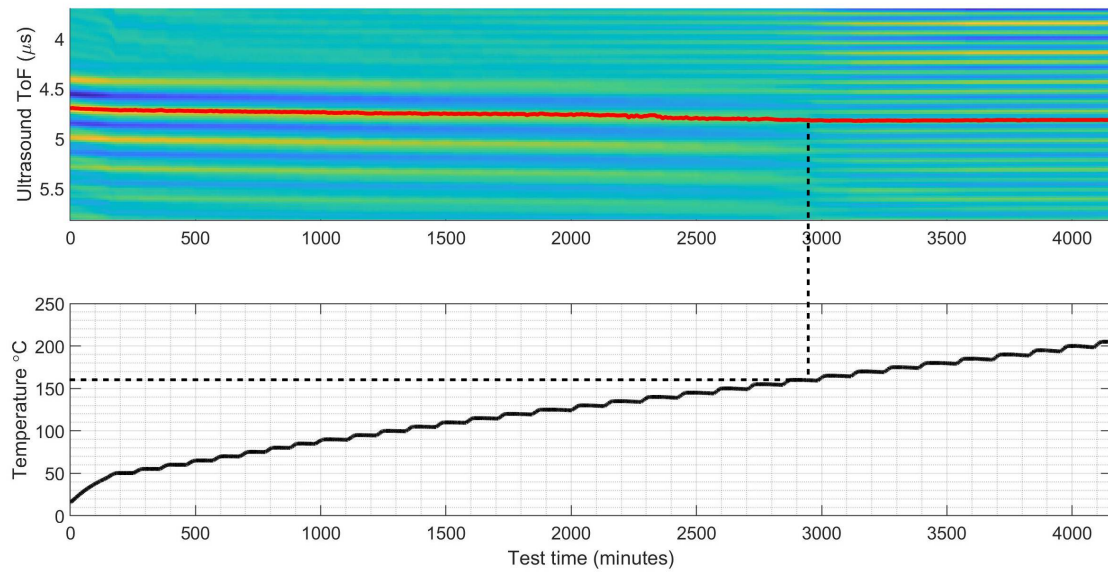
Figure 7.10: Peak tracking of ultrasound response through metal block.

| (a) | (b) |
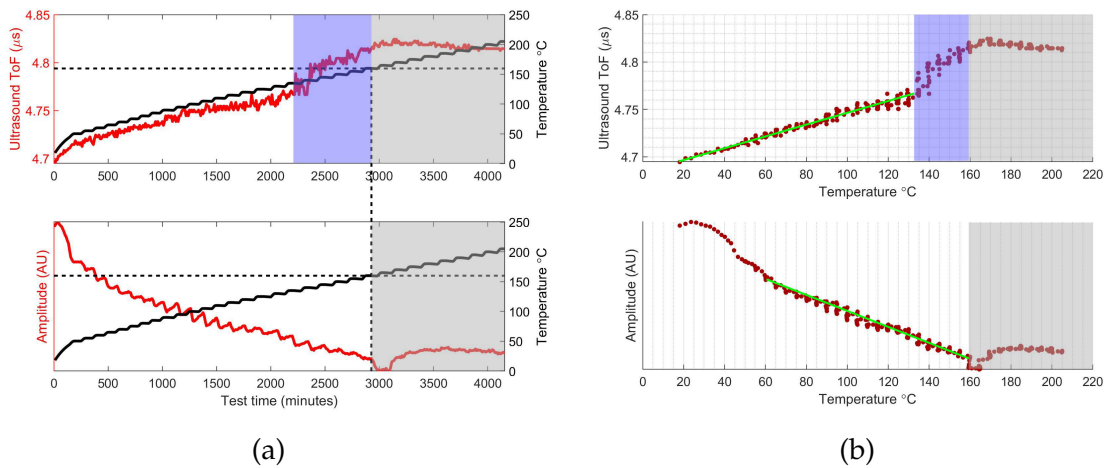
Figure 7.11: Results from metal block/ultrasound instrumentation test. a) ToF/temperature and peak amplitude/temperature comparison plots and b) ToF/temperature and peak amplitude/temperature correlation plots.

in Figure 7.11a and the correlation plots in Figure 7.11b. In the comparison plots, the dashed lines are transferred from the point where the nature of the signal drastically alters. The signal after this can therefore be disregarded and is greyed out. Up to this point there is a linear ToF/temperature relationship, although this is lost somewhat after 2200 minutes/135°C, this deviation from linearity is shaded in blue. The signal amplitude comparison plot shows a stable inverse relationship with temperature up to the loss of true signal event at 3000 minutes/160°C.

The correlation plots show the relationship clearly with the green line in Figure 7.11b - top panel showing strong linear ToF/temperature tracking from the test start, 20°C, to around 135°C. The amplitude/temperature green line in the bottom plot shows a linear relationship from 60°C (soon after the initial ramp to 50°C) up to approximately 160°C when the signal is no longer effectively measuring the block. This result provides confidence that the ultrasound sensor hardware is suitable up to 135°C. Linear changes are to be expected in the signal up to this temperature and any deviation from linearity would be a function of changes within a battery cell as it heats.

Battery Tests

For the battery tests, the battery charge cycling data was joined with the thermal abuse data to provide a single test to analyse. Figure 7.12 shows the two data sets joined forming a single test. The bottom panel displays the temperature data during charge cycling (up to 1500 minutes approximately) and during the thermal ramping afterwards, the y-axis is presented in log scale here to retain visual detail at the lower temperatures. There is a sudden loss of signal after approximately 3000 minutes as the cell did go in to thermal runaway in these tests, as expected. The cell, ultrasound sensors and attached wiring was destroyed at this point.
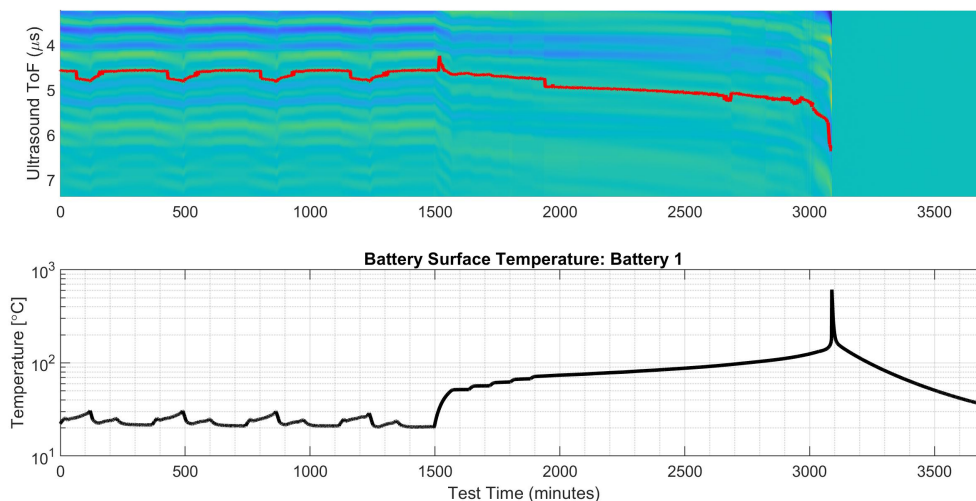
Figure 7.12: Peak tracking of ultrasound response through battery 1.

The peak selected for tracking for analysis was determined the clarity of the peak and by the strength of correlation between peak ToF changes and battery SoC. From the work in section 5.2, it is clear that not all peaks report battery changes efficiently, as such it was important that the thermal abuse analysis selected the optimum peak to

show ultrasonic changes as a function of internal battery changes, rather than temperature. Issues around signal quality and interpretations of internal cell changes are discussed in greater detail later in this section.

Figure 7.13a shows the tracked peak ToF synchronised with the cell surface temperature. The dashed line represents a threshold of 130°C, above which ultrasound measurements are no longer reliable, according to the findings in the metal block test (135°C less 5°C to allow for material discrepancy). A blue marker is placed at the time where the cell temperature reaches this threshold, a red marker is placed on the tracked ToF to show measurements are discarded after this point. The grey shaded area shows time after thermal runaway whilst the blue shaded area shows the time between loss of instrumentation reliability and thermal runaway. The blue region being narrow providing some confidence that the ultrasound gains meaningful data almost up to the point the cell is destroyed. These annotations are also included in Figures 7.14a & b.
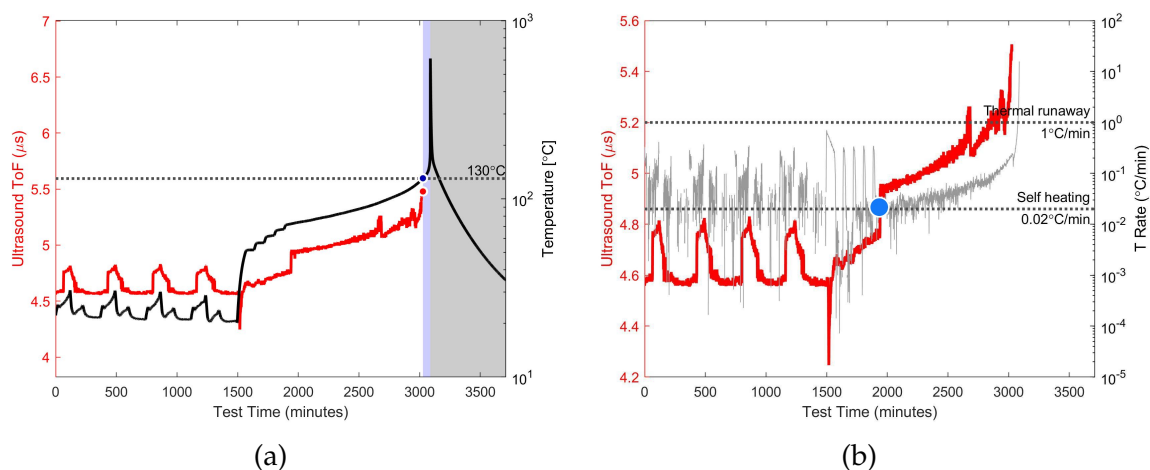
Figure 7.13: Ultrasound/battery temperature comparison plots a) ultrasound ToF and cell surface temperature b) ultrasound ToF and temperature change (T-rate).

The rate of temperature change in °C/min compared with signal peak ToF is shown in Figure 7.13b, dashed lines are drawn to show the points at which the onset of self-heating and thermal runaway occurs. The pale blue marker is placed at the point where temperature increases over the self heating threshold whilst the cell is at rest with no charge or external thermal activity taking place. Note a change in the ultrasound ToF at this point, this could be attributed to peak 'snapping', where peak tracking snaps to an adjacent peak in error, this is possible when inspecting the top panel of Figure 7.12, However it appears more likely even if snapping is the cause, a loss in signal fidelity facilitates the change at this point.

Comparisons between the amplitude of the tracked peak and battery temperature are shown in Figure 7.14a. As with charge cycling, signal amplitude is an erratic measure of lithium-ion batteries. Signal power, a measuring method utilised by Hsieh et al., calculated by summing the signal amplitude across the entire signal response[19] (referred to in their work as signal amplitude, but distinct from the signal 'peak' amplitude used in this work) is shown in Figure 7.14b. Signal power is calculated in the same manner here, by summing the 'area under the curve' across the whole signal response. This additional method of measuring ultrasound is considered as it gives a holistic view of the signal, enabling fair comparisons between cells with peak selection no longer a factor. As seen in the Figure 7.14b this value is erratic and difficult to interpret.
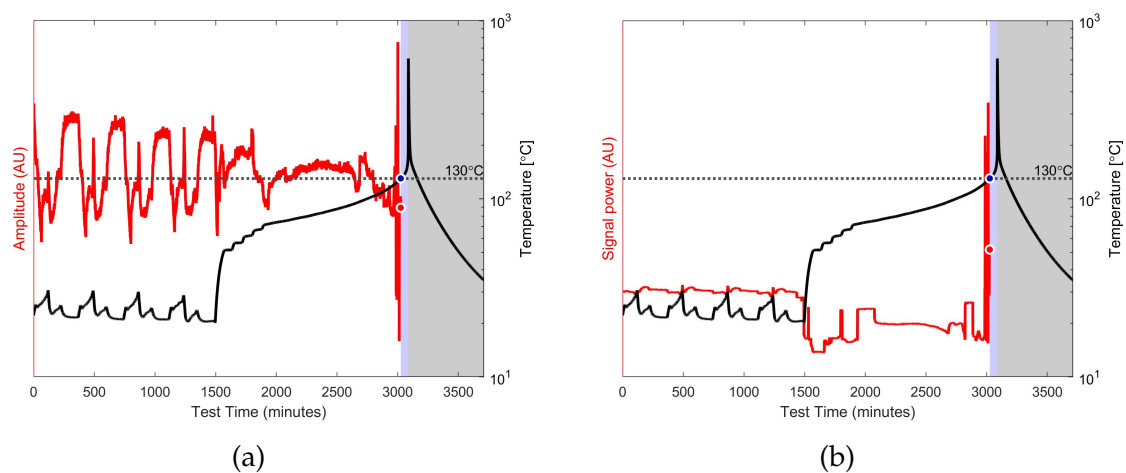
Figure 7.14: Ultrasound/battery temperature comparison plots a) ultrasound signal peak amplitude and cell surface temperature b) signal power and cell surface temperature.

Following from the analysis methods developed in section 5.2. Correlation plots are produced in Figure 7.15 of battery temperature and the various ultrasound parameters; ToF (top), peak amplitude (middle) and signal power (bottom). These plots are all cropped to only show data up to the established 130°C threshold.

Recall from the metal block test that the relationship between ToF and temperature was almost perfectly linear (Figure 7.11b - top). In the ToF/temperature plot on top of Figure 7.15, there are clearly seen to be slight but distinct deviations from a linear trend, which must be attributed to battery changes. The changes in signal amplitude (Figure 7.15 - center panel) are less defined and more erratic. This agrees with the findings during charge cycle testing, that signal amplitude is an unreliable indicator of battery charge when compared to the change in ToF. A correlation plot for signal power is shown in the bottom panel of Figure 7.15, this value is fairly constant across the test

with some variations occurring through the test that may be providing insights into battery evolution.
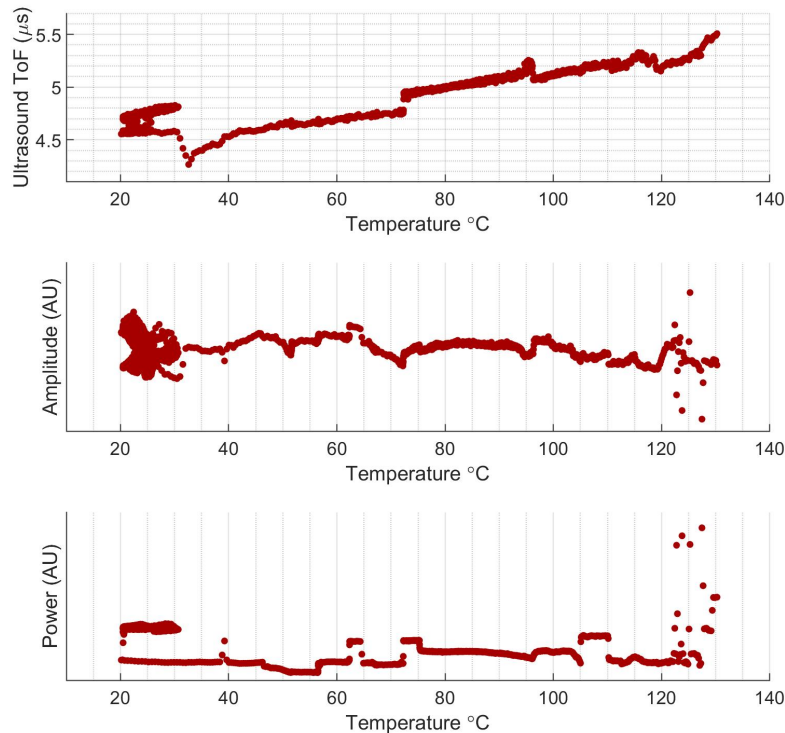
Figure 7.15: Ultrasound/temperature correlation plots; (top) temperature/ToF, (center) temperature/amplitude and (bottom) temperature/signal power.

The correlation plots in Figure 7.15 are all from battery 1. Presented this way, clusters of ultrasound measurements are created at points where the cell spends most time at this temperature. This is most evident in the clusters that form at the lower end of the temperature range, from which charge cycling/ultrasound data is obtained. To improve visual analysis of the results, 0.5°C *bins* are created. In each bin, ultrasound measurements are collected and averaged giving a single ultrasound value for each half degree C.

Performing this averaging step also serves as a smoothing function, which improves the results when all three battery tests are overlaid, as shown in Figures 7.16 to 7.18. Figure 7.16 contains the change in ToF of a selected peak, tracked over the course of the test (charge cycling and thermal abuse). The results for each cell are shaded red (see legend) whilst the metal block data is plotted as blue dots. The metal block reference

then has a third degree polynomial fit applied, which is plot as the solid blue line, the 95% confidence intervals are bounded by the blue shaded region. The plot is cropped at 130°C as data over this threshold has been shown to be unreliable.
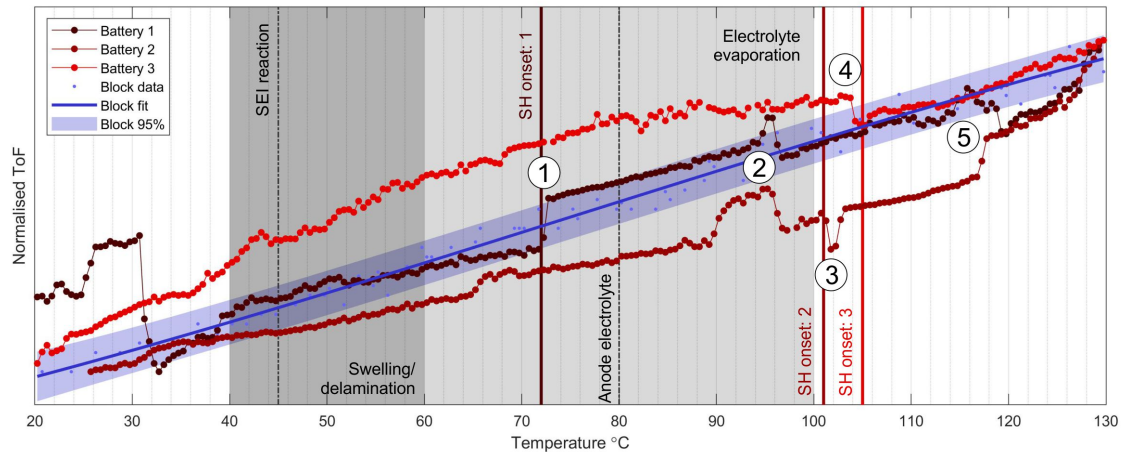
Figure 7.16: Composite correlation plots showing ToF/temperature relationship for batteries 1-3 (shaded red). Metal block reference shown in blue, complete with fitted curve and 95% confidence intervals. Annotations of expected battery events during heating marked and labelled accordingly.

Battery 1 follows a similar linear trend to the metal block throughout the test. There are some expected discrepancies at the lower temperature due to charge cycling, the ToF then increases at a similar rate to the metal block. A noticeable jump occurs at 72°C, marked (1), this is at the point where the onset of self heating was identified (see the pale blue marker in Figure 7.13b). There are distinctive jumps in the ToF tracking for battery 2, marked (3) and battery 3, marked (4), these also correspond to the points where the onset of self heating was identified, 101°C and 105°C respectively, these identified points are annotated on the plot.

A feature occurs in batteries 1 and 2 where the ToF temporarily increases and returns between 90°C to 100°C, marked (2). It is unclear what drives this temporary change, the features occurs in the electrolyte evaporation region (shaded light gray), the temporary nature and replication in two cells would merit further exploration. The point marked (5) again shows features in cells 1 and 2 occurring at approximately 115°C, these are difficult to explain currently. These are a clear deviation from the linear relationship of the metal reference block and so should be assumed to be battery related. It should be noted here that the test on battery 3 is regarded as inferior quality to that on batteries 1 and 2, this will be discussed in detail shortly.
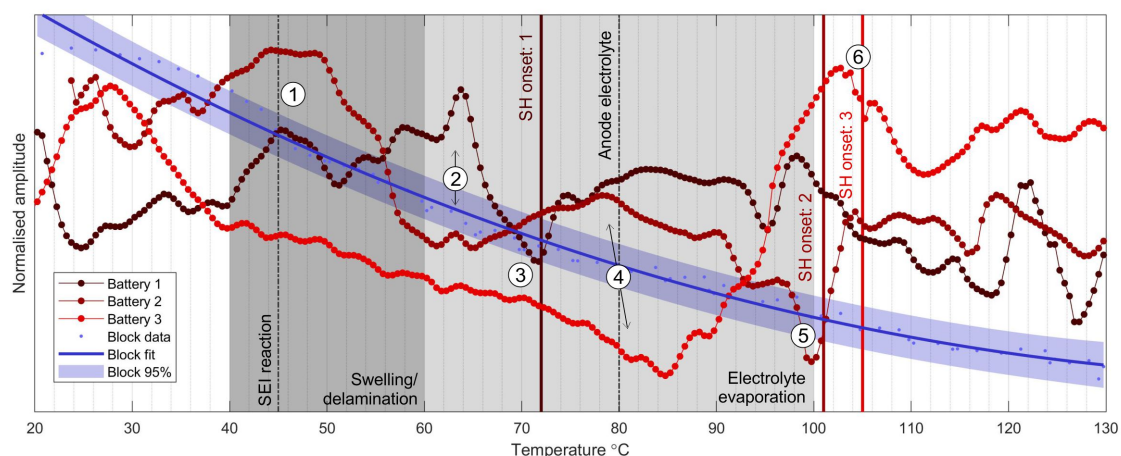
Figure 7.17: Composite correlation plots showing tracked peak signal amplitude/temperature relationship for batteries 1-3 (shaded red). Metal block reference shown in blue, complete with fitted curve and 95% confidence intervals. Annotations of expected battery events during heating marked and labelled accordingly.

The signal amplitude is explored in Figure 7.17. The plot is annotated with all the same information as the ToF plot, points of interest derived from Table 9. The first point to note is tracked peak amplitude for the metal block reference has an exponential relationship with temperature resembling a second order polynomial. The trend remains well defined however with the 95% confidence interval shaded blue close to the fitted curve.

Marker (1) shows a feature shared by cells 1 and 2 where the signal amplitude peaks. These features are noted as they occur at 45°C, around the points where SEI reactions can occur. Similarly, marker (2) shows a temporary rise in amplitude for cells 1 and 2 at approximately 64°C, just after the temperature range where the electrode can start to separate from the current collector, known as delamination. As with the ToF correlations, there are signal feature changes at the critical points where the onset of self heating is defined. There is a peak at each of the points almost exactly where the signal amplitude crosses the specified point, cell 1 marked (3), cell 2 marked (5) and cell 3 marked (6). There is a slight peak detected at marker (4), this occurs in all 3 cells at around 80°C at which point the anode starts to react with electrolyte releasing heat.

The signal power measurement for all 3 cells is shown in Figure 7.18. The same annotations of points of interest are applied, the signal power for the metal block reference test is plot using the blue points for data, fitted curve in blue with 95% confidence intervals bounded in the blue shaded area. The relationship between signal power and temper-

124
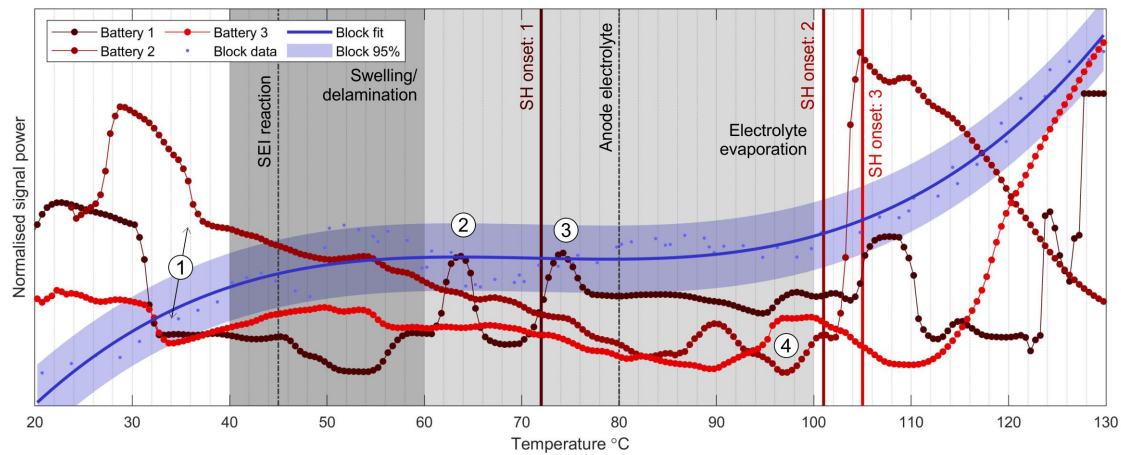
Figure 7.18: Composite correlation plots showing signal power/temperature relationship for batteries 1-3 (shaded red). Metal block reference shown in blue, complete with fitted curve and 95% confidence intervals. Annotations of expected battery events during heating marked and labelled accordingly.

ature for the metal block resembles a third order polynomial, again the deviation from this is low and the confidence intervals are narrow.

There is a distinct feature early in the tests where the signal power drops at approximately 35°C, marked (1). This is explained by the signal tracking battery charge alongside temperature fluctuation in low temperature regions (recall that each point here is a mean of several measurements), once out of this low temperature band the signal power remains fairly consistent in each battery until higher temperatures. The features here appear more difficult to interpret, there are two significant peaks in the battery 1 test, marked (2) and (3), it is unclear what drives these, although (3) occurs just after the onset of self heating. Marker (4) shows a period just prior to large changes in signal power (particularly for cell 2), this could be matching the rapid rise after a stable reading in the hardware as the signal power rises significantly in the metal block test after 100°C.

The metal block reference test was used to verify the hardware stability as the ARC, test sample and ultrasound instrumentation heated up. As previously stated, signal response quality could be checked using the cycling data section of the tests. The quality of the signal response is judged on how well the signal tracks internal battery changes with respect to SoC rather than temperature changes. It was acknowledged that if ultrasonic measurements closely track temperature, this is providing limited insights into the internal state of the battery cell.

A method of checking signal quality is to compare the correlations of battery SoC and cell surface temperature with change in ultrasound ToF and amplitude for a selected peak as described in section 6.3. The single peak selected for each of the three test was based on two main conditions; a strong peak which could be tracked without error through cycling and the best ToF/SoC correlation in conjunction with signal strength. These decisions were possible by analysing the charge cycling data using the exact methodologies outlined in Figure 5.7 in section 5.2.
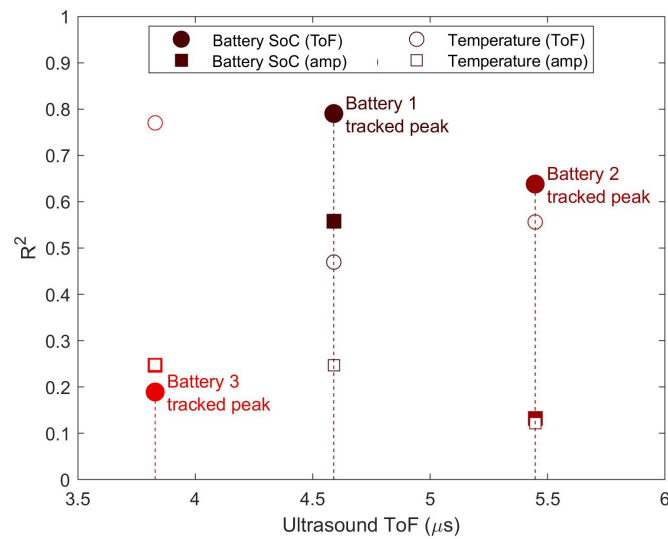
Figure 7.19: Evaluation of selected peak/signal quality, using SoC/temperature bias method.

From the charge cycling tests performed throughout section 6, it is claimed that a good quality signal will show a strong relationship between change in SoC and change in ToF. Therefore good quality signal would expect to see a strong battery SoC/ToF relationship and a weak temperature/ToF relationship. Figure 7.19 shows that the sensor on battery 1 performed well, battery 2 was satisfactory, whilst the sensor on battery 3 was poor.

This work refers to this signal quality, defined as the strength of ultrasound relationship with battery SoC and cell surface temperature as *bias*. A charge bias will tend towards stronger battery correlations (battery 1 tests) and a temperature bias will tend towards stronger temperature correlations (battery 3 test). Whilst peak amplitude can provide strong battery charge correlations, it has shown in this work to be erratic and unpredictable to use without offering any advantages over ToF. As such this work considers ToF for the measure of signal quality. The best charge bias was from the instrumentation of battery 1, with an R^2 of 0.79 for SoC compared to 0.47 for temperature.

Battery 2 had a level bias with R^2 of 0.64/0.56 for SoC/temperature. Battery 3 was bias towards temperature with R^2 of 0.19/0.77 for SoC/temperature. For reference, a comparable charge cycling (0.5C rate) test using commercial probes had a bias of 0.88/0.36, R^2 for SoC/temperature.

7.3.3 Conclusions

The metal block reference test was effective in defining the limitations of the bonded sensors when ramping to high temperatures. The ultrasound measurements remained stable up to 135°C after which the amplitude and therefore time of flight readings become erratic, unpredictable and unusable. Considering this, a 130°C limit was imposed on the battery cell data analysis.

The thermal abuse of the batteries cause all three tested cells to go into thermal runaway destroying the cell and attached ultrasound sensor instrumentation in the process. This was an expected and desired outcome of the tests. The sensors themselves varied in the quality of battery insights, checked by assessing the bias of each sensor towards tracking SoC or temperature during charge cycling. The test on battery 1 was considered successful, the sensor on battery 2 was considered satisfactory whilst the data from battery 3 was shown to be of poor quality and should not be regarded as insightful.

There were well defined features in the ultrasonic measurements during thermal ramping, occurring at critical moments such as the onset of self heating. In tests 1 and 2 there may have been a sign that the evaporation of electrolyte had been detected, the temporary change in signal around 95°C was well defined in each test. This would warrant further investigation with improved sensors. Other features developed in the amplitude and signal power that would benefit from further repeats with improved signal quality.

Signal quality was identified as the limiting factor in this second phase of tests. Following this, the decision was made to conduct a third phase of testing using commercial probes.

7.4 Phase 3: Commercial Probe Tests

In this third phase of testing, there was a move away from bonded sensors considering the concerns over temperature bias in the signal response. It is thought that the sensors did not emit waves with enough power to travel all the way through the cell and return to the sensing edge with a reflection or half reflection from which to take accurate measurements. As such the lack of cell penetration causes the signal to be dominated by reflections in the early layers, including the casing and sensor/bonding material, causing a temperature domination of the signal response. In this phase a return to commercial probes was explored.

7.4.1 Set Up

In an attempt to improve on the results from the bonded sensor tests in phase 2 of testing. Several commercial probes were obtained, similar to those that had provided strong battery insights throughout charge cycling tests. A battery charge cycling/thermal ramping test was performed using a commercial probe. The probe was attached to the cell using superglue in accordance with the superglue comparison in Section 6.6.1. This permanent fixing was preferred for the first test as this would ensure the location of the sensor remained stable, should swelling occur during heating. The probe was clamped to restrict extreme swelling, shown in Figure 7.20a.
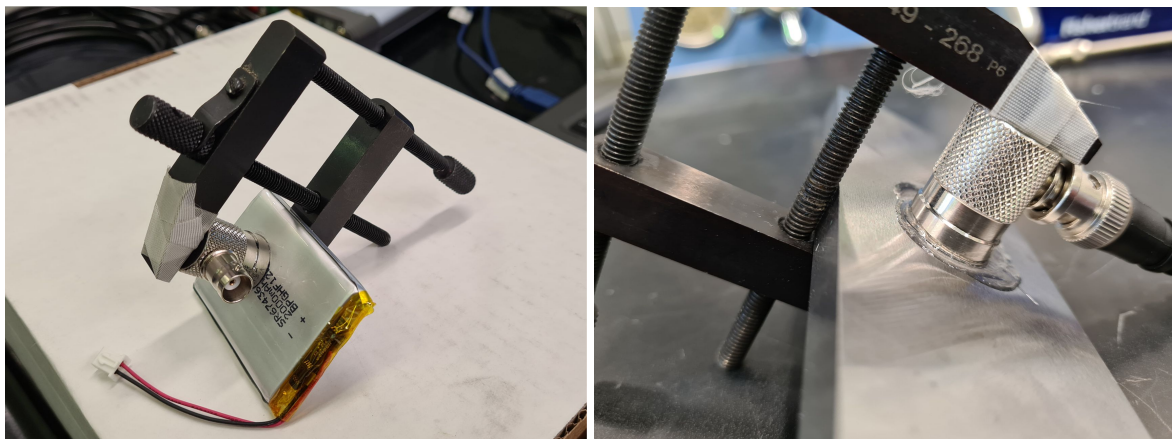
(a) High temperature gel couplant/clamp   (b) Metal reference block

Figure 7.20: Commercial probe instrumentation.

Once again, a metal block reference test was conducted (Figure 7.20b) to assess the feasibility of the instrumentation. High temperature gel (rated up to 398°C) was used

as couplant with the sensor held in place with a hand tightened clamp in the same manner as tests in section 6.

A second metal block reference test using high temperature gel was performed. Test parameters were designed to identify a definitive temperature range, above which the bonding/couplant method becomes unreliable. The ARC was set to heat the metal block to 30°C, 50°C, 70°C and 90°C, allowing the sample to cool (to room temperature) between each step for approximately 24 hours. This would provide knowledge about the limitations of this test set up, where a signal is permanently altered either due to bonding/couplant issues or heat damage to the sensor.

7.4.2 Results and Discussion
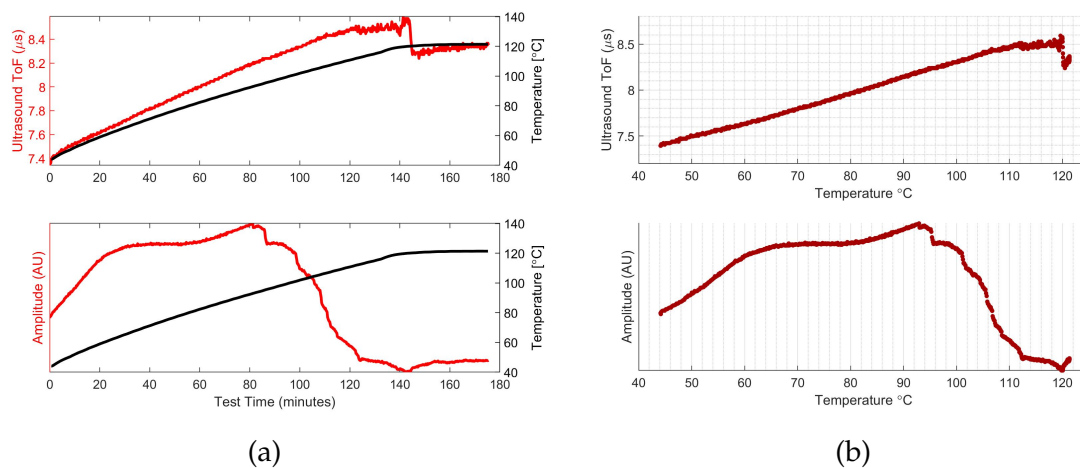
Figure 7.21: a) Ultrasound/temperature variations during test and b) same data plotted as ultrasound/temperature correlation plots for battery thermal ramping test.

The results for the battery cell thermal ramping test using superglue are shown in Figure 7.21. There are two issues considered with this data, firstly, the tracked peak ToF relationship with temperature appears to be linear right up to and beyond 110°C. This was an unexpected deviation from the results in section 7.3.2 where the ToF showed distinct deviations from this linear relationship (recall Figure 7.16). As such this commercial probe test provided no ToF insights into battery changes during thermal ramping. It is important to note at this stage, that processing data from the charge cycling test, conducted prior to the thermal ramping test produced poor results. The R^2 value for ToF/SoC was just 0.6 whilst the ToF/temperature had a R^2 of 0.61. This even split and lack of bias towards battery SoC was anomalous for commercial probe testing.

129

Secondly, there is unusual signal amplitude activity on the thermal ramping test on the battery. There is a change in the relationship between amplitude and temperature at around 60°C and again at approximately 90°C before decreasing sharply. It was thought likely this is a change in the properties of the superglue couplant as it heats. Although it still works, the signal is inconsistent and becomes an unwanted variable in the test system.

The results for the metal block reference test using high temperature gel couplant are shown in Figure 7.22. Whilst a positive relationship exists between temperature and tracked peak ToF, the relationship is not linear, like that shown in the metal block reference test in Figure 7.11b - top panel. Additionally, the signal amplitude drastically reduces at approximately 100°C, a significant downgrade on the stable signal achieved using bonded sensors.
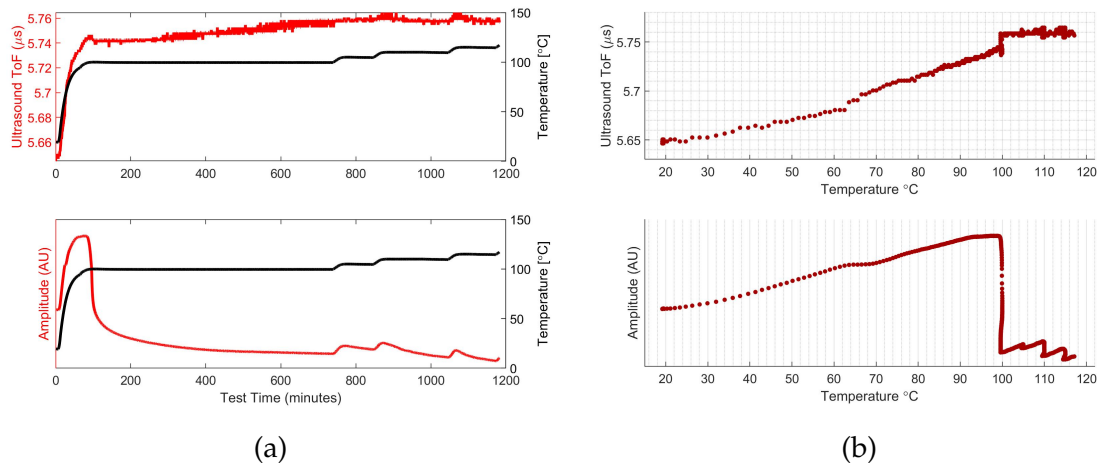
Figure 7.22: a) Ultrasound/temperature variations during test and b) same data plotted as ultrasound/temperature correlation plots for metal block thermal ramping test.

The results of the second and final metal block reference test are shown in Figure 7.23. Whilst the test is successful in terms of identifying apparatus limitations, the result is disappointing, showing that heating up to 70°C causes permanent change in signal in both ToF and amplitude. Marker (1) shows the signal at 30°C, the ToF and amplitude return their starting places during cooling, this is also true up to 50°C, marked (2). Whilst there appears to be a repeated pattern at marker (3) with the same path in ToF and amplitude taken, there is deviation upon cooling in both, ToF and amplitude return to new resting points at room temperature. This effect is repeated again to further alter both ToF and amplitude after heating to 90°C at marker (4) and cooling back down, marker (5). With this information, no thermal ramping test can reliably be per-

formed using this set up that plans to go above 50°C. It should be noted that the ARC was opened and the sensor was reapplied using fresh high temperature gel just prior to the 90°C ramp at marker (6). Reapplication of the sensor/gel did not alter the signal, so changes are safely assumed to be sensor based.
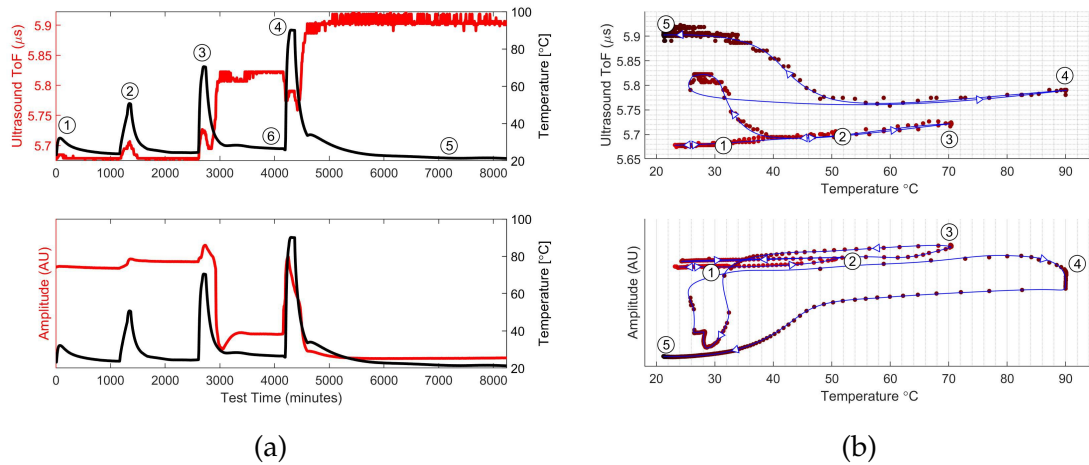
Figure 7.23: a) Ultrasound/temperature comparison plots and b) Ultrasound/temperature correlation plots for apparatus limitations test.

7.4.3 Conclusions

The commercial sensor tests were disappointing. Using superglue or high temperature gel as couplant produced poor results, inferior to those obtained using bonded piezo-ceramic elements used throughout section 7.3. The metal block reference test showed that piezo-ceramic elements bonded to the surface using epoxy resin could provide reliable and stable results up to 130°C. The limitations test of the metal reference block using commercial probes shows this test apparatus can only provide stable and reliable results up to 50°C. Whilst there appears to be some effect during heating on the gel couplant, the sensor itself is a significant problem, upon heating, the sensor is damaged and whilst reflections are obtained, signal power is diminished and therefore reliability is lost.

7.5 Conclusions

- Instrumented lithium-ion cells with bonded sensors as opposed to commercial probes due to the likelihood of sensor damage/destruction at high temperatures

131

($100°C+$). Successfully obtained a signal response using this alternative method.

- Results show a strong linear relationship between ultrasound response and cell temperature increases. In initial tests, some temporary or sudden non-linear features occurred in the peak tracking. These were difficult to attribute to either internal cell reactions or instrumentation effects due to heating.

- Metal block reference tests were conducted to help determine the effects increasing temperate have on ultrasound responses due to instrumentation, sensors/bonding/wiring. This was successful in showing a clear linear relationship between a tracked ultrasound peak change in time of flight and temperature up to $135°C$. The relationship between tracked peak amplitude and signal power with temperature resembled second and third order polynomials respectively.

- Repeatability was introduced into experimental designs with three identical tests conducted on three identical cells using the same methodologies throughout. There was a variation in signal quality however that negatively affected the ability to precisely locate non-typical features in the ultrasound measurements.

- Each test was designed to include a cycling section before thermal abuse tests, primarily to ensure all cells were cycled from new in the same manner and to leave at 100% state of charge. The signal quality was assessed using this cycling data, assessing the temperature bias method developed in section 6.3.

- To improve on the variable quality of the bonded sensor tests, commercial probes used in charge cycling tests throughout Chapter 6 were planned for thermal abuse testing. On the metal block reference test, the sensors performed very poorly. A second metal block reference test was designed to estimate the temperature limit above which a probe is no longer suitable for ultrasonic monitoring. This shows that this arrangement is only reliable up to $50°C$, far below the $135°C$ limit for the bonded sensors.

- Using the bonded sensor tests, with sensors on batteries 1 and 2 being considered reliable, it is concluded that ultrasonic monitoring of a battery differs from the metal block reference when measuring time of flight of a tracked peak at key and consistent points. These differences can be attributed with some confidence to known and expected cell reactions, in these tests the onset of self-heating is thought to be identified. There is a tracked peak time of flight deviation from the linear metal block reference at $115°C$ that would require further investigation.

- Signal amplitude of a tracked peak during battery cell heating deviates from the exponential relationship in the metal block test at key points. There are peaks identified at 45°C, the range where SEI reactions can occur. There is also a temporary rise in signal amplitude at 64°C, approximately where electrode delamination occurs. As with time of flight, features exist in the signal amplitude at the points where the onset of self heating occurs.

- There are changes in signal power during battery cell tests, deviating from the metal block reference that are not consistent in batteries 1 and 2. It is concluded that signal power is a less reliable monitoring method and more difficult to interpret.

8 Conclusions

Lithium-ion batteries are increasing in popularity, from consumer electronics powered using this technology to electric vehicles. The electric vehicle market in particular is expected to drive a large increase in demand for this method of power delivery over the coming 10 years. This is largely due to electric vehicles being widely accepted as a clean transportation solution compared to the internal combustion engine. The limitations around safe and effective use of lithium-ion batteries forms a large and ongoing area of research. The development of battery management systems search for more accurate and insightful monitoring methods of the batteries.

Ultrasonic monitoring is a growing battery monitoring technique, being a non-invasive, non-destruction means of gaining real-time measurements of the internal changes of a battery cell. Ultrasound responses are sensitive to internal changes in lithium-ion batteries during normal operation, for example changes in electrode densities during charge cycling. There are also ultrasound responses to internal reactions of a cell during non-standard operation, such as thermal abuse conditions. This thesis focused on ultrasound inspection through experimental testing under both normal and abuse conditions. Developing the method with signal processing techniques and modelling waves through a multi-layered body.

8.1 1D Wave Multi-Layer Modelling

A 1D wave model was created based on the wave equation partial differential equation. The model was created using MATLAB and various outputs are designed to show the behaviour of transmitted waves travelling and reflecting through multiple layers. From this modelling it is revealed how small dimensional, density or ordering changes from battery to battery can cause the signal to vary significantly in each case. This can impair the intensity of wave changes as a function of state of charge and can also cause render preferred measuring methods unreliable or impractical.

The model simulates waves when they encounter material boundaries, successfully modelling reflections and partial reflections where the waves span several layers. Modelling outputs are designed to show developments of transmitted and reflected waves travelling through the multiple layers, plotting frames to animate travelling waves and A-scan generation. These visualisations aid in the selection of pulse frequency. 2MHz

pulse frequencies are primarily used in this work and in much of the literature, using wave development plots and animations, motivation for this selection is provided.

The effects of temperature on signal responses can be simulated. Modelling this effect finds that at high temperature fluctuations, either from ambient temperature changes or cell temperature changes, signal response correlations tend towards a temperature bias. The can cause a loss in signal accuracy with respect to changes in state of charge.

8.2   Apparatus and Analysis Methods

Test apparatus and methodologies suitable for the ultrasonic monitoring of lithium-ion batteries were identified and acquired. A single commercial probe sensor, in pulse/echo set up was used as standard during charge cycling tests. Variations on this configurations were explored, usually driven by experimental conditions. Dual sensors using a through pulse and signal amplification was selected to monitor a large capacity cell. Bonded sensors were chosen as opposed to commercial probes for thermal abuse testing. The signal response quality using bonded sensors is currently considered inferior to that of commercial probes in this work.

Further apparatus was utilised in experiments during the course of this work. A thermocouple was added to test set up to monitor the surface temperature of a cell during charge cycling, a key test development in determining the effect of temperature fluctuations on signal responses. A multiplexer was incorporated into a test kit built towards the end of this project, enabling 14 channels, combined with signal amplification. The purchase of a Cadex portable battery analyser was made, enabling portable/bench top charge cycling.

The synchronisation and analysis of data from the various sources is performed using a MATLAB script developed to allow for some user interaction and some degree of automation/repetition. Peak tracking forms a fundamental aspect of the analysis, with a user asked to select a peak, the script automatically tracks the selection over the test. Peak tracking can be isolated and collated according to charging status to help provide visual context to ultrasound responses with respect to charge. A range of analysis options are available to the user, signal processing, correlation testing/method, multiple peak tracking and comparisons are amongst the many tools developed to understand the relationship between ultrasound responses and changes in a lithium-ion battery.

8.3 Standard Testing: Charge Cycling

From analysis of experimental data, time of flight measurements show better correlations with battery state of charge when compared to the signal amplitude. Additionally, this correlation is stronger comparing ultrasound with battery SoC rather than voltage. Variations in instrumentation in addition to variations in the layered construction of a cell, can lead to unpredictable signal responses. This can be problematic for some measuring/analysis techniques, such as signal enveloping which may be difficult or impossible to obtain.

In order to deal with signal response variations. A method using the cross wavelet transform to gain amplitude and phase shift activity along the transducer/pulsing frequency band across the signal, can provide a 'smart peak' selection region that has the capability to automate the peak that will provide the most accurate battery charge measurements. This method relies on two reference signals from non-identical parts of the charge cycle to be effective.

Signal peak amplitude and change in time of flight do not alter with state of charge in the same manner, it is shown that time of flight has stable correlations with battery charging whereas although some peaks have good amplitude/charge correlations, this is much more erratic across the signal. In addition, even with time of flight, when using a single sensor in pulse/echo, peaks do not alter in a uniform manner across the signal. There is an apparent unpredictability regarding how each peak alters during cycling. This is not the case for through pulse signals, where each peak has approximately the same behaviours across the signal.

Change in temperature is a factor that affects wave speed through any medium, along with changes in density and elasticity. To assess the effect of temperature, a thermocouple was attached to the battery during cycling, it was found that both battery activity and the ambient temperature of the laboratory caused changes in battery surface temperature by $\pm 7^\circ$C and this has little effect on the stability of the time of flight readings. From experiments on large capacity cells using higher C-rates combined with modelling however, it was shown that should the temperature effects be large enough this could prevent the capability of taking reliable and accurate ultrasound/SoC readings. A method is suggested to calibrate signal responses to dampen temperature effects using battery rest/temperature change data. A slight improvement in charge correlations is gained, whilst temperature correlations are damaged somewhat.

8.4 Non-Standard Testing: Thermal Abuse

In thermal abuse testing, samples are heated to over 100°C with an intention of causing thermal runaway, destroying the cell and connected instrumentation. Considering this, bonded sensors were used as opposed to commercial probes. Using metal block reference tests, it was determined that bonded sensors were suitable for ultrasonic monitoring up to 135°C while commercial probes were suitable only up to 50°C.

It was concluded that where measuring time of flight of a tracked peak differs from the metal block reference during ultrasonic monitoring of a battery, the difference can confidently be attributed to known features. In these tests, the onset of self-heating was thought to have been identified. Onset of self heating was also detected as a deviation from the reference using the peak amplitude measurement. Changes in peak amplitude not present in the reference test occur at temperatures consistent with SEI reactions and electrode delamination. Signal power was analysed, there are discrepancies with the reference test that are difficult to interpret without further testing and more consistent signal quality.

8.5 Future Work

Introduction

During the course of this work, many different avenues for future work have presented themselves. The work in this thesis provides insights that can help guide future work and in some instances, gives rise to the possibility of exploiting the chaotic and unpredictable nature of waves through a multi-layered body such as a lithium-ion pouch cell. The following presents a summary of planned or suggested future work and details of some work in progress developing methods to utilise the ultrasonic monitoring of lithium-ion batteries.

8.5.1 1D Wave Model

The model is used as a guideline throughout this work, providing approximations of travelling waves interacting with layer interfaces. Simulated A-scans at the sensing edges are obtained from modelling in this work, as whilst the results are assumed to be in reasonable, little attempt is made to evaluate the results against experimentally

obtained signals. This was not pursued based on the assumption that the model in its current state would be unable to fully simulate the true responses when pulsing through a lithium-ion cell.

With this in mind, given the useful insights gained from visualising waves traveling through the cell layers, proving context to the characteristic contained within A-scans. Wave modelling should be developed further with the aim of more closely simulating real wave responses, this would take one of three forms:

1. Further develop and refine the 1D wave model contained within this work.

   - Signal capture could be improved by modelling the ultrasound sensors and couplant method, currently, the waves 'close' to the edge are considered close enough for the purposes of this work. This likely to reduce A-scan simulation accuracy.

   - Modelling the chemistry of the charging process would be an important development. Currently the density of the layers in redistributed evenly across precisely defined boundaries and will almost certainly be an oversimplification of the actual processes involved during charge cycling. Improving would likely help to identify signal response features that could only be explained as a result of the complex reactions in the cell.

   - Careful attention should be given to the reflections at layer boundaries. Some work, not included in this thesis, was done comparing the time of flight measurements of the model compared to theoretical times. It was shown that whilst the timing of wave reflection matched exactly with the theoretical expectations, the amplitude and phase was not checked. This would be an important investigation to continue to validate the reflections, including comparing modelled reflections with expected reflection coefficients.

   - Currently, attenuation is modelling by arbitrarily reducing signal amplitude over time. The model would benefit from improved attenuation modelling, driven by the causes of this such as signal scattering and lost energy through absorption and beam spread.

   - Obtain wave responses from a simple layered body such as a bearing shell for direct comparison with modelled equivalent to assess model accuracy more completely.

2. Consideration of existing modelling solutions. During the course of this work, the decision was made to develop the modelling in this thesis to help understand the nature of the wave responses when travelling through the cell. This was mainly driven by the ability to build the exact tools desired for this project, namely frame by frame captures of waves passing through material boundaries. This was later developed further to include animations to see 'real-time' A-scan generation. Attempts to use other existing modelling tools utilised in other studies from the literature were cancelled to concentrate of other tasks during this work. It would be very helpful however to return to these ideas to assess now whether they could improve upon modelling in this work. This would include Clawpack, Dualfoil or the commercial modelling software Comsol.

8.5.2 Ultra High Frequency Ultrasound (UHFUS)

The modelling in section 4.7 shows that should resonance be found in the layers contained within a lithium-ion battery, it may be possible to retrieve information on the layers by analysing the signal in the frequency domain. In order to verify this experimentally, at least two ultrasound probes would be required being at least in the order of 40MHz. Two being required as modelling shows that the method would only be effective in a pitch/catch through pulse configuration.

The script built to analyse experimental data covered in section 5.2 already contains the functionality of analysing signals in the frequency domain in addition to the standard technique of analysing in the time domain. Peak tracking is applied to frequency peaks throughout testing rather than signal peaks. This feature is not covered in this thesis. But some development of this frequency domain analysis would be essential should ultra high frequency signals be obtained. The modelling shows that complex jumps in dominant frequency may occur being difficult to analyse using existing methods. The possibly of obtain layer information such as material density remains an interesting possibility.

8.5.3 Experimental results with cell tear down

In experiments, it was noted that the signal could differ drastically when comparing cells from identical suppliers and manufacturers. The discrepancies are difficult to explain. In one instance a cell failed to accept charge and the ultrasound signal was lost

on this cell, in future it would be desirable to inspect the internal state of this cell physically to determine the causes of the cell health issue and why this affected the ultrasound signal. It would be useful to compare differing signals from two cells with a tear down to assess the difference in layer structure and how this related to the signal responses. The would also be interesting to compare to layer modelling for model validation purposes, something lacking in this work.

8.5.4 Reverse signal engineering to predict battery cell layer structure

A large part of this study was dedicated to wave modelling and experimental data analysis of wave responses to pulses through multi-layered structures such as a lithium-ion battery cell. The idea of partial reflections has been suggested as the cause of A-scans taking the form they do at the sensing edge. This lack of full reflections contained in the response is noted to cause interpretations of the signal to become difficult. It is suggested here that an algorithm to harness the chaotic nature of waves through a structure containing many layered components can be developed. Based on a basic principle of pulses waves returning to the sensor containing information on all layers encountered. Development and testing of a method of comparing evolving test signals to a reference signals in order to converge on a solution is planned. This would use the modelling in section 4 to generationally refine the layered structure until a close match is found. This would be tested using a modelled reference signal (model to model) to assess the algorithm performance first and model to experimentally obtained reference for a practical algorithm performance review.

CT scan of cells

In addition to the cell tear down discussed previously, an alternative method of gaining information on the internal structure of a lithium-ion battery would be to obtain CT-scans of the cells. The scans would be performed on a Zeiss Xradia 620 Versa X-ray Microscope (XRM) at the Sheffield Tomography Centre (STC) at the University of Sheffield. After initial consultations obtaining CT scans would necessarily require small capacity cells (<400mAh) as the cell needs to fit in the CT-scanner and turn around during scanning. The aims of acquiring the CT scans would included the following:

- Determine basic cell geometry, the greyscale images would be expected to show the differences in material density between the component layers. The greyscale

values on the scan could be compared to normalised density values to draw direct comparisons. Additionally the scan would reveal layer thicknesses and precise number of layers windings. Finally, the scans would confirm the cell construction, such as jelly roll or layered construction.

- Experiments could be carried out where alongside real time ultrasonic measurements during charge cycling similar to those conducted throughout section 6, the cell is positioned in the CT scanner to monitor the cell layers during charge cycling. This would present significant problems however, as each scan can take several hours to complete so the charge process would have to be carefully timed. The cell turns during scanning so instrumentation would be challenging. The cell would have to be positioned in the CT scanner so the Cadex portable charging station covered in section 5.1 could be used for battery charge cycling.

- The cycling experiments above would be complicated and time consuming to conduct. A compromise of this to simply the process would be to step charge the cell outside of the CT scanner, suggesting 0%, 25%, 50%, 75% and 100%. Ultrasound reference signals could be capture outside of the scanner using the Cadex. Comparing signal captures with the greyscale intensity values from the 5 CT scans may show a relationship highlighting the ultrasound being sensitive to density distribution during charge cycling.

Importantly, these CT scans, particularly the cell geometry scans could be utilised in the reverse signal engineering work discussed previously to compare algorithm layer predictions from an experimentally obtained A-scan with the CT-scanned layers from the reference battery.

References

[1] V. Ramadesigan, P. W. C. Northrop, S. De, S. Santhanagopalan, R. D. Braatz, and V. R. Subramanian. Modeling and Simulation of Lithium-Ion Batteries from a Systems Engineering Perspective. *Journal of the Electrochemical Society*, 159(3):R31–R45, 1 2012. ISSN 0013-4651. doi: 10.1149/2.018203jes.

[2] Languang Lu, Xuebing Han, Jianqiu Li, Jianfeng Hua, and Minggao Ouyang. A review on the key issues for lithium-ion battery management in electric vehicles. *Journal of Power Sources*, 226: 272–288, 2013. ISSN 03787753. doi: 10.1016/j.jpowsour.2012.10.060. URL `http://dx.doi.org/10.1016/j.jpowsour.2012.10.060`.

[3] Jianwu Wen, Yan Yu, and Chunhua Chen. A Review on Lithium-Ion Batteries Safety Issues: Existing Problems and Possible Solutions. *Materials Express*, 2(3):197–212, 9 2012. ISSN 21585849. doi: 10.1166/mex.2012.1075.

[4] Gozde O. Sahinoglu, Milutin Pajovic, Zafer Sahinoglu, Yebin Wang, Philip V. Orlik, and Toshihiro Wada. Battery State-of-Charge Estimation Based on Regular/Recurrent Gaussian Process Regression. *IEEE Transactions on Industrial Electronics*, 65(5):4311–4321, 5 2018. ISSN 0278-0046. doi: 10.1109/TIE.2017.2764869.

[5] Grand View Research. Lithium-ion Battery Market Size, Share & Trends Analysis Report, 2021. URL `https://www.grandviewresearch.com/industry-analysis/lithium-ion-battery-market`.

[6] Electric Transportation. Electric Vehicle Sales : Facts & Figures. Technical report, Edison Electric Institute, 2019. URL `https://www.eei.org/issuesandpolicy/electrictransportation/Documents/FINAL_EV_Sales_Update_April2019.pdf`.

[7] Bloomberg NEF. Goodbye Gadgets, 2019. URL `https://about.bnef.com/`.

[8] Zuolu Wang, Guojin Feng, Dong Zhen, Fengshou Gu, and Andrew Ball. A review on online state of charge and state of health estimation for lithium-ion batteries in electric vehicles. *Energy Reports*, 7:5141–5161, 2021. ISSN 2352-4847. doi: 10.1016/j.egyr.2021.08.113. URL `https://doi.org/10.1016/j.egyr.2021.08.113`.

[9] U.S. Department of Energy. All-Electric Vehicles, 2021. URL `fueleconomy.gov/feg/evtech.shtml`.

[10] Qian Lin, Jun Wang, Rui Xiong, Weixiang Shen, and Hongwen He. Towards a smarter battery management system: A critical review on optimal charging methods of lithium ion batteries. *Energy*, 183:220–234, 2019. ISSN 03605442. doi: 10.1016/j.energy.2019.06.128. URL `https://doi.org/10.1016/j.energy.2019.06.128`.

[11] Mashable. iPhone Battery Readings Investigation, 2017. URL `https://mashable.com/article/iphone-battery-readings-investigation`.

[12] BMWBlog. Report: Incorrect State Of Charge Readings on the i3, 2017. URL `https://www.bmwblog.com/2017/04/17/bmw-address-issue-incorrect-state-charge-readings-i3/`.

[13] Microsoft Community. How to fix the Wrong estimate time on battery life using Windows 10?, 2016. URL `https://answers.microsoft.com/en-us/windows/forum/all/how-to-fix-the-wrong-estimate-time-on-battery-life/7a8eb173-75bb-4f30-be5b-9539453aca8f`.

[14] How-To Geek. Why Is My Battery Estimate Never Accurate?, 2016. URL `https://www.howtogeek.com/275846/why-is-my-battery-estimate-never-accurate/`.

[15] Matthew Clarke and Juan J. Alonso. Lithium–Ion Battery Modeling for Aerospace Applications. *Journal of Aircraft*, pages 1–13, 2021. doi: 10.2514/1.c036209.

[16] Josef Krautkrämer and Herbert Krautkrämer. *Applied Ultrasonic Testing of Materials*. Springer-Verlag Berlin Heidelberg GmbH 1990, 1969. ISBN 3-540-51231-4/0-387-11733-4. doi: 10.1007/978-3-662-13257-9{_}4.

[17] R. S. Dwyer-Joyce. The application of ultrasonic NDT techniques in tribology. *Proceedings of the Institution of Mechanical Engineers, Part J: Journal of Engineering Tribology*, 219(5):347–366, 2005. ISSN 13506501. doi: 10.1243/135065005X9763.

[18] Matthias Herrmann. Packaging - Materials review. *AIP Conference Proceedings*, 1597(February):121–133, 2014. ISSN 15517616. doi: 10.1063/1.4878483.

[19] A. G. Hsieh, S. Bhadra, B. J. Hertzberg, P. J. Gjeltema, A. Goy, J. W. Fleischer, and D. A. Steingart. Electrochemical-acoustic time of flight: in operando correlation of physical dynamics with battery charge and health. *Energy Environ. Sci.*, 8(5):1569–1577, 2015. ISSN 1754-5692. doi: 10.1039/C5EE00111K.

[20] Bingbin Wu, Yang Yang, Dianying Liu, Chaojiang Niu, Mark Gross, Lorraine Seymour, Hongkyung Lee, Phung M. L. Le, Thanh D. Vo, Zhiqun Daniel Deng, Eric J. Dufek, M. Stanley Whittingham, Jun Liu, and Jie Xiao. Good Practices for Rechargeable Lithium Metal Batteries. *Journal of The Electrochemical Society*, 166(16):A4141–A4149, 2020. ISSN 1945-7111. doi: 10.1149/2.0691916jes.

[21] Power Sonic. What is a Battery C-Rating, 2021. URL `https://www.power-sonic.com/blog/what-is-a-battery-c-rating/`.

[22] Witold Maranda. Capacity degradation of lead-acid batteries under variable-depth cycling operation in photovoltaic system. *2015 22nd International Conference Mixed Design of Integrated Circuits & Systems (MIXDES)*, 22(June):552–555, 6 2015. doi: 10.1109/MIXDES.2015.7208584. URL `http://ieeexplore.ieee.org/document/7208584/`.

[23] Sabine Piller, Marion Perrin, and Andreas Jossen. Methods for state-of-charge determination and their applications. *Journal of Power Sources*, 6(29):403–404, 2001. ISSN 14394413. doi: 10.1055/s-0029-1195484.

[24] Wladislaw Waag, Christian Fleischer, and Dirk Uwe Sauer. Critical review of the methods for monitoring of lithium-ion batteries in electric and hybrid vehicles. *Journal of Power Sources*, 258:

321–339, 2014. ISSN 03787753. doi: 10.1016/j.jpowsour.2014.02.064. URL `http://dx.doi.org/10.1016/j.jpowsour.2014.02.064`.

[25] Yuejiu Zheng, Minggao Ouyang, Xuebing Han, Languang Lu, and Jianqiu Li. Investigating the error sources of the online state of charge estimation methods for lithium-ion batteries in electric vehicles, 2 2018. ISSN 03787753.

[26] Wen-Yeau Chang. The State of Charge Estimating Methods for Battery: A Review. *ISRN Applied Mathematics*, 2013:1–7, 7 2013. ISSN 2090-5572. doi: 10.1155/2013/953792.

[27] M. Berecibar, I. Gandiaga, I. Villarreal, N. Omar, J. Van Mierlo, and P. Van Den Bossche. Critical review of state of health estimation methods of Li-ion batteries for real applications, 4 2016. ISSN 18790690.

[28] Xuning Feng, Minggao Ouyang, Xiang Liu, Languang Lu, Yong Xia, and Xiangming He. Thermal runaway mechanism of lithium ion battery for electric vehicles: A review, 1 2018. ISSN 24058297.

[29] Jiuchun Jiang and Caiping Zhang. *Fundamentals and Applications of Lithium-ion Batteries in Electric Drive Vehicles*. John Wiley & Sons Singapore Pte. Ltd, Singapore, 5 2015. ISBN 9781118414798. doi: 10.1002/9781118414798. URL `http://doi.wiley.com/10.1002/9781118414798`.

[30] Hartmut Popp, Markus Koller, Severin Keller, Gregor Glanz, Reinhard Klambauer, and Alexander Bergmann. State Estimation Approach of Lithium-Ion Batteries by Simplified Ultrasonic Time-of-Flight Measurement. *IEEE Access*, 7:170992–171000, 2019. ISSN 21693536. doi: 10.1109/ACCESS.2019.2955556.

[31] Yi Sin Chou, Ning Yih Hsu, King Tsai Jeng, Kuan Hsiang Chen, and Shi Chern Yen. A novel ultrasonic velocity sensing approach to monitoring state of charge of vanadium redox flow battery. *Applied Energy*, 182:253–259, 2016. ISSN 03062619. doi: 10.1016/j.apenergy.2016.08.125. URL `http://dx.doi.org/10.1016/j.apenergy.2016.08.125`.

[32] James B. Robinson, Rhodri E. Owen, Matt D. R. Kok, Maximilian Maier, Jude Majasan, Michele Braglia, Richard Stocker, Tazdin Amietszajew, Alexander J. Roberts, Rohit Bhagat, Duncan Billsson, Jarred Z. Olson, Juyeon Park, Gareth Hinds, Annika Ahlberg Tidblad, Dan J. L. Brett, and Paul R. Shearing. Identifying Defects in Li-Ion Cells Using Ultrasound Acoustic Measurements. *Journal of The Electrochemical Society*, 167(12):120530, 2020. ISSN 0013-4651. doi: 10.1149/1945-7111/abb174.

[33] L. Pitta Bauermann, L.V. Mesquita, C. Bischoff, M. Drews, O. Fitz, A. Heuer, and D. Biro. Scanning acoustic microscopy as a non-destructive imaging tool to localize defects inside battery cells. *Journal of Power Sources Advances*, 6(May):100035, 2020. ISSN 26662485. doi: 10.1016/j.powera.2020.100035. URL `https://doi.org/10.1016/j.powera.2020.100035`.

[34] Zhe Deng, Zhenyu Huang, Yue Shen, Yunhui Huang, Han Ding, Aidan Luscombe, Michel Johnson, Jessie E. Harlow, Roby Gauthier, and Jeff R. Dahn. Ultrasonic Scanning to Observe Wetting and "Unwetting" in Li-Ion Pouch Cells. *Joule*, 4(9):2017–2029, 2020. ISSN 25424351. doi: 10.1016/j.joule.2020.07.014. URL `https://doi.org/10.1016/j.joule.2020.07.014`.

[35] Wesley Chang, Clement Bommier, Thomas Fair, Justin Yeung, Shripad Patil, and Daniel Steingart. Understanding Adverse Effects of Temperature Shifts on Li-Ion Batteries: An Operando Acoustic Study. *Journal of The Electrochemical Society*, 167(9):090503, 2 2020. ISSN 1945-7111. doi: 10.1149/1945-7111/ab6c56. URL `https://iopscience.iop.org/article/10.1149/1945-7111/ab6c56`.

[36] Hendrik Zappen, Georg Fuchs, Alexander Gitis, and Dirk Uwe Sauer. In-operando impedance spectroscopy and ultrasonic measurements during high-temperature abuse experiments on lithium-ion batteries. *Batteries*, 6(2), 2020. ISSN 23130105. doi: 10.3390/batteries6020025.

[37] Kevin W. Knehr, Thomas Hodson, Clement Bommier, Greg Davies, Andrew Kim, and Daniel A. Steingart. Understanding Full-Cell Evolution and Non-chemical Electrode Crosstalk of Li-Ion Batteries. *Joule*, 2(6):1146–1159, 2018. ISSN 25424351. doi: 10.1016/j.joule.2018.03.016. URL `https://doi.org/10.1016/j.joule.2018.03.016`.

[38] Thomas Hodson, Shripad Patil, and Daniel Steingart. A Initial Exploration of Coupled Transient Mechanical and Electrochemical Behaviors in Lithium Ion Batteries. *Journal of The Electrochemical Society*, 2021. ISSN 0013-4651. doi: 10.1149/1945-7111/ac0f86.

[39] S. Bhadra, A. G. Hsieh, M. J. Wang, B. J. Hertzberg, and D. A. Steingart. Anode Characterization in Zinc-Manganese Dioxide AA Alkaline Batteries Using Electrochemical-Acoustic Time-of-Flight Analysis. *Journal of The Electrochemical Society*, 163(6):A1050–A1056, 2016. ISSN 0013-4651. doi: 10.1149/2.1201606jes.

[40] Greg Davies, Kevin W. Knehr, Barry Van Tassell, Thomas Hodson, Shaurjo Biswas, Andrew G. Hsieh, and Daniel A. Steingart. State of Charge and State of Health Estimation Using Electrochemical Acoustic Time of Flight Analysis. *Journal of The Electrochemical Society*, 164(12):A2746–A2755, 2017. ISSN 0013-4651. doi: 10.1149/2.1411712jes.

[41] James B. Robinson, Martin Pham, Matt D.R. Kok, Thomas M.M. Heenan, Dan J.L. Brett, and Paul R. Shearing. Examining the Cycling Behaviour of Li-Ion Batteries Using Ultrasonic Time-of-Flight Measurements. *Journal of Power Sources*, 444(September):227318, 2019. ISSN 03787753. doi: 10.1016/j.jpowsour.2019.227318. URL `https://doi.org/10.1016/j.jpowsour.2019.227318`.

[42] Martin T.M. Pham, John J. Darst, Donal P. Finegan, James B. Robinson, Thomas M.M. Heenan, Matt D.R. Kok, Francesco Iacoviello, Rhodri Owen, William Q. Walker, Oxana V. Magdysyuk, Thomas Connolley, Eric Darcy, Gareth Hinds, Dan J.L. Brett, and Paul R. Shearing. Correlative acoustic time-of-flight spectroscopy and X-ray imaging to investigate gas-induced delamination in lithium-ion pouch cells during thermal runaway. *Journal of Power Sources*, 470(March):228039, 2020. ISSN 03787753. doi: 10.1016/j.jpowsour.2020.228039. URL `https://doi.org/10.1016/j.jpowsour.2020.228039`.

[43] Clement Bommier, Wesley Chang, Yufang Lu, Justin Yeung, Greg Davies, Robert Mohr, Mateo Williams, and Daniel Steingart. In Operando Acoustic Detection of Lithium Metal Plating in Commercial LiCoO2/Graphite Pouch Cells. *Cell Reports Physical Science*, 1(4):100035, 4 2020. ISSN 26663864. doi: 10.1016/j.xcrp.2020.100035. URL `https://linkinghub.elsevier.com/retrieve/pii/S2666386420300254`.

[44] Clement Bommier, Wesley Chang, Jianlin Li, Shaurjo Biswas, Greg Davies, Jagjit Nanda, and Daniel Steingart. Operando Acoustic Monitoring of SEI Formation and Long-Term Cycling in NMC/SiGr Composite Pouch Cells. *Journal of The Electrochemical Society*, 167(2):020517, 2020. ISSN 1945-7111. doi: 10.1149/1945-7111/ab68d6.

[45] Wesley Chang, Robert Mohr, Andrew Kim, Abhi Raj, Greg Davies, Kate Denner, Jeung Hun Park, and Daniel Steingart. Measuring effective stiffness of Li-ion batteries: Via acoustic signal processing. *Journal of Materials Chemistry A*, 8(32):16624–16635, 2020. ISSN 20507496. doi: 10.1039/d0ta05552b.

[46] Wesley Chang and Daniel Steingart. Operando 2D Acoustic Characterization of Lithium-Ion Battery Spatial Dynamics. *ACS Energy Letters*, 6(8):2960–2968, 2021. ISSN 2380-8195. doi: 10.1021/acsenergylett.1c01324.

[47] Yi Wu, Youren Wang, Winco K. C. Yung, and Michael Pecht. Ultrasonic Health Monitoring of Lithium-Ion Batteries. *Electronics*, 8(7):751, 2019. ISSN 2079-9292. doi: 10.3390/electronics8070751. URL https://www.mdpi.com/2079-9292/8/7/751.

[48] James B. Robinson, Maximilian Maier, George Alster, Tomos Compton, Dan J.L. Brett, and Paul R. Shearing. Spatially resolved ultrasound diagnostics of Li-ion battery electrodes. *Physical Chemistry Chemical Physics*, 21(12):6354–6361, 2019. ISSN 14639076. doi: 10.1039/c8cp07098a.

[49] Purim Ladpli, Fotis Kopsaftopoulos, Raphael Nardari, and Fu-Kuo Chang. Battery charge and health state monitoring via ultrasonic guided-wave-based methods using built-in piezoelectric transducers. *Smart Materials and Nondestructive Evaluation for Energy Systems 2017*, 10171(April 2017):1017108, 2017. doi: 10.1117/12.2260107.

[50] Bhanu Sood, Michael Osterman, and Michael Pecht. Health Monitoring of Lithium-ion Batteries. *2013 IEEE Symposium on Product Compliance Engineering (ISPCE)*, pages 3–8, 2013. doi: 10.1109/ISPCE.2013.6664165.

[51] Lukas Gold, Tobias Bach, Wolfgang Virsik, Angelika Schmitt, Jana Muller, Torsten E.M. Staab, and Gerhard Sextl. Probing lithium-ion batteries' state-of-charge using ultrasonic transmission – Concept and laboratory testing. *Journal of Power Sources*, 343:536–544, 2017. ISSN 03787753. doi: 10.1016/j.jpowsour.2017.01.090.

[52] L. Oca, N. Guillet, R. Tessard, and U. Iraola. Lithium-ion capacitor safety assessment under electrical abuse tests based on ultrasound characterization and cell opening. *Journal of Energy Storage*, 23(February):29–36, 2019. ISSN 2352152X. doi: 10.1016/j.est.2019.02.033. URL https://doi.org/10.1016/j.est.2019.02.033.

[53] Jun Jie Chang, Xue Feng Zeng, and Tao Lei Wan. Real-time measurement of lithium-ion batteries' state-of-charge based on air-coupled ultrasound. *AIP Advances*, 9(8), 2019. ISSN 21583226. doi: 10.1063/1.5108873. URL https://doi.org/10.1063/1.5108873.

[54] Purim Ladpli, Chen Liu, Fotis Kopsaftopoulos, and Fu Kuo Chang. Estimating lithium-ion battery state of charge and health with ultrasonic guided waves using an efficient matching pursuit technique. *9th European Workshop on Structural Health Monitoring, EWSHM 2018*, 2018.

[55] Honggang Li and Zhenggan Zhou. Numerical simulation and experimental study of fluid-solid coupling-based air-coupled ultrasonic detection of stomata defect of lithium-ion battery. *Sensors (Switzerland)*, 19(10), 2019. ISSN 14248220. doi: 10.3390/s19102391.

[56] Maximilian Maier, Tomos Compton, James B. Robinson, Dan J. L. Brett, George Alster, and Paul R. Shearing. Spatially resolved ultrasound diagnostics of Li-ion battery electrodes. *Physical Chemistry Chemical Physics*, 2018. ISSN 1463-9076. doi: 10.1039/c8cp07098a.

[57] Purim Ladpli, Fotis Kopsaftopoulos, and Fu Kuo Chang. Estimating state of charge and health of lithium-ion batteries with guided waves using built-in piezoelectric sensors/actuators. *Journal of Power Sources*, 384(February):342–354, 2018. ISSN 03787753. doi: 10.1016/j.jpowsour.2018.02.056.

[58] Henry Peter Brunskill. *The Real-Time Characterisation of Dry Machine Element Contacts Using Ultrasonic Reflectometry*. PhD thesis, The University of Sheffield, 2013. URL `http://etheses.whiterose.ac.uk/6494/`.

[59] Misaki Kinoshita-Ise, Manabu Ohyama, Joel M. Ramjist, F. Stuart Foster, Victor X.D. Yang, Muskaan Sachdeva, Shachar Sade, and Neil H. Shear. Ultra high-frequency ultrasound with seventy-MHz transducer in hair disorders: Development of a novel noninvasive diagnostic methodology. *Journal of Dermatological Science*, 102(3):167–176, 2021. ISSN 1873569X. doi: 10.1016/j.jdermsci.2021.04.008. URL `https://doi.org/10.1016/j.jdermsci.2021.04.008`.

[60] P Daponte, G Fazio, and A Molinaro. Detection of echoes using time-frequency analysis techniques. *Instrumentation and Measurement, IEEE Transactions on*, 45(1):30–40, 1996. ISSN 0018-9456. doi: 10.1109/19.481308.

[61] Leopoldo Angrisani, Pasquale Daponte, and Massimo D'Apuzzo. The detection of echoes from multilayer structures using the wavelet transform. *IEEE Transactions on Instrumentation and Measurement*, 49(4):727–731, 2000. ISSN 00189456. doi: 10.1109/19.863914.

[62] A. Grinsted, J. C. Moore, and S. Jevrejeva. Application of the cross wavelet transform and wavelet coherence to geophysical time series. *Nonlinear Processes in Geophysics*, 11(5/6):561–566, 11 2004. ISSN 1607-7946. doi: 10.5194/npg-11-561-2004. URL `http://www.nonlin-processes-geophys.net/11/561/2004/`.

[63] A. Wade, R. Copley, A. Alsheikh Omar, B. Clarke, T. Liskiewicz, and M. Bryant. Novel numerical method for parameterising fretting contacts. *Tribology International*, 149(May):105826, 2019. ISSN 0301679X. doi: 10.1016/j.triboint.2019.06.019. URL `https://linkinghub.elsevier.com/retrieve/pii/S0301679X19303330`.

[64] Peter J. Bugryniec, Jonathan N. Davidson, and Solomon F. Brown. Assessment of thermal runaway in commercial lithium iron phosphate cells due to overheating in an oven test. *Energy Procedia*, 151:

74–78, 2018. ISSN 18766102. doi: 10.1016/j.egypro.2018.09.030. URL `https://doi.org/10.1016/j.egypro.2018.09.030`.

[65] Peter J. Bugryniec, Jonathan N. Davidson, Denis J. Cumming, and Solomon F. Brown. Pursuing safer batteries: Thermal abuse of LiFePO4 cells. *Journal of Power Sources*, 414(October 2018):557–568, 2019. ISSN 03787753. doi: 10.1016/j.jpowsour.2019.01.013.

[66] Peter J. Bugryniec, Dr Jonathan N. Davidson, and Dr Solomon F. Brown. Advanced abuse modelling of Li-ion cells – A novel description of cell pressurisation and simmering reactions. *Journal of Power Sources*, 474(May):228396, 2020. ISSN 03787753. doi: 10.1016/j.jpowsour.2020.228396. URL `https://doi.org/10.1016/j.jpowsour.2020.228396`.

[67] Xuning Feng, Mou Fang, Xiangming He, Minggao Ouyang, Languang Lu, Hao Wang, and Mingxuan Zhang. Thermal runaway features of large format prismatic lithium ion battery using extended volume accelerating rate calorimetry. *Journal of Power Sources*, 255:294–301, 2014. ISSN 03787753. doi: 10.1016/j.jpowsour.2014.01.005. URL `http://dx.doi.org/10.1016/j.jpowsour.2014.01.005`.

[68] Donal P. Finegan, Mario Scheel, James B. Robinson, Bernhard Tjaden, Marco Di Michiel, Gareth Hinds, Dan J.L. Brett, and Paul R. Shearing. Investigating lithium-ion battery materials during overcharge-induced thermal runaway: An operando and multi-scale X-ray CT study. *Physical Chemistry Chemical Physics*, 18(45):30912–30919, 2016. ISSN 14639076. doi: 10.1039/c6cp04251a.

[69] Shishuo Liang, Wenqi Yan, Xu Wu, Yi Zhang, Yusong Zhu, Hongwei Wang, and Yuping Wu. Gel polymer electrolytes for lithium ion batteries: Fabrication, characterization and performance. *Solid State Ionics*, 318(August 2017):2–18, 2018. ISSN 01672738. doi: 10.1016/j.ssi.2017.12.023.